



# **DIPLOMARBEIT**

# Diffusive Heat Transport Profiles from Integrated Data Analysis at ASDEX Upgrade

zur Erlangung des akademsichen Grades

Diplom-Ingenieur

im Rahmen des Studiums

Physikalische Energie- und Messtechnik

eingereicht von

Raffael Wendlinger

Matrikelnummer 00273289

ć	ausgef	führt am Institut für Angewandte Physik
(	der Fa	akultät für Physik der Technischen Universität Wien
(	(in Zu	ısammenarbeit mit dem Max-Planck-Institut für Plasmaphysik)

Betreuung
Betreuerin: Univ. Prof. Dr. Elisabeth Wolfrum
Mitwirkung: Dr. Rainer Fischer
Mitwirkung: Dr. Michael Bergmann

Wien, 19.09.2025		
, , , , , , , , , , , , , , , , , , , ,	Raffael Wendlinger	Elisabeth Wolfrum

### Abstract

Reliable estimates of heat transport are crucial for interpreting tokamak experiments and informing scenario development, as effective heat confinement is necessary to achieve net energy gain. In magnetically confined plasmas, turbulent transport dominates energy losses, but its complex nature cannot be described analytically. While advanced numerical codes exist for detailed turbulence modeling, they are computationally intensive.

This thesis adopts an alternative approach by relying exclusively on experimental data to use in a diffusive transport coefficient model adapted from the transport code ASTRA. Heat transport is analyzed by establishing a power balance for electrons and ions, accounting for all relevant power sources and sinks, such as heating systems and radiative losses, to calculate the corresponding diffusion coefficients  $\chi$ . Specifically, this work implements, validates and analyzes the calculation of the electron and ion heat diffusivities within the Bayesian integrated data analysis framework (IDA/IDE) at the ASDEX Upgrade tokamak.

A central contribution is a robust reconstruction of the radiated-power profile: instead of relying on sparse impurity concentrations (W, C) and fixed radiation functions, a Gaussian-Process Tomography (GPT) code using bolometer data is ported and integrated into IDE (Fortran90). The implementation introduces an X-point-aware masking that excludes divertor pixels while preserving confined-plasma emission and performs radial integration in  $\rho_{tor}$  with spline-based volume normalization. The GPT-based  $P_{\rm rad}$  agrees with manual tomographies and corrects the unphysical edge roll-off of the legacy model, thereby improving  $\chi_e$  near the pedestal.

A Monte Carlo sensitivity study quantifies uncertainty envelopes versus radius: temperature gradients dominate ( $T_e$  for  $\chi_e$ ,  $T_i$  for  $\chi_i$ ), with largest relative uncertainties in the core and edge and smaller, more reliable values for  $0.2 \le \rho_{tor} \le 0.8$ . High-time-resolution analyses demonstrate interpretable  $\chi$  dynamics during ELM cycles when the diagnostic data acquisition rate permits; the impact of temporal resolution and  $\frac{dW}{dt}$  treatment is characterized and averaging across the same time window reconciles profiles obtained at different cadences.

Overall, the work delivers a validated, readily available pathway to transport coefficients directly from IDE, together with practical guidance on reliability and limits.

# Zusammenfassung

Zuverlässige Abschätzungen des Wärmetransports sind entscheidend für die Auswertung von Tokamak-Experimenten und die Szenarioentwicklung, da ein effektiver Wärmeeinschluss notwendig ist, um einen Nettoenergiegewinn zu erzielen. In magnetisch eingeschlossenen Plasmen dominiert turbulenter Transport die Energieverluste, dessen komplexe Natur sich jedoch nicht analytisch beschreiben lässt. Obwohl es fortgeschrittene numerische Codes für detaillierte Turbulenzmodellierung gibt, sind diese rechenintensiv und eignen sich daher nicht für die Analyse vieler experimenteller Plasmaentladungen.

Diese Arbeit verfolgt einen alternativen Ansatz, der ausschließlich experimentelle Daten nutzt, um ein diffuses Transportkoeffizienten-Modell zu speisen, das aus dem transport code ASTRA adaptiert wurde. Der Wärmetransport wird durch Aufstellen einer Leistungsbilanz für Elektronen und Ionen analysiert, in der sämtliche relevanten Leistungsquellen und -senken, wie Heizsysteme und Strahlungsverluste, berücksichtigt werden, um die zugehörigen Diffusionskoeffizienten  $\chi$  zu bestimmen. Konkret werden Implementierung, Validierung und Analyse der Berechnung der Elektronen- und Ionen-Wärmediffusivitäten im bayesschen integrierte daten analyse system (IDA/IDE) am ASDEX Upgrade Tokamak vorgestellt.

Ein zentraler Beitrag ist eine robuste Rekonstruktion des Strahlungsleistungsprofils: Anstatt sich auf spärliche Verunreinigungskonzentrationen (W, C) und feste Strahlungsfunktionen zu stützen, wird ein Gaussian-Process-Tomographie (GPT)-Code auf Basis von Bolometerdaten nach Fortran90 portiert und in IDE integriert. Die Implementierung führt eine X-Punkt-sensitive Maskierung ein, die Divertor-Pixel ausschließt, während die Emission des eingeschlossenen Plasmas erhalten bleibt, und führt eine radiale Integration in  $\rho_{tor}$  mit splinebasierter Volumennormierung durch. Das GPT-basierte  $P_{\rm rad}$  stimmt mit manuellen Tomographien überein und korrigiert den unphysikalischen Randabfall des Legacy-Modells, wodurch  $\chi_e$  im Bereich des Pedestals verbessert wird.

Eine Monte-Carlo-Sensitivitätsstudie quantifiziert Unsicherheitshüllen in Abhängigkeit vom Radius: Temperaturgradienten dominieren ( $T_e$  für  $\chi_e$ ,  $T_i$  für  $\chi_i$ ), mit den größten relativen Unsicherheiten im Kern und am Rand sowie kleineren, verlässlicheren Werten für  $0.2 \leq \rho_{tor} \leq 0.8$ . Analysen mit hoher zeitlicher Auflösung zeigen interpretierbare  $\chi$ -Dynamik während ELM-Zyklen, sofern die Diagnostik-Kadenz dies zulässt; der Einfluss der zeitlichen Auflösung und der Behandlung von  $\frac{dW}{dt}$  wird charakterisiert, und Mittelungen über dasselbe Zeitfenster versöhnen Profile, die mit unterschiedlichen Kadenzen gewonnen wurden.

Insgesamt liefert die Arbeit einen validierten, leicht nutzbaren Pfad zu Transportkoeffizienten direkt aus IDE sowie praktische Hinweise zu Verlässlichkeit und Grenzen.

# Contents

Abstract						
Zι	ısam	menfassung				
1	Introduction					
	1.1 1.2	Fusion Energy				
2	$Th\epsilon$	oretical Background				
	2.1	Nuclear fusion				
	2.2	Magnetic confinement and the Tokamak				
	2.3	Magnetohydrodynamics				
	2.4	Equilibrium Solvers				
	2.5	IDA and IDE				
	2.6	Automated System for TRansport Analysis (ASTRA)				
	2.7	Diffusive Heat Transport				
		2.7.1 Energy conservation and heat flux				
		2.7.2 Calculation of the transport coeffcient				
		2.7.3 Interpretation of the transport coeffcient				
	2.8	Gaussian Process Regression (GPR)				
_						
3		erimental Background 22				
	3.1	ASDEX Upgrade				
	3.2	Heating				
		3.2.1 Neutral Beam Injection - NBI				
		3.2.2 Electron Cyclotron Resonance Heating - ECRH				
	0.0	3.2.3 Ion Cyclotron Resonance Heating - ICRH				
	3.3	Diagnostics				
		3.3.1 Electron Cyclotron Emission - ECE				
		3.3.2 Deuterium Cyanide Laser Interferometry - DCN				
		3.3.3 Lithium Beam Emission Spectroscopy - Li-BES				
		3.3.4 Thomson Scattering - TS				
		3.3.5 Charge Exchange Recombination Spectroscopy - CXRS				
		3.3.6 Bolometers				
4	Tra	asport coefficient calculation implementation 28				
	4.1	Summary of the mod_coefficients_model.f90 Module				
	4.2	Subroutines				
		4.2.1 eval_equipartition_model				
		4.2.2 eval_POHM_model				
		4.2.3 eval_PRAD_model				
	4.3	Implementation of GPT into the IDE framework				
5	۸	lysis of the transport coefficients calculation 39				
IJ	5.1	lysis of the transport coefficients calculation  Power depositions				
	$5.1 \\ 5.2$	Radiative Power Loss				
	5.2 $5.3$	Sensitivity Study				
	0.0	Dombierity Duddy				

	5.4 Transport coefficient dynamics during ELM events	53
	5.5 Transient condition analysis	55
	5.6 Impact of Temporal Resolution	57
6	Conclusion	59
7	Outlook	60
A	cknowledgements	61
$\mathbf{A}$	ppendix	62
Acronyms		
Li	ist of Figures	66
Li	ist of Tables	69
U	se of Generative AI Tools in Thesis Preparation	70
$\mathbf{B}$	ibliography	71

# 1 Introduction

# 1.1 Fusion Energy

"If I have seen further it is by standing on the shoulders of Giants."

— Isaac Newton, The Correspondence of Isaac Newton [1]

With global energy demand continuing to rise and the urgency of both the climate and energy crises intensifying, the need to tap into new sustainable energy sources has never been greater. In 2024, global renewable energy capacity additions surged by an estimated 25%, reaching approximately 700 gigawatts—a new all-time high and the 22nd consecutive year of record-breaking growth in the sector [2].

Despite this strong growth, significant challenges persist—most notably, the intermittency of solar and wind power. Their output fluctuates due to weather patterns and seasonal variation, making it difficult to ensure a stable and reliable electricity supply. Recent events, such as the widespread blackout across the Iberian Peninsula in May 2025, underscore the vulnerabilities of current energy systems when over-reliant on variable renewable generation without adequate support infrastructure [3]. Efforts to stabilize and store renewable electricity at the scale required for national grids have yet to yield a fully viable solution. Batteries, pumped hydro, and other storage technologies remain either too costly, geographically constrained, or insufficient in duration and scale. As a result, the lack of dependable baseload power from renewables continues to be one of the most pressing issues in achieving a truly sustainable energy system.

Fusion energy has received increasing attention as a potential solution [4, 5]. Compared to conventional nuclear fission, fusion offers several advantages, particularly in terms of safety and radioactive waste. Fission reactors rely on a self-sustaining chain reaction in radioactive fuel, which must be carefully controlled to avoid catastrophic failure. In contrast, fusion reactions are inherently difficult to initiate and maintain, making them far safer: any disruption would simply cause the reaction to stop, rather than spiral out of control [6, 7].

In terms of waste, fusion does produce radioactive materials, primarily through neutron activation of reactor components, but these do not include long-lived isotopes and are far more manageable. Most of the waste is limited to the reactor vessel itself, and with appropriate material choices, it can potentially be reused after about 100 years of storage [8, 9].

These characteristics position fusion as a strong candidate to contribute significantly to a carbon-free energy mix. However, many engineering and scientific hurdles remain before fusion can become a practical energy source. One of the most promising designs for a future fusion power plant is the tokamak, a device that uses a toroidal magnetic field to confine plasma [10]. The Axially Symmetric Divertor Experiment (ASDEX) Upgrade is an experimental facility of this kind and was built to study the behaviour of the plasma under magnetic confinement. A central challenge in this approach is to control the plasma instabilities, which can damage internal components. Preventing or mitigating these instabilities is essential for making fusion commercially viable and requires detailed understanding of the underlying plasma dynamics.

Plasma and heat transport are key drivers in these, as energy losses in tokamaks often exceed what classical and neoclassical theory predict. This is mainly due to turbulent,

or anomalous, transport—caused by complex, multi-scale plasma fluctuations. While much progress has been made in understanding and modeling these processes, transport still limits performance in many regimes [11].

To support these studies, advanced analysis tools and appropriate data processing methods are essential. One fundamental outcome of such analysis is the determination of diffusive transport coefficients, which quantify how heat and particles move through diffusive processes in the plasma. These coefficients provide a low-level description of transport processes and serve as valuable indicators of discharge behavior. Accurately deriving them is crucial for interpreting experimental results and guiding further development in fusion devices.

To enable these studies, precise diagnostics and advanced analysis tools are needed to deepen our understanding. A fundamental aspect of such analysis is determining the so-called magnetic equilibrium of the plasma, which describes the nested magnetic flux surfaces where pressure remains constant [12, 13]. Accurate equilibrium reconstruction is essential for combining and interpreting measurements that are derived in different locations of the tokamak.

# 1.2 Objective of this work

This thesis aims to analyze, validate and improve upon the newly implemented diffusive coefficient calculation model in the Integrated Data Analyses (IDA)/Integrated Data analyses Equilibrium (IDE) Framework of ASDEX Upgrade. The applicability and accuracy of the model will be tested for different discharge conditions.

The sum of all transport mechanisms, including turbulent and neoclassical transport, can be described by a diffusion coefficient. While particle transport is more challenging to characterize due to poorly measurable sources and the possibility of inward-directed particle flux under certain turbulent regimes, it is possible to describe heat transport using a radial profile of the heat transport coefficient.

This requires knowledge of the magnetic equilibrium, heat sources (plasma heating), and measured temperature profiles. The calculation of these diffusive transport coefficients has been implemented within the IDA/IDE framework, which employs Bayesian inference methods to systematically combine measurements from multiple diagnostics into self-consistent profiles with robust uncertainty estimates.

In this work, the reliability of the calculation will be analyzed, validated, and improved across various plasma regimes and different radial regions. Particular attention will be given to assessing the model's performance under different discharge conditions, identifying potential sources of uncertainty, and implementing improvements to enhance the accuracy and robustness of the transport coefficient calculations.

# 2 Theoretical Background

"Everything is theoretically impossible, until it is done."

— Robert A. Heinlein

This section provides a brief overview of the fundamental physics involved in fusion engineering, plasma transport physics and how an equilibrium is reconstructed.

### 2.1 Nuclear fusion

Nuclear fusion is the counterpart to nuclear fission. While fission involves splitting a heavy nucleus into two lighter nuclei, fusion refers to the process in which two light nuclei combine to form a heavier nucleus. Both processes release energy, which can be explained by the concept of mass defect.

The mass defect is the difference between the mass of a nucleus and the total mass of its individual protons and neutrons [14]. This discrepancy arises because some mass is converted into energy during the reaction. Einstein's mass-energy equivalence

$$E = mc^2 (1)$$

allows us to calculate the energy released in nuclear reactions. Plotting the binding energy per nucleon as a function of mass number for various nuclei yields the curve shown in Figure 1, which illustrates why energy is released in both fusion and fission processes.

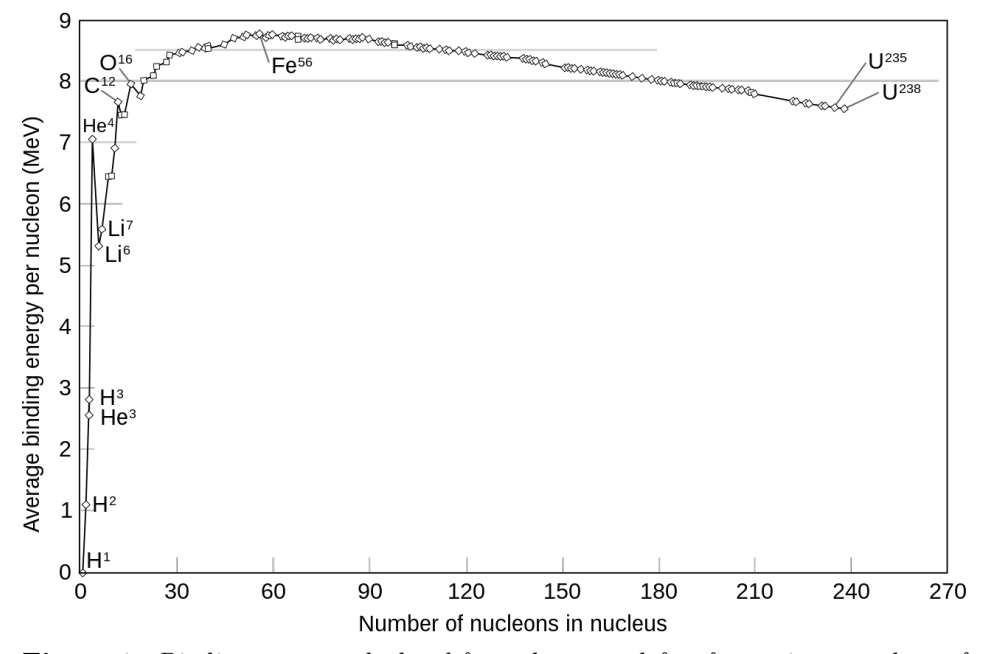


**Figure 1:** Binding energy calculated from the mass defect for various numbers of nucleons in the nucleus. [15].

The binding energy per nucleon increases rapidly for the lightest elements, reaching a maximum at iron (Fe), which has 56 nucleons. Beyond this point, as nuclei become heavier, the binding energy per nucleon gradually decreases.

This characteristic shape of the curve is explained by the interplay of two fundamental forces within the nucleus. For lighter elements, each added nucleon contributes significantly to the overall binding energy, as it is attracted to all other nucleons through the strong nuclear force—a short-range but extremely powerful interaction. However, in heavier nuclei, this force becomes less effective due to its short range and the increasing distance between nucleons. At the same time, the growing number of positively charged protons leads to stronger electrostatic repulsion (Coulomb force), which works against the binding effect of the strong nuclear force [14].

Fusion reactions derive their energy from the difference in binding energy between the reactants and the resulting nucleus. A steep gradient in binding energy between the initial and final nuclei makes a reaction more energetically favorable, which is a key consideration in selecting potential fusion fuels. One of the most promising reactions is the deuterium  $\binom{2}{1}H$ -tritium  $\binom{3}{1}H$  fusion reaction

$$_{1}^{2}H +_{1}^{3}H \rightarrow _{2}^{4}He(3.5\text{MeV}) + \text{n}(14.1\text{MeV}),$$
 (2)

which exploits the high binding energy of helium and releases a total of 17.6 MeV per fusion event. To initiate fusion, the reacting nuclei must possess enough kinetic energy to overcome the Coulomb barrier—the electrostatic repulsion between positively charged nuclei-requiring sufficient kinetic energy. Figure 2 shows the fusion cross-section for different colliding nuclei as a function of relative kinetic energy. A high cross-section is favorable since it leads to a higher reaction rate. For the deuterium-tritium reaction, the cross-section peaks at energies around 10-50 keV, which corresponds to temperatures exceeding 100 million Kelvin [14].

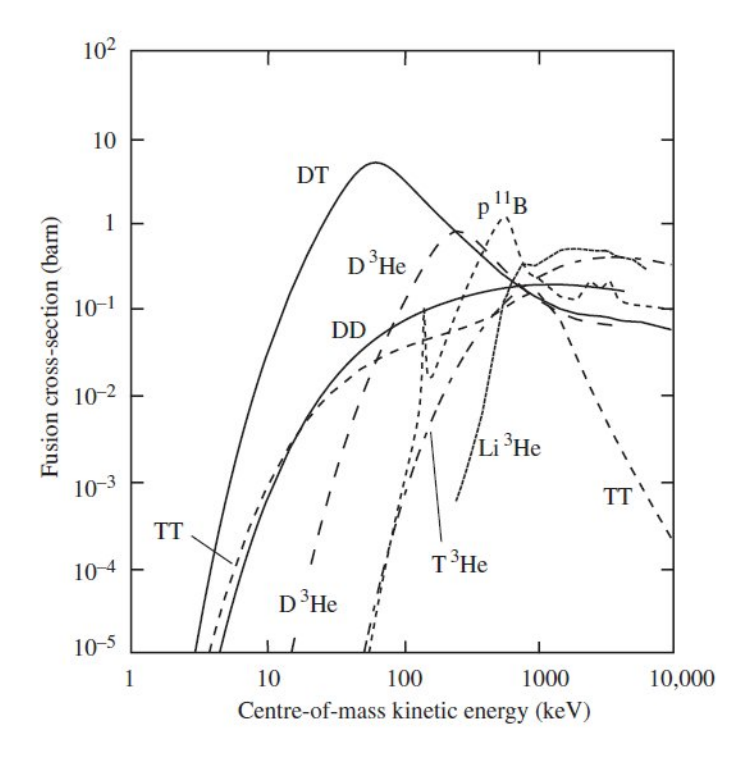


**Figure 2:** Fusion cross sections versus the centre of mass energy for reactions of interest [16].

At such extreme temperatures, particles possess kinetic energies sufficient to overcome the Coulomb barrier, aided by quantum tunneling effects and the Maxwell-Boltzmann distribution, which ensures that even at lower average energies, a fraction of particles still possess the high energies required for fusion.

For a fusion reactor to serve as a viable energy source, the energy produced must exceed the energy required to sustain the plasma. This condition is captured by the Lawson criterion [17], which defines a minimum threshold for the so-called triple product:

$$n * \tau_E * T > 3 \times 10^{21} \text{ keV} \cdot \text{s} \cdot \text{m}^{-3}.$$
 (3)

Here, n is the particle density, T the plasma temperature, and  $\tau_E$  the energy confinement time, which is defined as  $\tau_E = W/P_{loss}$  with W being the total energy stored in the plasma and  $P_{loss}$  the rate of energy loss [17].

The Lawson criterion represents a fundamental benchmark for achieving net energy gain from fusion, and the deuterium-tritium reaction appears most promising for meeting this requirement. However, tritium presents a significant challenge due to its scarcity in nature, resulting from its short half-life of 12.32 years. This radioactive decay prevents large-scale tritium stockpiling, necessitating that fusion reactors produce their own tritium through nuclear reactions within the reactor itself [18].

Fusion reactors must therefore incorporate "breeding blankets" that surround the plasma chamber, where the high-energy neutrons produced by the D-T fusion reaction interact with lithium to create tritium through two primary reactions:

$$n + {}_{3}^{6} Li \rightarrow {}_{2}^{4} He + {}_{1}^{3} H + 4.8 \text{ MeV}$$
 (4)

$$n +_{3}^{7} Li \to_{2}^{4} He +_{1}^{3} H + n - 2.5 \text{ MeV}$$
 (5)

The reaction with <sup>6</sup>Li (equation 4), which comprises approximately 7.5% of natural lithium, is highly favorable and releases energy, while the reaction with <sup>7</sup>Li (equation 5) has a smaller cross-section and actually consumes energy. Most tritium breeding strategies focus on the <sup>6</sup>Li reaction due to its superior energy balance and higher cross section [18].

Examining global fuel requirements provides insight into the long-term sustainability of fusion energy. A typical gigawatt fusion power plant would consume approximately 120 kg of deuterium and 4 tonnes of lithium annually [18]. Deuterium, extractable from seawater at minimal cost (roughly 0.02 g per liter), represents an essentially unlimited resource—the world's oceans contain sufficient deuterium to supply fusion energy for more than  $4 \times 10^{10}$  world energy units, where one world energy unit corresponds to the current global annual electricity demand of  $1.12 \times 10^{20}$  J = 3.42 terawatt-years [18, 19].

Lithium availability presents a more constrained but still abundant resource. Current terrestrial lithium reserves of approximately 13.5 million tonnes could support fusion energy production for about  $10^3$  world energy units. However, seawater contains an estimated 230 billion tonnes of lithium at a concentration of 0.2 mg per liter, sufficient to supply approximately  $25 \times 10^6$  world energy units—enough to meet global energy demands for millions of years, assuming efficient lithium extraction from seawater can be developed [18].

This fuel abundance distinguishes fusion from other energy sources and positions it as one of the few technologies capable of providing sustainable energy on geological timescales, comparable only to solar energy in terms of long-term availability.

Although theoretical models and experimental designs have outlined pathways toward harnessing fusion power, no reactor has yet achieved sustained, practical energy production. The primary engineering challenge lies in maintaining extremely high temperatures and densities within engineered systems capable of withstanding these conditions for sufficient duration while remaining economically viable.

One of the leading approaches to meeting these conditions is magnetic confinement, particularly in devices such as the tokamak, which is discussed in detail in section 2.2.

# 2.2 Magnetic confinement and the Tokamak

Magnetic confinement is one of the most extensively studied methods for containing plasma heated to millions of degrees, a requirement for achieving fusion reactions. Plasmas consist of charged particles which induced by the Lorentz force follow a gyrating motion around the magnetic field lines. By forming closed, ring-shaped magnetic field lines, it becomes possible to confine plasma without direct physical contact which is critical for magnetic confinement. This is done with strong magnets which create a toroidally shaped magnetic field, effectively confining the plasma within it.

The most studied fusion reactor design of this kind is the Tokamak. The term Tokamak originates from a Russian acronym translating to "toroidal chamber with magnetic coils" [20]. A Tokamak consists primarily of three main magnetic coil systems, as illustrated in Figure 3.

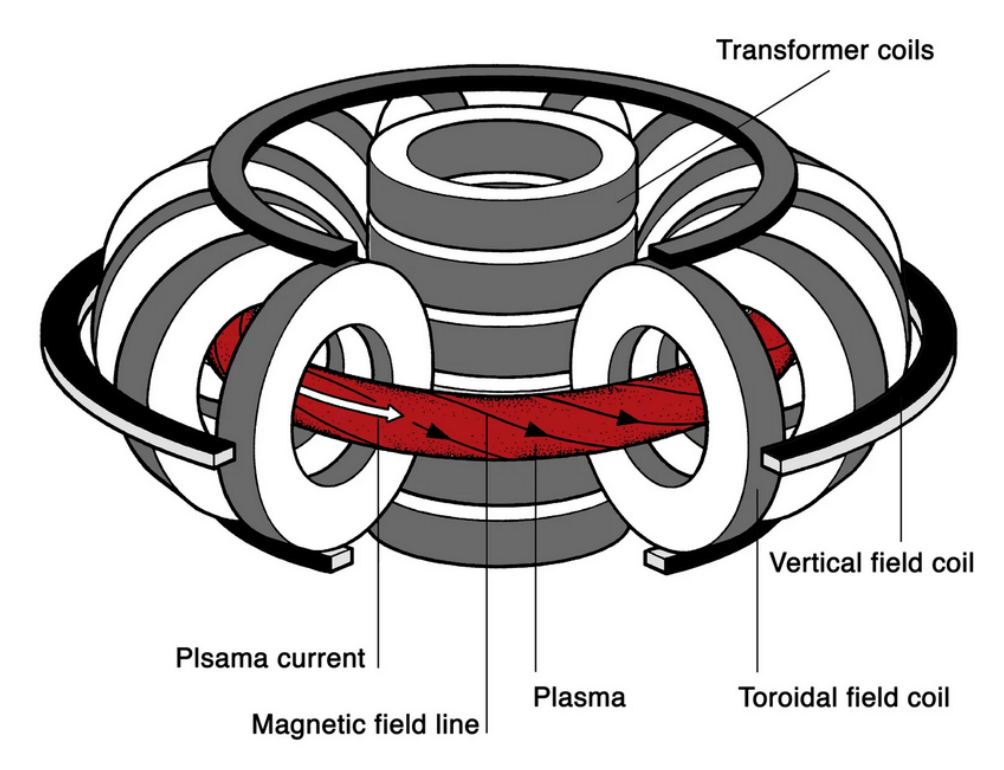


Figure 3: Schematic of a Tokamak [21]. The toroidal field coils are arranged around the vaccum vessel. The vertical field coils are used to better control the plasma position and shape. The transformer coils induces the plasma current which is indicated by the white arrow. The path of the particles follows a helical path around the nested magnetic flux surfaces (red) indicated by the black magnetic field lines.

The commonly "D"-shaped toroidal field coils arranged around the torus form the core component of the Tokamak, generating the toroidal magnetic field. However, this toroidal magnetic field alone is insufficient to fully confine the plasma, as it weakens progressively from the inner region toward the outer part of the torus. This gradient, coupled with the curvature of the field lines, induces a vertical drift in oppositely charged particles in opposing directions. This charge separation creates an electric field that

ultimately pushes all particles, irrespective of their charge, out of the confinement area. This phenomenon is known as the "E×B-Drift" [22]

$$\vec{v}_{ExB} = \frac{\vec{E} \times \vec{B}}{B^2}.$$
 (6)

To counteract this drift, a solenoid at the center of the Tokamak acts as a transformer, inducing an electric current within the plasma. This current produces a poloidal magnetic field that, when combined with the existing toroidal field, results in helical magnetic field lines. These helical lines spiral around the nominal circular path of the torus (see "Magnetic field line" in Figure 3). A drawback of this method is that the plasma current is induced by a changing flux in the transformer core, which requires a varying current in the primary winding. The maximum current that can be supplied to the primary winding ultimately limits the discharge durations and necessitates the tokamak's pulsed operation. Additional poloidal field coils are utilized to maintain plasma position and counterbalance forces that drive the plasma outward [14, 23].

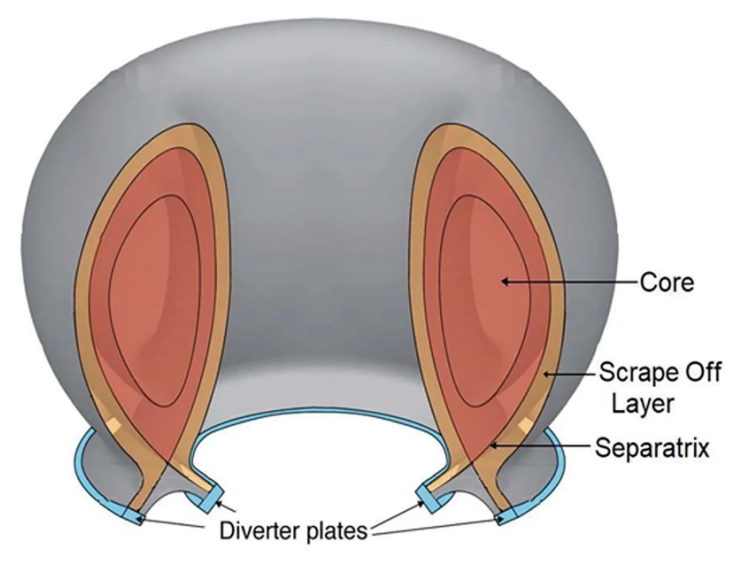


**Figure 4:** Plasma geometry inside a tokamak [24]. The magnetic field lines are marked in black while detailing the plasma core in red and the SOL in orange. The divertor plates can be seen in blue and intersect the separatrix.

The geometry of the contained plasma consists of surfaces of constant magnetic flux, known as magnetic flux surfaces. The cross section of such a geometry is illustrated in Figure 4. In a perfectly axisymmetric tokamak, these flux surfaces are nested toroidal surfaces, which means that the magnetic field lines are closed loops that do not intersect each other. Modern tokamaks employ a "double-null" configuration [25], which features two divertors which were first introduced in 1958 [26, 27]. This design allows for better control of plasma stability and improved exhaust of impurities and heat from the plasma through the separatrix. The separatrix is the boundary between the confined plasma (nested flux surfaces) and the Scrape-Off Layer (SOL), where the plasma interacts with the walls of the tokamak. The SOL is a region of low-density plasma that extends beyond the separatrix and plays a crucial role in heat and particle exhaust.

Examining the cross section in Figure 4, it is evident that the plasma is vertically elongated, with a greater extent along the vertical axis than the horizontal. This geometric complexity means that several parameters are needed to fully characterize

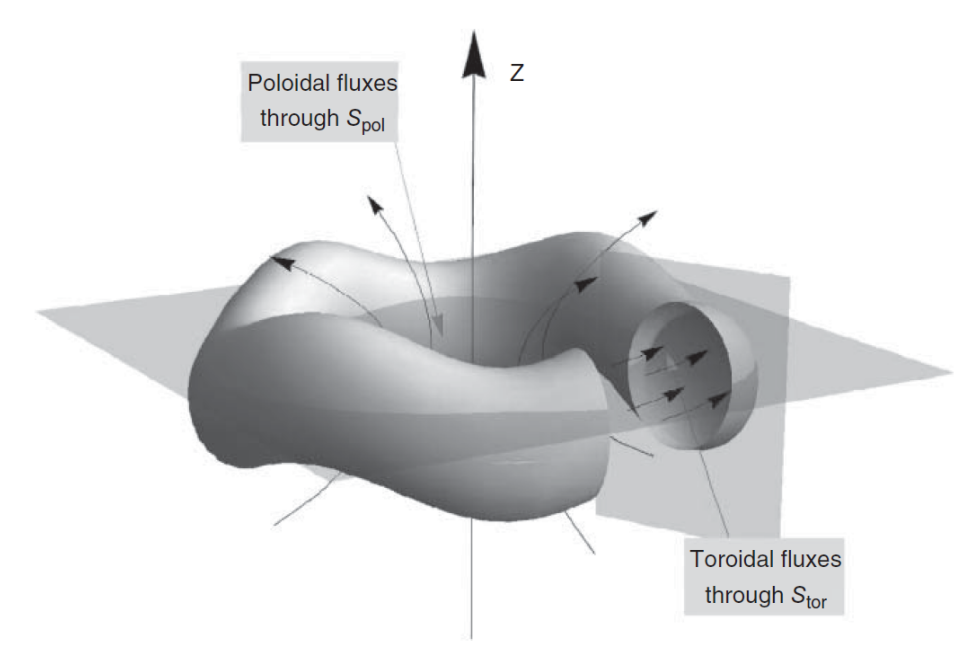


**Figure 5:** Example toroidal geometry from [12]. Two topologically distinct curves can be used to define flux integrals, which in turn can act as labels for flux surfaces.

the shape and position of the magnetic flux surfaces. To simplify the description of plasma profiles and facilitate analysis, it is common practice to introduce a normalized plasma radius, defined in terms of either the poloidal or toroidal magnetic flux, as illustrated in Figure 5. These normalized coordinates are given by:

$$\rho_{pol}(\Psi) = \sqrt{\frac{\Psi - \Psi_{axis}}{\Psi_{sep} - \Psi_{axis}}} \quad \text{with} \quad \Psi = \int_{S_{pol}} \vec{B} \cdot dS$$
 (7)

$$\rho_{tor}(\Phi) = \sqrt{\frac{\Phi - \Phi_{axis}}{\Phi_{sep} - \Phi_{axis}}} \quad \text{with} \quad \Phi = \int_{S_{tor}} \vec{B} \cdot dS.$$
 (8)

Here,  $\Psi$  denotes the poloidal magnetic flux, with  $\Psi_{\rm axis}$  and  $\Psi_{\rm sep}$  corresponding to the values at the magnetic axis and separatrix, respectively. Similarly,  $\Phi$  represents the toroidal magnetic flux, with  $\Phi_{\rm axis}$  and  $\Phi_{\rm sep}$  defined analogously. Although this approach may initially appear to add significant complexity, it ultimately allows us to represent plasma parameters along a single normalized axis starting from the plasma center to the plasma edge. The underlying condition allowing that is derived in the following section 2.3. If not stated otherwise,  $\rho_{tor}$  will be mainly used throughout this work, as it serves as the standard coordinate for transport coefficient calculations in the reference framework.

# 2.3 Magnetohydrodynamics

Magnetohydrodynamics (MHD) serves as the foundation for all equilibrium reconstructions, providing a fluid-based description of macroscopic plasma behavior [28]. The MHD approach employs hydrodynamic principles—such as mass and momentum conservation—and incorporates the Lorentz force to describe electrically conducting fluids within magnetic fields. Using magneto hydrodynamics simplifies plasma modeling significantly by describing plasma dynamics as continuous fields rather than tracking individual particle motions. This simplification facilitates the practical use of numerical solvers for plasma simulations.

Equilibrium conditions are established when the internal plasma pressure precisely balances the external magnetic pressure. This state of equilibrium for static, single-fluid MHD plasmas is described by the following criterion [22]:

$$\nabla p = j \times B,\tag{9}$$

where p is the kinetic pressure, j the current density, and B the magnetic field. This relationship implies two key conditions derived from dot products: first,  $B \cdot \nabla p = 0$  indicates that the pressure remains constant along magnetic field lines; second,  $j \cdot \nabla p = 0$  means that current flows along surfaces of constant pressure. Consequently, current lines and magnetic field lines together form surfaces of constant magnetic flux, known as flux surfaces. In axisymmetric geometries, such as the tokamak, these flux surfaces are described in cylindrical coordinates  $(r, \theta, z)$  by the Grad-Shafranov equation (GSE) [22, 29, 30]:

$$\frac{\partial^2 \psi}{\partial r^2} - \frac{1}{r} \frac{\partial \psi}{\partial r} + \frac{\partial^2 \psi}{\partial z^2} = -\mu_0 r^2 p'(\psi) - \mu_0^2 f(\psi) f'(\psi), \tag{10}$$

where  $\mu_0$  represents magnetic permeability,  $\psi$  the poloidal magnetic flux function, and  $f = \frac{\mu_0}{2\pi} I_{pol}$  the current flux function proportional to the total poloidal current  $I_{pol}$  [12]. Plasma properties are largely uniform along each flux surface, perpendicular to these concentric surfaces the conditions vary rapidly making them a great coordinate system to describe the plasma. These equlibria are therefore essential for plasma analysis.

# 2.4 Equilibrium Solvers

Equilibrium solvers are computational codes that reconstruct MHD equilibria using diagnostic data and optional constraints. These codes are mainly numerical solvers for the GSE (equation 10) and often include optimization routines to improve the solution quality [31, 32].

A fundamental problem with the GSE is that it is static—it does not consider how the plasma evolves over time and therefore poorly models current distribution. When the GSE is solved for a given time t, it calculates a snapshot of the equilibrium at that time only. This creates a series of unconnected solutions in time, depending on how often the input data is sampled. While smoothness constraints can help reduce unphysical jumps in current profiles, this method relies on artificial regularization instead of actual physical measurements. A better approach couples the GSE with the current diffusion equation (CDE), which reduces the need for non-physical smoothing [33, 34, 35].

The CDE models how current profiles change over time. In this coupled approach, the GSE solution at time t provides equilibrium conditions that the CDE uses to predict boundary conditions for the next GSE calculation at time t+1 [33]. This coupling helps to avoid unphysical jumps in the results and creates more reliable equilibrium data.

### 2.5 IDA and IDE

The Integrated Data Analysis (IDA) framework forms the essential basis for any IDE equilibrium reconstruction at ASDEX Upgrade. IDA employs Bayesian inference to systematically combine measurements of the same physical quantities, such as electron temperature or density, from multiple diagnostics into a single, self-consistent profile. This approach not only improves the statistical accuracy and spatial resolution of the reconstructed profiles, but also provides robust uncertainty estimates by rigorously propagating measurement errors and prior knowledge through the inference process [31, 33, 36].

Building on this foundation, the Integrated Data Equilibrium (IDE) code utilizes the high-fidelity profiles produced by IDA as both input data and as constraints for equilibrium reconstruction. In particular, IDE constrains the pressure gradient term  $\nabla p$  in the Grad-Shafranov equation using pressure profiles derived from the sum of thermal electron, thermal ion pressure and fast-ion pressure pressure, as provided by IDA. This ensures that the equilibrium solution is consistent with the best-available kinetic data, rather than relying solely on magnetic measurements or less direct constraints. Additionally, it is also coupled with a current diffusion equation to avoid nonphysical behaviour as explained in 2.4 [33].

# 2.6 Automated System for TRansport Analysis (ASTRA)

The Automated System for TRansport Analysis (ASTRA) code is a widely used and highly flexible transport simulation tool developed for the analysis and modeling of magnetically confined plasmas, particularly in tokamak experiments. Originally created in the late 1980s at the Kurchatov Institute in Moscow, ASTRA has evolved into a modular and extensible system, allowing users to construct customized transport models for both predictive and interpretative studies. Its architecture is based on a library of interchangeable modules, each representing a specific physical process or data treatment, which can be assembled according to the needs of a particular simulation. This modularity ensures that ASTRA can be easily adapted and expanded as new experimental requirements or theoretical developments arise [35].

ASTRA solves a set of coupled, time-dependent, one-dimensional transport equations for the plasma quantities:  $n_e$ ,  $T_e$ ,  $T_i$  and poloidal magnetic flux  $\Psi$ . The general form of these equations is:

$$S_e = \frac{1}{V'} \left( \frac{\partial}{\partial t} - \frac{\dot{B}_0}{2B_0} \frac{\partial}{\partial \rho} \rho \right) (V' n_e) + \frac{1}{V'} \frac{\partial}{\partial \rho} \Gamma_e$$
 (11)

$$P_e = \frac{3}{2} (V')^{-5/3} \left( \frac{\partial}{\partial t} - \frac{\dot{B}_0}{2B_0} \frac{\partial}{\partial \rho} \rho \right) \left[ (V')^{5/3} n_e T_e \right] + \frac{1}{V'} \frac{\partial}{\partial \rho} \left( q_e + \frac{5}{2} T_e \Gamma_e \right)$$
(12)

$$P_{i} = \frac{3}{2} (V')^{-5/3} \left( \frac{\partial}{\partial t} - \frac{\dot{B}_{0}}{2B_{0}} \frac{\partial}{\partial \rho} \rho \right) \left[ (V')^{5/3} n_{i} T_{i} \right] + \frac{1}{V'} \frac{\partial}{\partial \rho} \left( q_{i} + \frac{5}{2} T_{i} \Gamma_{i} \right)$$
(13)

$$\sigma_{\parallel} \left( \frac{\partial \psi}{\partial t} - \frac{\rho \dot{B}_0}{2B_0} \frac{\partial \psi}{\partial \rho} \right) = \frac{J^2 R_0}{\mu_0 \rho} \frac{\partial}{\partial \rho} \left( \frac{G_2}{J} \frac{\partial \psi}{\partial \rho} \right) - \frac{V'}{2\pi \rho} (j_{BS} + j_{CD}) \tag{14}$$

where  $V' = \frac{\partial V}{\partial \rho}$  is the derivative of the plasma volume with respect to the radial coordinate  $\rho$ ,  $\Gamma_e$  and  $\Gamma_i$  are the electron and ion particle fluxes,  $q_e$  and  $q_i$  are the electron and ion heat fluxes, and  $P_e$  and  $P_i$  are the electron and ion heating power densities. The last equation describes the evolution of the poloidal flux, including contributions from bootstrap and driven currents [35].

The ASTRA code assumes a general structure for the transport matrix. It includes the electron and ion heat diffusivities  $\chi_e$ ,  $\chi_i$  and the particle diffusivity  $D_n$  and is written as:

$$\begin{pmatrix}
\frac{\Gamma_e}{n_e} \\
\frac{q_e}{n_e T_e} \\
\frac{q_i}{n_i T_i} \\
V'G_1 \frac{\mu_0 j_{BS}}{B_p}
\end{pmatrix} = -V'G_1 \begin{pmatrix}
D_n & \chi_e^n & \chi_n^i & C_n \\
D_e & \chi_e & \chi_e^i & C_e \\
D_i & \chi_i^e & \chi_i & C_i \\
D_E & \chi_E^e & \chi_E^i & 0
\end{pmatrix} \begin{pmatrix}
\frac{1}{n_e} \frac{\partial n_e}{\partial r} \\
\frac{1}{T_e} \frac{\partial T_e}{\partial r} \\
\frac{1}{T_i} \frac{\partial T_i}{\partial r} \\
\frac{E_{\parallel}}{B_p}
\end{pmatrix}$$
(15)

where  $G_1 = \langle (\nabla \rho)^2 \rangle$  is a geometric factor that stands for the flux surface average of the plasma in a tokamak and  $E_{\parallel}$  is the parallel electric field. (Note: The transport matrix in the original paper [35] contains an error in equation (60). The correct form is

given in the ASTRA notation in equation (87), but the variable translation in Table 4.5 is again inconsistent.)

All coefficients in the upper left  $3\times 3$  block of the transport matrix have the units of  $\mathrm{m}^2/\mathrm{s}$ , while the coefficients in the rightmost column and bottom row are dimensionless. Here,  $B_p$  denotes the average poloidal magnetic field, which is defined as  $B_p = \frac{1}{2\pi R_0} \frac{\partial \Psi}{\partial \rho}$ . This formalism allows ASTRA to flexibly incorporate a wide range of transport models and to couple particle, heat, and current transport in a consistent framework.

In the context of this thesis, ASTRA is firstly used as a guidline on how the initial implementation of diffusive transport coeffcient  $\chi_e$  and  $\chi_i$  calculation shall be facilitated and later serves as validation to check proper implementation in the IDA/IDE framework through comparison.

# 2.7 Diffusive Heat Transport

This section outlines the fundamental equations governing diffusive heat transport, which typically describe how heat energy moves within the plasma based solely on local properties. However, both experimental observations and theoretical studies have demonstrated that plasma regions can interact over much larger distances and on timescales faster than those predicted by classical diffusion [12]. As a result, the heat flux at a given location may also be affected by changes in plasma parameters elsewhere in the device. Accurately modeling and automating these complex, non-local transport processes within the IDE framework is beyond the scope of this thesis. Instead, we focus on a simplified, yet broadly applicable, approach to transport modeling and evaluate its ability to capture essential features of plasma behavior.

### 2.7.1 Energy conservation and heat flux

The starting point for understanding heat transport is the energy conservation law for a plasma volume. The temporal change in energy of a certain plasma volume  $\frac{\partial E}{\partial t}$  is given by

$$\frac{\partial E}{\partial t} = -\oint \vec{q} \cdot d\vec{A} + \int S \, dV. \tag{16}$$

The first term on the right side integrates the heat flux  $\vec{q}$  over the closed plasma surface. The second term integrates the energy sources and sinks S over the plasma volume. For a fusion plasma, S is defined by its energy sources like external heating, heating from the fusion reactions as well as energy losses (sinks) due to radiation or particle loss.

By introducing the energy density w and applying the divergence theorem to convert the surface integral into a volume integral with  $\nabla \cdot \vec{q}$ , the integral equation can be transformed into a differential equation

$$\frac{\partial w}{\partial t} = -\nabla \cdot \vec{q} + S. \tag{17}$$

Diffusive heat transport is primarily driven by spatial temperature gradients as described by Fourier's law of thermal conduction

$$\vec{q} = -\kappa \nabla T. \tag{18}$$

Introducing the heat conductivity  $\kappa = n\chi$  into equation (18) Fourier's law of thermal conduction can be expressed as

$$\vec{q} = -n\chi \nabla T \tag{19}$$

where n represents the density and  $\chi$  represents the diffusion coefficient with the physical unit  $m^2/s$ .

The direction of magnetic field lines play a crucial role in determining transport characteristics, as already discussed in section 2.3. Parallel to the magnetic field, particles in the plasma can move freely and the heat conductivity is so large that, in practice, no temperature gradients can build up along closed field lines. This results in the plasma being in thermal equilibrium toroidally, with temperature remaining constant on each

magnetic flux surface. In contrast, transport across magnetic field lines (perpendicular direction) is significantly slower and more restricted. Therefore we consider only radial transport which occurs perpendicular to magnetic flux surfaces. Consequently, all vector quantities can be expressed as their scalar magnitudes since both heat and particle fluxes are directed parallel to the normal vector of the magnetic flux surface. This allows us to define the total power flowing over a magnetic flux surface Q as [37]

$$Q = \int \vec{q}d\vec{A} = \int qdA. \tag{20}$$

Resulting Fourier's law of thermal conduction to be rewritten as

$$q(\rho) = -n(\rho)\chi(\rho)\nabla T(\rho) = \frac{Q(\rho)}{A(\rho)}$$
(21)

with  $A(\rho)$  being the area of the magnetic flux surface at a given radial coordinate  $\rho$ . Using the aforementioned equations we can express the transport coefficient as

$$\chi(\rho) = -\frac{Q(\rho)}{n(\rho)\nabla T(\rho)A(\rho)} = -\frac{S(\rho) - \frac{\partial w}{\partial t}(\rho)}{n(\rho)\nabla T(\rho)A(\rho)}$$
(22)

leaving us with a single equation to calculate the transport coefficient  $\chi$  at a given radial coordinate  $\rho$  applicable for electrons or ions respectively. Here,  $S(\rho)$  is the sources and sinks term,  $\frac{\partial w}{\partial t}(\rho)$  is the temporal change of energy density,  $n(\rho)$  is the particle density,  $\nabla T(\rho)$  is the temperature gradient and  $A(\rho)$  is the area of the magnetic flux surface at that radial coordinate.

### 2.7.2 Calculation of the transport coeffcient

The calculation of transport coefficients requires addressing several unknowns through appropriate assumptions and simplifications. Each component of equation (22) presents distinct challenges and considerations.

The radial profiles of density and temperature are obtained through direct measurements (see section 3.3). While these diagnostics provide reliable data, measurement uncertainties inevitably propagate into the final transport coefficient calculations. The quality of these profiles is therefore crucial for obtaining physically meaningful results.

For the sources and sinks term S, we employ a comprehensive power balance approach as described in section 4.1. This method quantifies all significant energy input and loss mechanisms.

The temporal change of energy density  $\frac{\partial w}{\partial t}$  requires careful consideration of the plasma's time evolution. Two primary approaches are commonly employed in plasma transport analysis.

# Steady-state assumption $\frac{\partial w}{\partial t} = 0$ :

For simplification, it is often assumed that the energy contained in the plasma remains constant, yielding  $\frac{\partial w}{\partial t} = 0$ . This steady-state assumption is valid for quasi-steady plasma conditions and enables straightforward analysis for a pertimepoint basis when continuity of the contained energy is ensured. However, this approach becomes invalid during transient processes where the energy content in the plasma inherently changes, such as during heating system activation or deactivation, plasma ramp-up and ramp-down phases, and major disruptions or instabilities.

# Transient condition assumption $\frac{\partial w}{\partial t} = \frac{\partial}{\partial t}(nT)$ :

To facilitate analysis during transient conditions, the energy change can be calculated using the stored thermal energy. The magnetohydrodynamic energy content  $W_{MHD}$  is computationally challenging to determine, and several methods exist for its calculation. In equilibrium reconstructions, it is common practice to solve the Grad-Shafranov equation (see section 2.3) to obtain the total plasma pressure profile p, which is then integrated over the plasma volume  $V(\rho)$  to determine the total energy content [38, 39]

$$W_{MHD} = \frac{3}{2} \int_{V(\rho)} p dV. \tag{23}$$

However, this exact computation is computationally too complex for our application. Therefore, we utilize the relationship from the ideal gas law pV = nRT and recognize that changes in pressure p are proportional to changes in the product  $n \cdot T$  for constant V. This approximation in combination with equation(23) allows us to express the temporal change of  $W_{MHD}$  as  $\frac{\partial w}{\partial t} = \frac{\partial}{\partial t}(nT)$  for each flux surface.

### 2.7.3 Interpretation of the transport coeffcient

The transport coefficient or diffusion coefficient is the commonly used quantity determined by transport models and has the unit  $m^2/s$ . It can be understood as the rate at which a concave temperature profile smooths itself out essentially meaning how quickly a bump becomes flat.

It is important to note that the transport coefficient is derived from several plasma parameters which are either measured or calculated under certain assumptions and boundary conditions. This is not necessarily problematic, but deviations, uncertainties and errors of these parameters propagate into the resulting transport coefficient, leading to erroneous or unphysical descriptions, which is important to be aware of.

One of the most prominent cases is when the diffusive coefficient  $\chi$  becomes negative, essentially indicating that heat flows against the temperature gradient, which is fundamentally impossible from a physical standpoint. This phenomenon can occur in our model through different phenomena which lead to major temporal differences in density and temperature profiles, causing a high  $\frac{\partial w}{\partial t}$  and thus a sign change in the numerator of equation (22).

Another important aspect to consider is the dependency of the denominator to the temperature gradient  $\nabla T$ . As the temperature profile is measured by several different diagnostics (see section 3.3) each with different certainty along the radial profile it

needs to get stitched together for the best result. This leads to smoothing constraints needed between the different sections. In this case, the denominator of equation (22) can become very small as well as go through zero and flip signs, which in turn leads to very prominent spikes in the transport coefficient profile.

# 2.8 Gaussian Process Regression (GPR)

A natural concern with the idea of modeling functions directly is that there are infinitely many possible functions—how can we possibly compute with such an enormous set in practice? This is where the concept of a Gaussian process becomes useful.

A Gaussian process is a generalization of the familiar Gaussian (normal) probability distribution. While a probability distribution describes uncertainty over scalars or vectors, a stochastic process like a Gaussian process describes uncertainty over functions.

To build some intuition, imagine a function as a very long vector, where each entry gives the value f(x) at a particular input x. Although this is a somewhat naive picture, it is surprisingly close to how Gaussian processes actually work: they allow us to reason about distributions over functions in a way that is both mathematically rigorous and computationally tractable [40, 41].

### A Pictorial Introduction to Gaussian Process Regression

To build intuition for GPR, it helps to visualize how GPR models uncertainty over functions.

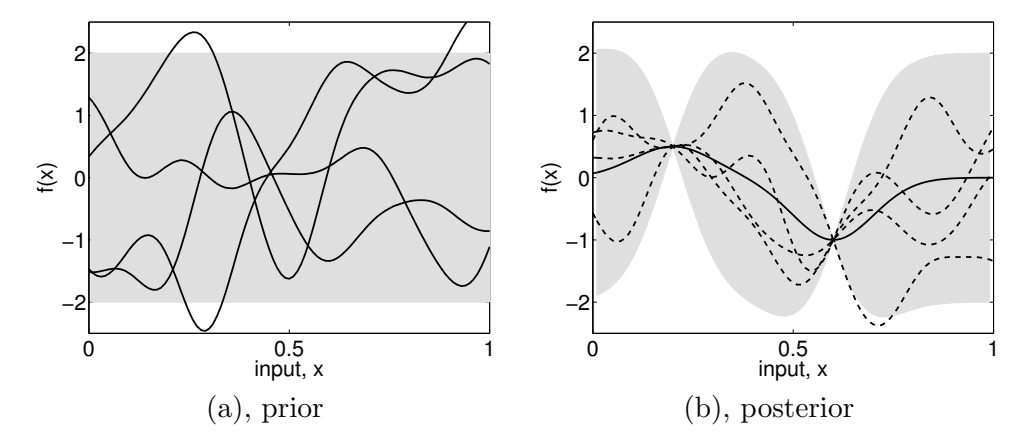


Figure 6: Panel (a): Four random functions sampled from the GP prior distribution. Panel (b): After observing two data points, the mean prediction (solid line) and four samples from the posterior (dashed lines) are shown. The shaded area in both plots shows twice the standard deviation at each value x. Taken from [40].

The left Panel of Figure 6 shows several functions randomly drawn from a Gaussian process prior, representing our initial beliefs about possible functions before seeing any data. The right Panel (b) of Figure 6 shows what happens after observing two data points. Now, only functions that pass through these points are considered likely. The mean prediction is shown as a solid line, and the uncertainty is greatly reduced near the observations. The dashed lines are samples from the posterior distribution, reflecting the updated beliefs after seeing data.

This pictorial example illustrates how GPR combines prior assumptions with observed data to produce both predictions and uncertainty estimates in a principled, Bayesian way [40].

#### Gaussian Processes: From Vectors to Functions

A Gaussian process (GP) generalizes the concept of a multivariate normal distribution to functions. Instead of a finite-dimensional mean vector and covariance matrix, a GP is defined by a mean function m(x) and a covariance (kernel) function k(x, x'):

$$f(x) \sim \mathcal{GP}[m(x), k(x, x')]$$
 (24)

In general it can be interpreted as a normal distribution of functions for which any finite set of points  $x_1, ..., x_N$ , the function values  $[f(x_1), ..., f(x_N)]$  are jointly Gaussian distributed:

$$\begin{bmatrix} f(x_1) \\ \vdots \\ f(x_N) \end{bmatrix} \sim \mathcal{N} \left( \begin{bmatrix} m(x_1) \\ \vdots \\ m(x_N) \end{bmatrix}, \begin{bmatrix} k(x_1, x_1) & \cdots & k(x_1, x_N) \\ \vdots & \ddots & \vdots \\ k(x_N, x_1) & \cdots & k(x_N, x_N) \end{bmatrix} \right)$$
(25)

The kernel function k(x, x') encodes the expected correlation between function values at x and x'. Common choices include the squared exponential kernel, Ornstein-Uhlenbeck [42] and Gaussian noise kernels, each controlling the smoothness and variability of sampled functions [40].

### Gaussian Process Regression: Conditioning on Data

Given noisy measurements  $\mathbf{y} = [f(x_1), ..., f(x_n)]^T$  at points  $x_1, ..., x_n$ , we assume a Gaussian likelihood prior for the underlying function f(x). The posterior over observed and test points is:

$$\begin{bmatrix} \mathbf{y} \\ \mathbf{f}_* \end{bmatrix} \sim \mathcal{N} \left( \begin{bmatrix} \boldsymbol{\mu}_y \\ \boldsymbol{\mu}_* \end{bmatrix}, \begin{bmatrix} K_{xx} + \sigma^2 I & K_{xx^*} \\ K_{x^*x} & K_{x^*x^*} \end{bmatrix} \right)$$
(26)

where  $\mathbf{f}_*$  are the function values at new (test) points,  $K_{xx}$  is the covariance matrix for the observed points, and  $\sigma^2$  is the measurement noise variance.

Conditioning on the observed data, the posterior mean and covariance at the test points are:

$$\boldsymbol{\mu}_{\text{post}} = \boldsymbol{\mu}_* + K_{x^*x} (K_{xx} + \sigma^2 I)^{-1} (\mathbf{y} - \boldsymbol{\mu}_y)$$
 (27)

$$\Sigma_{\text{post}} = K_{x^*x^*} - K_{x^*x}(K_{xx} + \sigma^2 I)^{-1} K_{xx^*}$$
(28)

This yields both the best-fit function and a principled estimate of uncertainty at each point [40]. Figure 7 illustrates the posterior with an added error to the measurements.

## Hyperparameters and Model Selection

The kernel hyperparameters, such as the length scale l in the SE kernel, control the flexibility of the fit. Small l allows rapid variation (risking overfitting), while large l enforces smoothness (risking underfitting). Hyperparameters are typically optimized by maximizing the marginal likelihood of the data [40, 43].

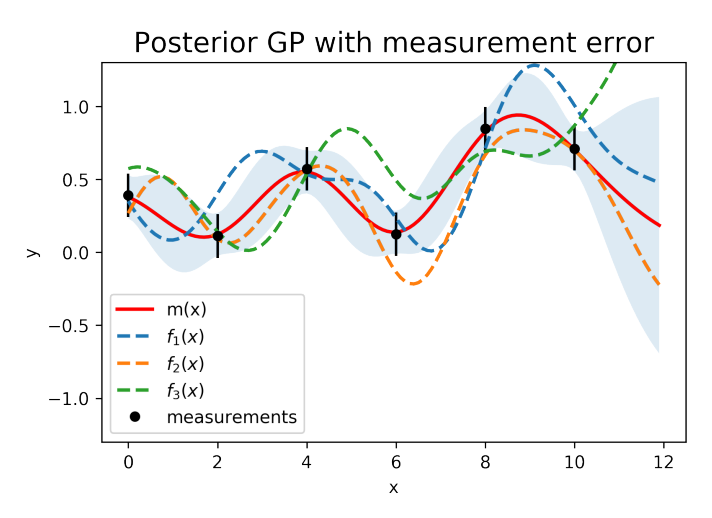


Figure 7: Posterior Gaussian process after including a measurement error. The sampled functions now accurately reflect the uncertainty introduced by the measurement noise. (Taken from [44])

### Application to Tomography

A GPR-based approach was used to develop the Gaussian Process Tomography (GPT) method in [44, 45], aiming to reconstruct emission distributions from bolometer measurements. This code was implemented in Python and the models hyperparameters were specifically optimized for inferring radiative emission through tomographic analysis of bolometer data from the ASDEX Upgrade tokamak. The general process is illustrated in Figure 8.

To obtain the radial emission profile, each pixel in the tomographic reconstruction is mapped to its corresponding magnetic coordinate  $\rho$ . The pixels are subsequently grouped into ten equally spaced radial bins spanning from  $\rho = 0$  to  $\rho = 1$ . Within each bin, the contribution from all pixels is summed and integrated according to:

$$P_{\text{rad,bin}} = 2\pi dr dz \sum_{i} R_{i} E_{i} \quad \text{with} \quad \rho_{\text{bin,min}} < \rho_{i} < \rho_{\text{bin,max}}$$
 (29)

where dr and dz represent the pixel dimensions in the radial and vertical directions,  $R_i$  is the major radius of the *i*-th pixel, and  $E_i$  is its emission density in  $W/m^3$ .

This binning procedure yields emission profile values at ten discrete  $\rho$  locations. The complete radial profile can subsequently be constructed by an interpolation between these points [43].

### Implementation in IDE

In this thesis, GPT is employed to automatically reconstruct radiation profiles from noisy bolometer measurement data. This approach yields the most reliable radiation profiles and is a fully autonomous method which is a necessity for the application within IDE. To integrate this capability into the IDE framework, the GPR/GPT method was ported to Fortran90 and incorporated into the existing IDE codebase. Throughout that process a fundamental issue within the profile generation procedure arose which will be discussed further in section 4.3. The porting into Fortran90 ensures high computational performance while ensuring compatibility with the established code infrastructure and preserving language familiarity for the existing maintainer.

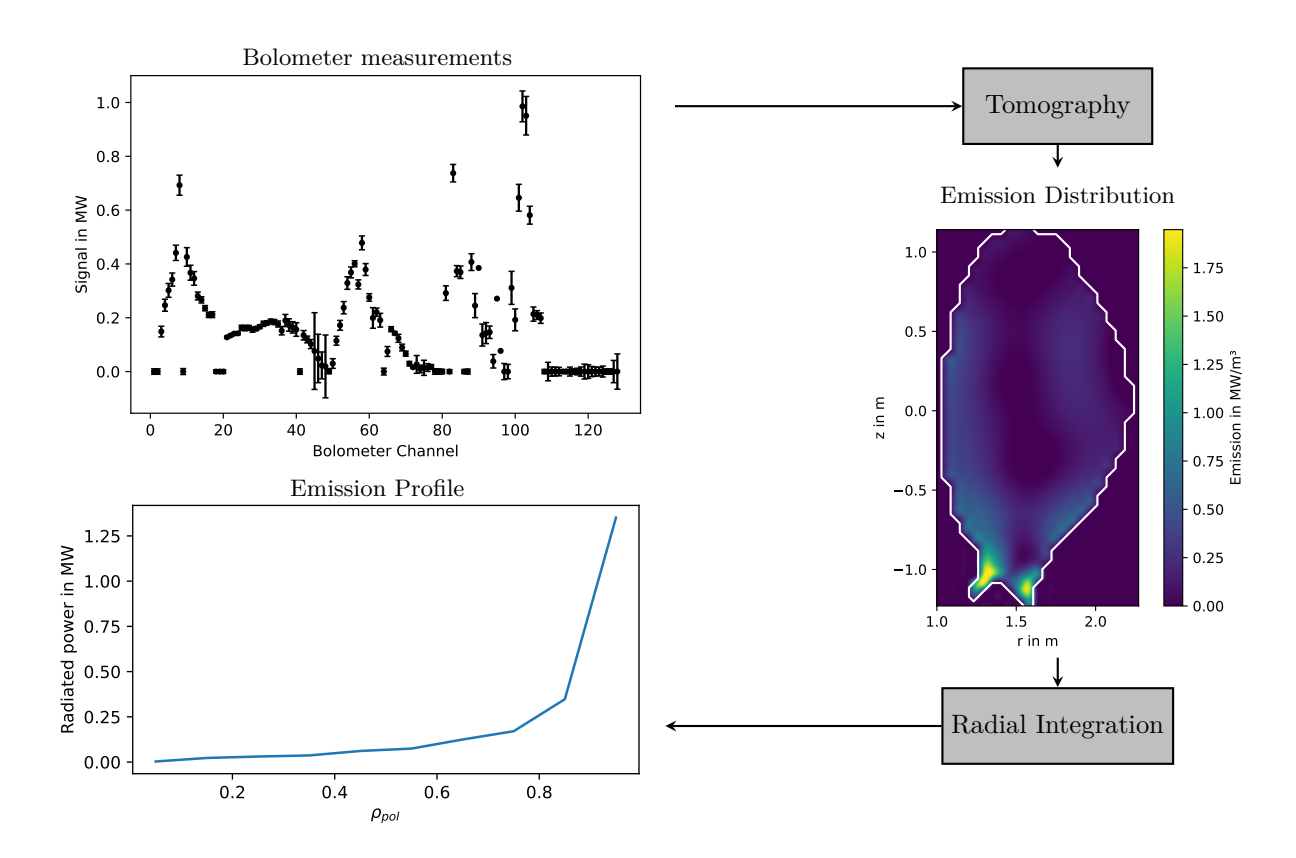


Figure 8: Overview of the Gaussian Process Tomography workflow on an example discharge #33616 at 7s. Initially, bolometer data is loaded and preprocessed. Subsequently, Gaussian Process Tomography is applied to reconstruct a two-dimensional emission tomogram. Finally, the tomogram is radially integrated to obtain the radiated power profile as a function of plasma radius. (Adapted from [43].)

# 3 Experimental Background

"Any sufficiently advanced technology is indistinguishable from magic."

— Arthur C. Clarke

# 3.1 ASDEX Upgrade

The "Axially Symmetric Divertor Experiment-Upgrade" (ASDEX-Upgrade) is a magnetic confinement fusion (MCF) research tokamak located in Garching near Munich, Germany. ASDEX-Upgrade is a medium-sized tokamak with a major radius of 1.65 m, a minor radius of 0.5 m and the vacuum chamber walls fully coated in tungsten. It aims to study the behaviour of high-temperature plasma being confined by strong magnetic fields to gain insights for future fusion projects like ITER and DEMO [46, 47].

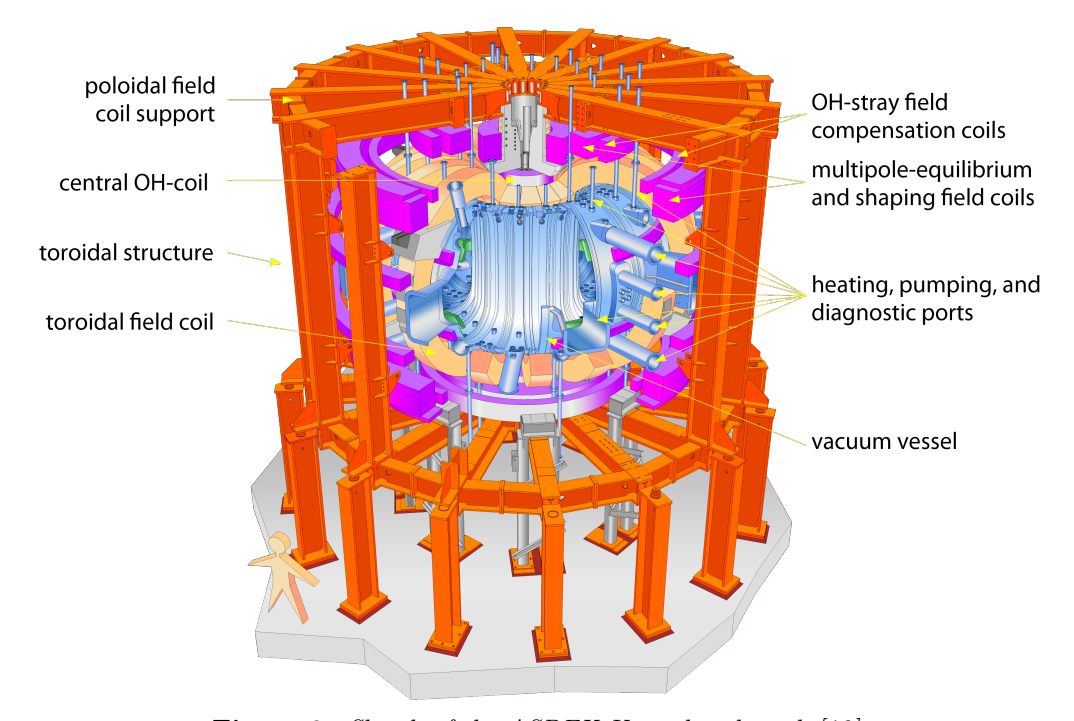


Figure 9: Sketch of the ASDEX Upgrade tokamak [48].

For the calculation of diffusive transport coefficients described in this thesis, precise knowledge of all energy sources and sinks in the plasma is essential. The power balance equations (see section 4.1) require accurate determination of heating power deposition profiles from various heating systems, as well as reliable measurements of plasma density and temperature profiles from diagnostic systems. Additionally, energy losses through radiation must be properly quantified. The following sections describe the heating methods, diagnostic techniques, and radiation measurements used at ASDEX Upgrade that provide the necessary input data for transport coefficient calculations.

# 3.2 Heating

This section provides a brief overview of several heating methods used in fusion engineering, all of which are applied at the ASDEX Upgrade tokamak.

### 3.2.1 Neutral Beam Injection - NBI

Neutral Beam Injection (NBI) is an effective technique for heating plasma in magnetic confinement fusion devices. It involves injecting a beam of high-energy neutral atoms into the plasma. The process begins by ionizing particles and accelerating them to high energies using electrostatic or electromagnetic fields. Before entering the reactor vessel, the ions pass through a neutralizing chamber, where they undergo charge exchange reactions with a neutralizing gas to become neutral atoms. This neutrality is crucial for the beam to penetrate the magnetically confined plasma without being deflected. Once inside the plasma, the neutral atoms are re-ionized and transfer their energy through Coulomb collisions to the plasma particles. In addition to efficient energy deposition, NBI also contributes to current drive and profile shaping [10, 49]. The energy deposition and driven current is estimated within this work with the RABBIT code [50].

### 3.2.2 Electron Cyclotron Resonance Heating - ECRH

Electron Cyclotron Resonance Heating (ECRH) uses electromagnetic waves in the microwave frequency range to heat the plasma. High-frequency (GHz) microwaves are generated by gyrotrons and directed into the plasma using mirrors and waveguides. These microwaves interact resonantly with plasma particles gyrating at the cyclotron frequency, transferring energy to them. The cyclotron frequency depends on the magnetic field strength at a specific location, which varies with the radius [10, 22]. There are 8 gyrotrons installed at the ASDEX Upgrade providing radiation at either 140 GHz or 105 GHz and a total heating power of up to 6.5 MW [51]. The energy deposition and driven current from the microwaves are estimated with the TORBEAM code [52].

### 3.2.3 Ion Cyclotron Resonance Heating - ICRH

Ion Cyclotron Resonance Heating (ICRH) employs radio-frequency waves in the MHz range to heat the plasma. The principle is similar to ECRH, but the resonant interaction targets ions instead of electrons. Unlike microwaves, radio-frequency waves are more challenging to transport and must be transmitted into the plasma using antennas positioned near the plasma edge. This requirement complicates the reactor vessel design, as interactions between the plasma and the antenna must be minimized.

The waves are tuned to match the ion cyclotron frequency, which corresponds to the frequency at which ions gyrate around magnetic field lines. Through resonant interaction, the waves transfer energy to the ions, heating the plasma [10]. Typically a hydrogen minority heating scheme is employed, where a small fraction of hydrogen ions in the deuterium plasma efficiently absorbs the radio-frequency power [53]. At ASDEX Upgrade, the ICRH system uses frequencies in the 30-60 MHz range and is capable of providing another 6-7 MW of heating power [54].

The waves are tuned to match the ion cyclotron frequency, which corresponds to the frequency at which ions gyrate around magnetic field lines. Through resonant interaction, the waves transfer energy to the ions, heating the plasma [10]. At ASDEX Upgrade, the ICRH system typically employs the hydrogen minority heating scheme, where a small fraction of hydrogen ions in a deuterium plasma efficiently absorbs the radio-frequency power. The system uses frequencies in the 30–60 MHz range and is capable of providing another 6–7 MW of heating power [54].

# 3.3 Diagnostics

This section provides a brief overview of the key diagnostics used to determine the density and temperature profiles at the ASDEX Upgrade tokamak.

### 3.3.1 Electron Cyclotron Emission - ECE

Electron Cyclotron Emission (ECE) diagnostics are used to measure the electron temperature  $T_e$  of the plasma. In a magnetized plasma, electrons gyrate around magnetic field lines and emit synchrotron radiation in the process. The frequency of this radiation is directly linked to the local magnetic field strength, which decreases with increasing radius. By analyzing the intensity of the emitted radiation across various frequencies, the electron temperature profile as a function of radius can be determined [55, 56].

### 3.3.2 Deuterium Cyanide Laser Interferometry - DCN

Deuterium Cyanide Laser Interferometry (DCN) diagnostics measure the electron density  $n_e$  by detecting the phase shift of a laser beam as it traverses the plasma. At the ASDEX Upgrade tokamak, this phase shift is measured using a Mach–Zehnder interferometer with a deuterium cyanide laser operating at a wavelength of 195  $\mu m$ . For this wavelength, a phase shift of  $2\pi$  corresponds to an integrated line density of  $5.72 \times 10^{18} \text{electrons/m}^{-2}$ . A challenge with this method is the occurrence of "fringe jumps," where phase shifts are miscounted in multiples of  $2\pi$  [57].

### 3.3.3 Lithium Beam Emission Spectroscopy - Li-BES

Lithium Beam Emission Spectroscopy (Li-BES) diagnostics measure electron density profiles in the outer plasma region. This method involves injecting a beam of lithium atoms into the plasma, where the atoms are excited and subsequently de-excited. During the de-excitation from the  $Li_{2p}$  to the  $Li_{2s}$  state, photons with a wavelength of 670.8 nm are emitted. By measuring the intensity of this emission, the electron density can be determined. Since the lithium beam is attenuated by the plasma, an attenuation model must be applied to the measurements. As a result, Li-BES is most accurate for regions near the plasma edge, such as the Scrape-Off Layer (SOL) [58, 59].

### 3.3.4 Thomson Scattering - TS

Thomson Scattering (TS) diagnostics measure both the electron density  $n_e$  and temperature  $T_e$  by analyzing the scattering of laser light by free electrons in the plasma. The scattered light undergoes a Doppler shift due to electron motion, resulting in a broadened spectrum. This spectrum is analyzed to determine the electron temperature, while the intensity of the scattered light provides the electron density. TS can be used for both the plasma edge and core. However, accurate measurements require precise calibration, with absolute calibration needed for density measurements and relative calibration for temperature measurements [60].

### 3.3.5 Charge Exchange Recombination Spectroscopy - CXRS

Charge Exchange Recombination Spectroscopy (CXRS) diagnostics are used to measure ion properties in the plasma. This method relies on the light emitted during charge exchange reactions between neutral particles (D) and ionized impurity atoms  $(A^{Z+})$ :

$$A^{Z+} + D \to A^{(Z-1)+*} + D^{+} \to A^{(Z-1)+} + h\nu + D^{+}.$$
 (30)

Neutral particles are typically introduced into the plasma via neutral beam injection or gas puffing. These particles exchange electrons with impurity ions, exciting them. The subsequent de-excitation of the ions emits photons with characteristic wavelengths. By analyzing the emitted spectrum, the ion temperature  $T_i$  can be determined from the Doppler width, the flow velocity from the Doppler shift, and the impurity density from the emission line radiance [61, 62].

CXRS assumes that the excited impurity ions  $A^{Z+}$  share the same energy, velocity, and temperature as the bulk ions [63].

#### 3.3.6 Bolometers

Bolometers measure the total radiated power emitted by the plasma across the electromagnetic spectrum. ASDEX Upgrade employs both foil and diode bolometer systems, each with distinct advantages and limitations. Diode bolometers, based on semiconductor technology, offer superior temporal resolution enabling measurements in the sub-millisecond regime, but suffer from challenging calibration procedures. In contrast, foil bolometers provide more reliable absolute measurements and are used primarily in this work.

Foil bolometers operate using a thin gold foil with uniform absorption characteristics across the plasma's emission spectrum. The absorbed radiative power heats the foil, causing a measurable change in its electrical resistance that is proportional to the temperature increase. This resistance change directly correlates with the incident radiated power, enabling quantitative power measurements [64, 65].

The bolometer diagnostic system at ASDEX Upgrade comprises three primary camera arrays: a horizontal array with 48 channels, a vertical array with 32 channels, and a divertor-mounted array with 28 channels. While additional cameras with fewer channels have been installed over time (red lines in Figure 10), they were excluded from the GPT analysis due to limited availability across the discharge database or significant geometric changes between experimental campaigns [43].

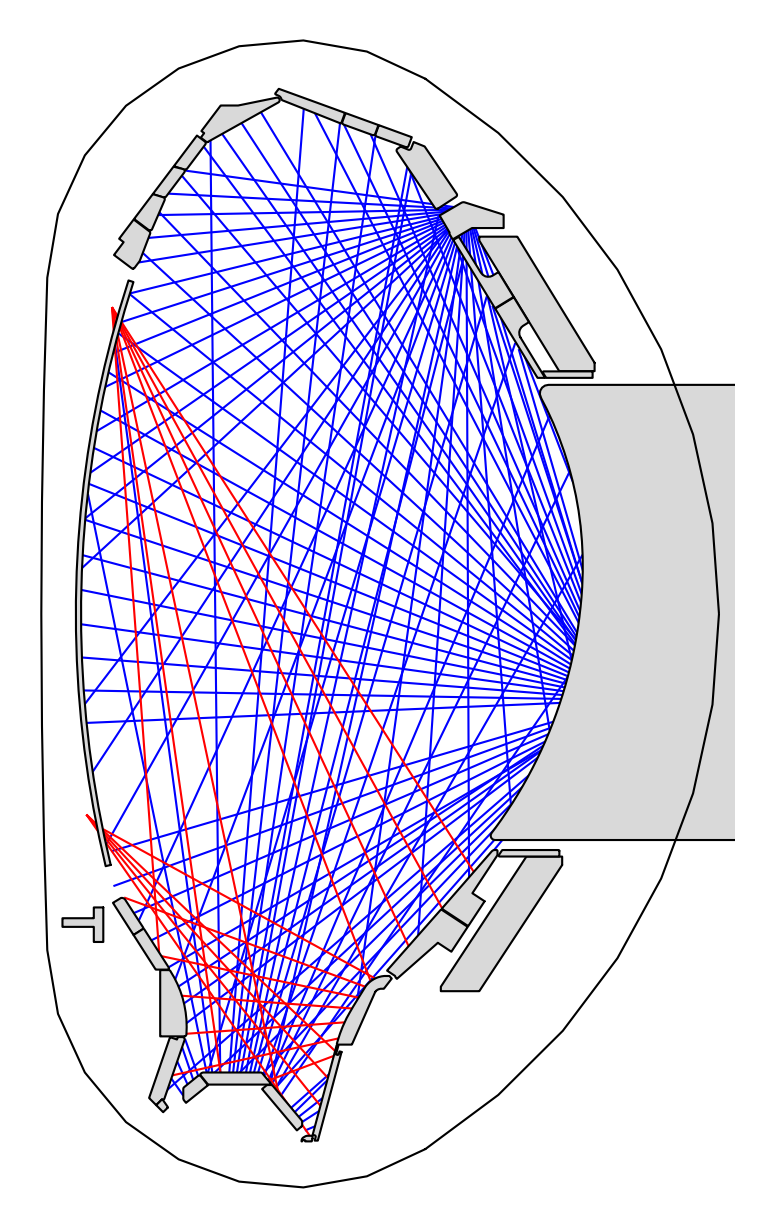


**Figure 10:** Lines of sight for the bolometer channels. The blue lines respirent channels FHC, FVC and FDC. The red lines are FLX, FLH and FHS and were excluded in the GPT analysis.

# 4 Transport coefficient calculation implementation

"Talk is cheap. Show me the code."

— Linus Torvalds

The module mod\_coefficients\_model.f90 within the IDE framework is responsible for calculating the transport coefficients in the plasma after the equilibrium is calculated. It computes the electron and ion heat diffusivities  $\chi_e$  and  $\chi_i$  as well as a combination of the two called the effective heat diffusivity  $\chi_{eff}$ . The formulas defining the calculation are based on the implementation of the heat diffusivities of ASTRA. The equations are based on diffusive transport theory as explained in section 2.7, combined with empirical formulas (e.g., tungsten and carbon radiation profiles) derived from experimental data in tokamak plasmas. This will subsequently be improved upon in section 4.3 which introduces a method to calculate the radiative loss from bolometer measurements. The entire module is implemented in Fortran90. Figure 11 provides a flowchart overview of the calculation process, with each quantity and processing step explained in detail in the following sections.

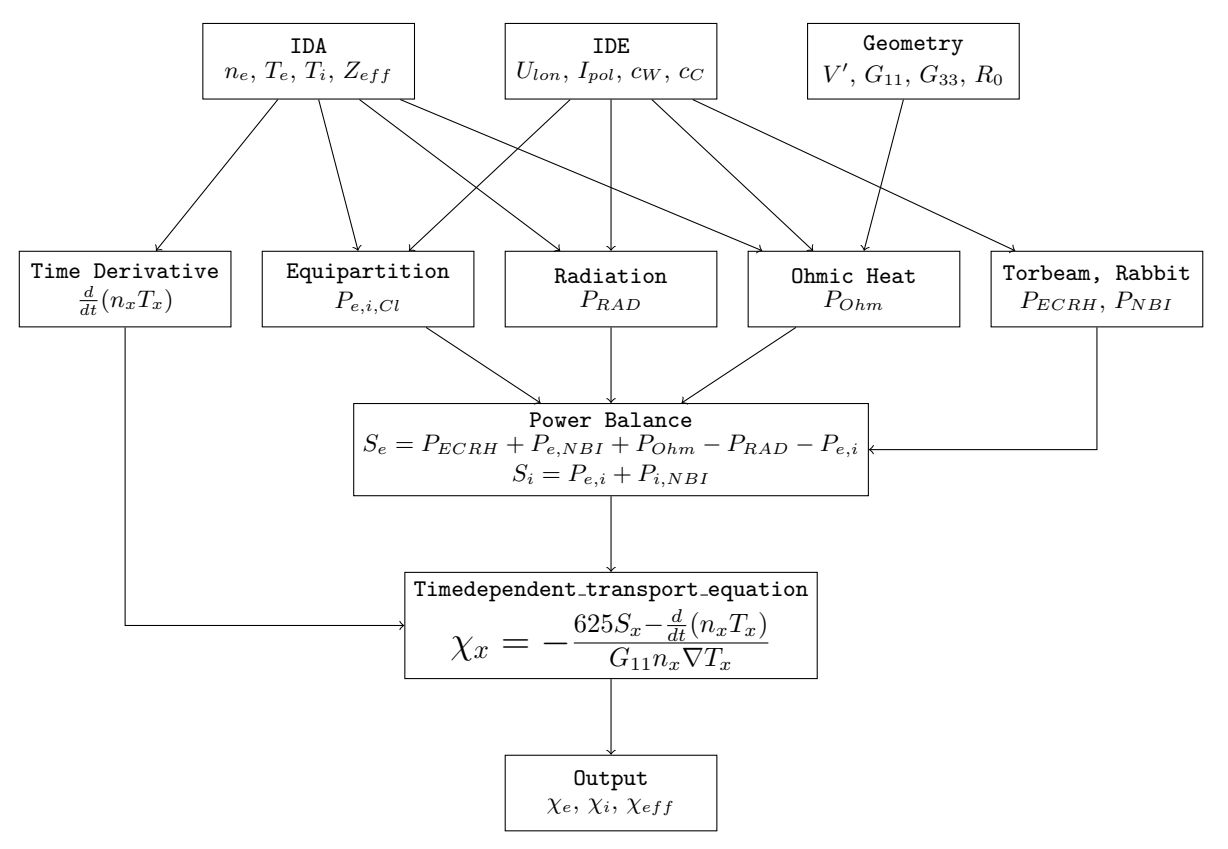


Figure 11: Flow of data within the mod\_coefficients\_model.f90 module for calculating diffusive transport coefficients.

#### 4.1 Summary of the mod\_coefficients\_model.f90 Module

The calculation of heat diffusivities is based on the equations derived in section 2.7. This process is performed incrementally over  $\rho_{tor}$ , evaluating the net power flow for each plasma volume element.

To accomplish this, we must determine all energy sources and sinks affecting each plasma volume element. This analysis requires establishing separate power density equations which quantify all energy sources and sinks for electrons and ions respectively as a function of  $\rho_{tor}$ . We define them as

$$S_e = P_{ECRH} + P_{e,NBI} + P_{Ohm} - P_{RAD} - P_{e,i}$$
 (31)

$$S_i = P_{e,i} + P_{i,NBI} \tag{32}$$

where  $P_{\text{ECRH}}$ ,  $P_{\text{NBI}}$ , and  $P_{\text{Ohm}}$  are the heating powers deposited by ECRH, NBI, and ohmic heating, respectively,  $P_{\text{RAD}}$  is the radiative power loss, and  $P_{e,i}$  represents the electron-ion heat exchange due to Coulomb collisions. The ion sources and sinks  $S_i$  are derived from the electron-ion heat exchange  $P_{e,i}$  and the power deposited onto ions by neutral beam injection  $P_{i,NBI}$ . Currently,  $P_{\text{ICRH}}$  is not included in the model since we lack a sufficiently accurate and computationally efficient method to determine the ICRH power deposition per volume element. Surrogate models are currently under development to address this limitation and are planned to be implemented in future versions [66, 67].

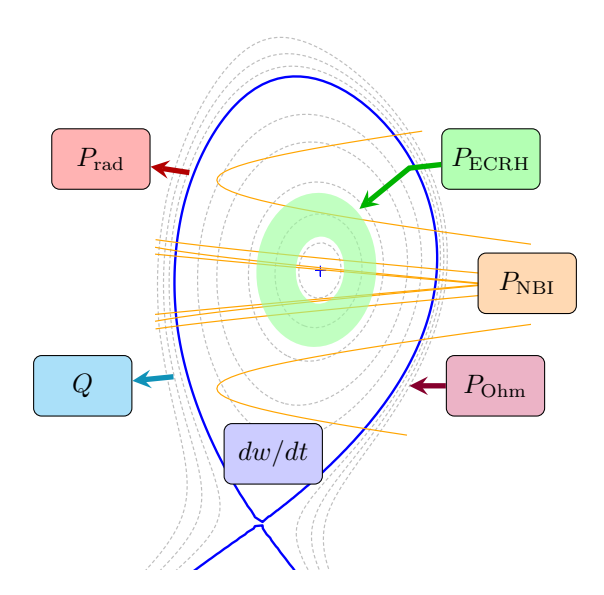


Figure 12: Poloidal cross-section of IDE equilibrium #33616 at t=3.0s illustrating the power balance equation in a tokamak plasma. The figure shows nested magnetic flux surfaces with the separatrix (blue line) defining the plasma boundary, NBI heating trajectories (orange lines), and the ECRH heating region (green shaded area). Power flows are indicated by arrows: heating sources ( $P_{ECRH}$ ,  $P_{Ohm}$ ,  $P_{NBI}$ ) on the right, power losses through radiation ( $P_{rad}$ ) and conducted heat flux (Q) on the left and the temporal change in stored plasma energy ( $\frac{dw}{dt}$ ) at the bottom.

With a schematic illustrated in Figure 12 we can now define our power balance equations in combination with the transient condition assumption  $\frac{dw}{dt} = \frac{d}{dt}(n_e T_e)$  from section 2.7.2 as:

$$Q_e + \frac{d}{dt}(n_e T_e) \approx S_e = P_{ECRH} + P_{e,NBI} + P_{Ohm} - P_{RAD} - P_{e,i}$$
(33)

$$Q_i + \frac{d}{dt}(n_i T_i) \approx S_i = P_{e,i} + P_{i,NBI}. \tag{34}$$

The heating power supplied to the plasma must be balanced by three fundamental processes: absorption by the plasma, resulting in an increase in stored energy  $(\frac{d}{dt}(nT))$ ; transport to colder plasma regions as conducted heat flux (Q); or energy loss through radiation  $(P_{\rm rad})$ . It is important to note that the left and right sides of equations (33) and (34) are not exactly equal, as convective heat transport mechanisms are neglected in this simplified treatment.

We use equation (22) in combination with power balance equation as denoted above. We obtain expressions for the electron and ion heat diffusivities:

$$\chi_e = -\frac{625S_e - \frac{d}{dt}(n_e T_e)}{G_{11}n_e \nabla T_e}$$
(35)

$$\chi_i = -\frac{625S_i - \frac{d}{dt}(n_i T_i)}{G_{11} n_i \nabla T_i}$$
(36)

Here,  $G_{11} = \langle (\nabla \rho)^2 \rangle V'$  is a geometric factor that accounts for the flux surface geometry of the tokamak plasma, where V' denotes the derivative of the plasma volume with respect to the radial coordinate. The factor of 625 arises from unit conversion, specifically converting power from MW to keV/s, resulting in the unit of  $m^2/s$  for the diffusivities.

A third diffusivity,  $\chi_{\text{eff}}$ , is also calculated following the definition used in ASTRA:

$$\chi_{\text{eff}} = \frac{Q_e + Q_i}{G_{11}(n_e \nabla T_e + n_i \nabla T_i)},\tag{37}$$

where  $Q_e = 625S_e - \frac{d}{dt}(n_eT_e)$  and  $Q_i = 625S_i - \frac{d}{dt}(n_iT_i)$  represent the total heat fluxes for electrons and ions, respectively and  $n_i$  is the total ion density (main ions plus impurity ions).

For the case of quasi-neutrality  $(Z_{eff} = 1)$  where  $n_e = n_i = n$  and equal temperature gradients  $\nabla T_e = \nabla T_i = \nabla T$ , this expression simplifies to:

$$\chi_{\text{eff}} = \frac{Q_e + Q_i}{2G_{11}n\nabla T} = \frac{\chi_e + \chi_i}{2},\tag{38}$$

effectively becoming the average of the electron and ion heat diffusivities [68]. The previous simplification is for illustrative purposes only. In practice,  $Z_{eff}$  is not assumed to be 1 and electron and ion profiles may differ significantly.

#### 4.2 Subroutines

Throughout the following pages of this thesis the variables  $n_e$ ,  $T_e$ ,  $n_i$  and  $T_i$  will be used without further explanation. This is done to keep the text concise and readable where  $n_e$  is the electron density,  $T_e$  the electron temperature,  $n_i$  the ion density and  $T_i$  the ion temperature. The following subroutines are used to calculate the power deposition profile for a single time point and are called for every time step during the execution of the Timedependent\_transport\_equation.

#### 4.2.1 eval\_equipartition\_model

Computes the electron-ion heat exchange due to Coulomb collisions  $P_{e,i,Cl}$ , which describes the energy transfer from electrons to ions in a plasma. Within a plasma, electrons and ions maintain distinct temperatures and naturally evolve toward thermal equilibrium. During this process, energy flows from the hotter species to the colder one—electrons transferring energy to ions when  $T_e > T_i$ , and ions transferring energy to electrons when  $T_i > T_e$ . This bidirectional energy exchange facilitates thermal equilibration between the two species. It is comonly called the equipartition term and can be expressed as [69]

$$P_{e,i,Cl} = 0.00246 \times ln(\Lambda) \times Suz_{Pei} \times n_e \times \frac{T_e - T_i}{T_e \sqrt{T_e}}$$
(39)

where  $\ln(\Lambda)$  is the local Coulomb logarithm in the plasma [70] and  $Suz_{Pei}$  is a term that characterizes the heat exchange susceptibility of the local plasma, accounting for the effective charge and density contributions of both the main ion species and impurities in that region. It is defined as

$$Suz_{Pei} = \frac{n_{main}}{A_{main}} \times Z_{main}^2 + \sum_{x=1}^{N} \frac{n_{im,x}}{A_{im,x}} \times Z_{im,x}^2$$
 (40)

where  $n_{main}$ ,  $A_{main}$ , and  $Z_{main}$  are the density, atomic number, and charge of the main ion species, respectively. The summation accounts for a number of N main impurities with their respective densities  $n_{im,x}$ , atomic numbers  $A_{im,x}$ , and charge numbers  $Z_{im,x}$ . The term  $Suz_{Pei}$  captures the contributions of both the main ion species and impurities to the electron-ion heat exchange. The implementation of the Coulomb logarithm term  $ln(\Lambda)$  is fully adapted from ASTRA but no proper documentation or source was found for the exact coefficients. It is given as

$$ln(\Lambda) = 15.9 - 0.5 \log(n_e) + \log(T_e). \tag{41}$$

The Coulomb logarithm typically ranges from 10 to 20, depending on the plasma conditions. The logarithmic dependence on electron density and temperature in the implementation reflects the underlying physics: higher densities reduce the Debye length (decreasing  $\ln(\Lambda)$ ), while higher temperatures increase the collision velocities and reduce the classical distance of closest approach (increasing  $\ln(\Lambda)$ ).

As of now only a single impurity is considered, which is assumed to be carbon. The impurity density is calculated from the electron density and the effective ion charge  $Z_{eff}$ .

#### 4.2.2 eval\_POHM\_model

Evaluates Ohmic heating  $P_{Ohm}$  in the plasma, which results from resistive dissipation of the toroidal electric field. The equation is based on the classical Spitzer resistivity formula and is crucial for determining how much energy is supplied to the plasma via electrical currents.

$$P_{Ohm} = \frac{CC}{G_{33}} \times \left(\frac{U_{lon}}{2\pi R_0 \times I_{Pol}}\right)^2 \tag{42}$$

where  $R_0$  is the major radius of the plasma,  $I_{Pol}$  is the normalized poloidal current,  $U_{lon}$  is the longitudinal loop voltage and CC the electrical conductivity. The factor  $G_{33} = \langle (R_0/r)^2 \rangle$  accounts for the geometry of the plasma which was defined in ASTRA. The equation describes how the resistive dissipation of electrical energy contributes to heating the plasma.

#### 4.2.3 eval\_PRAD\_model

The inital implementation which was adapted from ASTRA is based on a model that computes the total radiative power loss  $P_{RAD}$  due to bremsstrahlung, tungsten, and carbon radiation based on the concentration of said impurities.

The bremsstrahlung for a fully ionized plasma is proportional to  $n_e^2 \sqrt{T_e}$  according to [12]. As impurities exist in our plasma which are not fully ionized, the effective ion charge  $Z_{eff}$  and a factor is used to account for the contribution of all ion species in the plasma resulting in [71]

$$P_{RBrems} = 5.06 \times 10^{-5} \times Z_{eff} \times n_e^2 \times \sqrt{T_e}$$
 (43)

for the bremsstrahlung radiation power loss  $P_{RBrems}$ .

The impurity radiation powers are calculated from the impurity concentrations which are multiplied with the density as well as experimentally evaluated temperature dependent radiation functions  $P_{Tun}(T_e)$  and  $P_{Car}(T_e)$  to yield the total radiation power loss.

$$P_{RTun} = n_e^2 \times P_{Tun}(T_e) \times c_{Tun} \tag{44}$$

$$P_{RCar} = n_e^2 \times P_{Car}(T_e) \times c_{Car} \tag{45}$$

where  $c_{Tun}$  and  $c_{Car}$  are the concentrations of tungsten and carbon, respectively. The carbon concentration is calculated from the effective ion charge  $Z_{eff}$  and the main ion charge  $Z_{main}$ 

$$c_{Car} = \frac{Z_{eff} - Z_{main}}{Z_{Car}(Z_{Car} - Z_{main})} \tag{46}$$

where  $Z_{Car}$  is the charge of the carbon ion, which is 6. The tungsten concentration  $c_{Tun}$  is fetched from the GIW shotfile which derives two very coarse and often unavailable values for the  $c_{Tun}$  over the radial axis. The concentrations are derived from a quasicontinuum model and spectrometer measurements which is described in [72].

During the validation phase of the project the radiation function  $P_{Tun}(T_e)$  was updated to the latest known values [73] which can be seen in Figure 13.

The total radiative power loss is then given by the sum of the bremsstrahlung and impurity radiation contributions

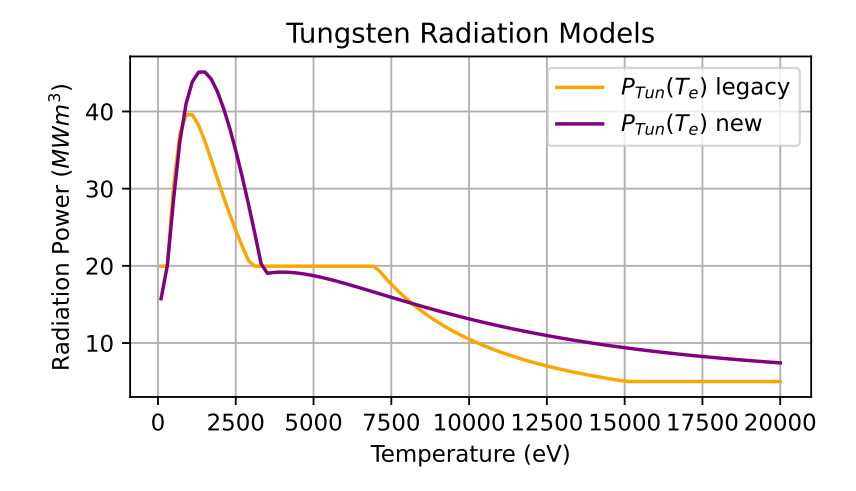


**Figure 13:** Radiation functions for tungsten as a function of electron temperature  $T_e$ . The function is used to calculate the radiative power loss in the plasma. The values are based on experimental data and theoretical models [73].

$$P_{RAD} = P_{RBrems} + P_{RTun} + P_{RCar}. (47)$$

During the validation phase, it was determined that the modeled radiation profile lacked sufficient accuracy, primarily due to limited knowledge of the tungsten concentration. As a result, the subroutine was replaced with an approach that relies on direct measurements rather than calculating the radiation from impurity concentrations. The theoretical foundation of this alternative method is explained in section 2.8, the implementation details are presented in section 4.3 and the initial problems of the legacy model as well as the results from the new method are discussed in section 5.2.

### 4.3 Implementation of GPT into the IDE framework

During the process of porting the Python GPT code to Fortran90, a fundamental issue within the profile generation procedure was discovered. According to equation (29), the integration process sums over all pixels satisfying  $\rho_{pol} \leq 1$ . This requires first calculating the normalized magnetic coordinate  $\rho_{pol}$  for each pixel from its known (r, z) coordinates. This coordinate transformation is performed using an equilibrium reconstruction (such as IDE), which provides the magnetic flux at each spatial location.

Figure 14 illustrates this challenge using two representative discharge configurations. The left panel shows an example discharge in Lower Single Null (LSN) configuration, where the intersection of the separatrix (blue line)—also known as the X-point—is located at the bottom of the plasma. The right panel depicts a discharge in Upper Single Null (USN) configuration with the X-point positioned at the top of the plasma.

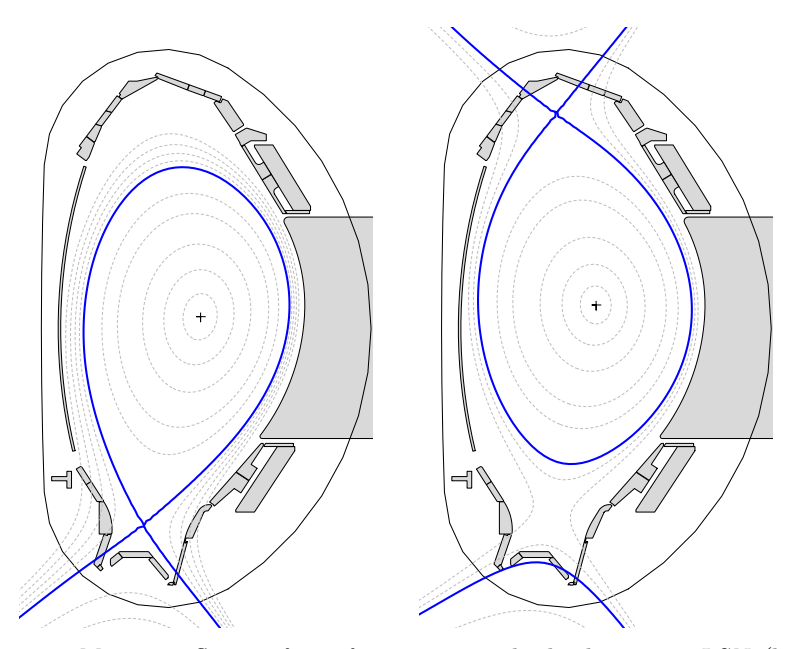


Figure 14: Magnetic flux surfaces for two example discharges in LSN (left) and USN (right) configurations. The blue line indicates the separatrix, with its self-intersection point being the X-point. Gray dashed lines represent additional magnetic flux surfaces for different values of  $\rho_{pol}$ .

The magnetic flux can be conceptualized as a topographical map where the normalized radial coordinate  $\rho_{pol} < 1$  within the separatrix (blue line) and  $\rho_{pol} > 1$  outside it. However, a critical issue becomes apparent when examining the magnetic field topology: regions that lie topologically within the separatrix but are positioned beyond the X-point also yield  $\rho_{pol}$  values less than 1. This phenomenon is most clearly observed by following the gray dashed flux lines that extend beyond the X-point region.

This geometric complexity poses a significant challenge for accurate radial integration, as pixels located in the divertor region (below the X-point in LSN configuration or above in USN configuration) may incorrectly contribute to the core plasma emission profile, leading to systematic errors in the reconstructed radiation profiles. This issue manifested in the original Python implementation of GPT, where the radial integration applied bin masks of  $\Delta \rho_{pol} = 0.1$  width that inadvertently included emission from divertor regions lying topologically outside the confined plasma volume, despite having  $\rho_{pol} < 1$  values. Figure 15 illustrates this problematic inclusion of pixels below the X-point due to the flawed masking procedure.

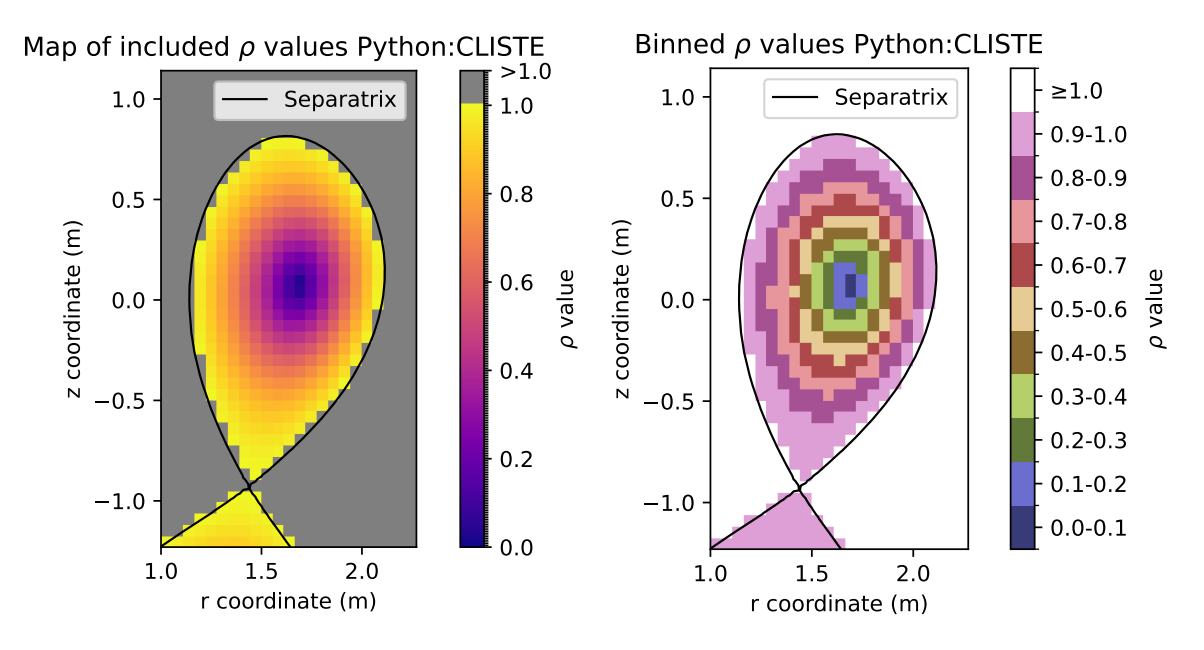


Figure 15: Erroneous pixel inclusion in radial integration for discharge #33173 at t=1.0s using the Python GPT implementation with CLISTE equilibrium data. Left panel: Gradient colormap showing all pixels with  $\rho_{pol} < 1$  included in the integration. Right panel: Binned colormap depicting the radial bins of  $\Delta \rho_{pol} = 0.1$  used for integration. The separatrix (black line) emphasizes how pixels in the divertor region (below the X-point) are incorrectly included in the confined plasma radiation profile reconstruction.

To address this issue, a simple yet effective solution was implemented in the Fortran version: the algorithm now retrieves the z-coordinate of the X-point and applies an additional spatial constraint. For LSN configurations, only pixels satisfying both  $\rho_{pol} < 1$  and  $z > z_{\text{X-point}}$  are included, while for USN configurations, the constraint becomes  $\rho_{pol} < 1$  and  $z < z_{\text{X-point}}$ . This geometric filtering ensures that only pixels within the topologically confined plasma volume contribute to the radial integration, effectively eliminating the systematic errors introduced by the previous approach.

Since the transport coefficient calculation in IDE is performed using the toroidal magnetic coordinate  $\rho_{tor}$ , it is advantageous to conduct the radial integration directly in  $\rho_{tor}$  coordinates rather than  $\rho_{pol}$ . However,  $\rho_{tor}$  becomes ambiguous outside the separatrix, where values between 0 and 1 can occur in regions that are topologically outside the confined plasma. Therefore, we cannot simply substitute one coordinate for

the other without additional constraints.

The integration procedure requires a two-step filtering process. First, we use  $\rho_{pol}$  to identify all pixels located within the separatrix. Second, we apply X-point filtering by examining each remaining pixel's z-coordinate against the spatial constraints described previously. To ensure robust filtering across different plasma configurations that may contain multiple X-points within the computational domain, we exclude regions between both X-points, implementing the conditions:

$$0 < \rho_{pol} < 1 \begin{cases} z_{xp1} < z_{\text{pixel}} < z_{xp2} & \text{for LSN configuration if } z_{xp1} < z_{xp2} \\ z_{xp2} < z_{\text{pixel}} < z_{xp1} & \text{for USN configuration if } z_{xp1} > z_{xp2} \end{cases}$$

$$(48)$$

Only pixels satisfying both the  $\rho_{pol} < 1$  criterion and the appropriate z-coordinate constraints are included in the subsequent radial integration using  $\Delta \rho_{tor} = 0.1$  bins.

The integration produces a radiative power loss profile  $P_{\rm rad}$  in units of MW, resolved into 10 radial bins. For transport coefficient calculations, however, a finer radial resolution of 200 elements across  $\rho_{tor}=0$  to  $\rho_{tor}=1$  is required. To achieve this, cubic spline interpolation is applied to both the power and volume profiles, yielding high-resolution splines for each radial position along  $\rho_{tor}$ . The radiative power is then converted to a volumetric profile  $(MW/m^3)$  by dividing the interpolated power by the corresponding volume of each segment, as defined by the ASTRA convention  $V=d\rho \cdot V'$ . This approach ensures that the total integrated power remains consistent after rescaling. The resulting profiles are illustrated in Figure 16.

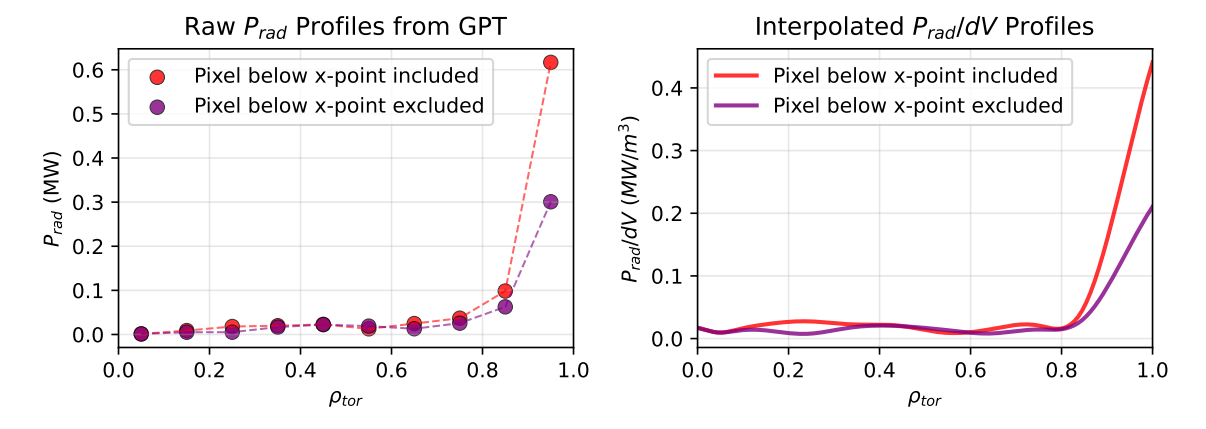


Figure 16: Comparison of the radiative power for discharge #33173 at 1.0s. Left panel: Radiative power profiles calculated by the GPT method, comparing calculations with (purple) and without (orange) the z-coordinate X-point filtering condition. Right panel: Interpolated power profile normalized by the interpolated volume of each radial segment.

The left panel of Figure 16 clearly demonstrates that the profile excluding pixels below the X-point (purple) yields significantly lower radiation towards the plasma edge compared to the profile that erroneously includes those divertor pixels (orange). This validates the importance of proper geometric filtering in the radial integration procedure.

When comparing the profiles generated by the original Python method with the

newly ported Fortran 90 version, slight differences become apparent, as shown in Figure 17.

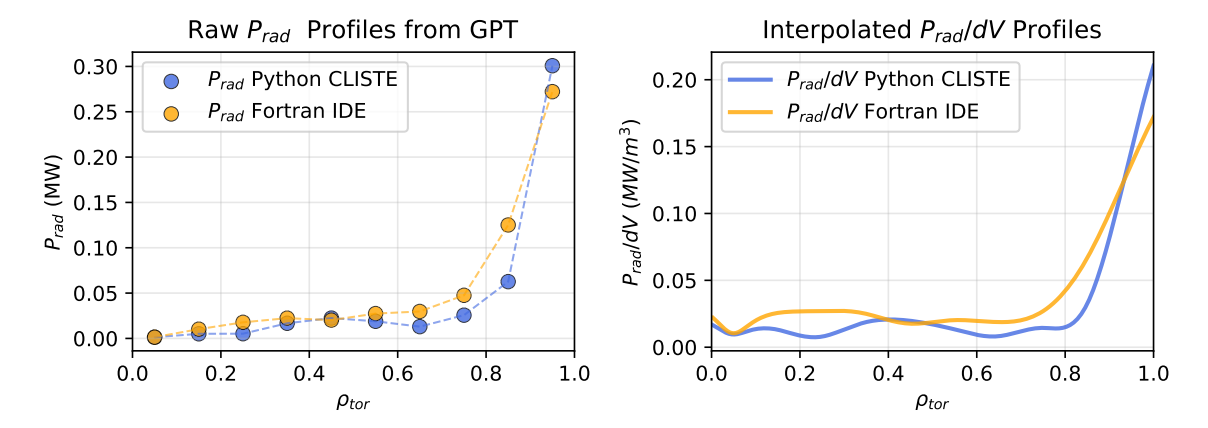


Figure 17: Comparison of the radiative profiles from Python via CLISTE and Fortran90 via IDE equilibrium for discharge #33173 at 1.0s. Left panel: Radiative power profiles calculated by the GPT method. Right panel: Interpolated power profile normalized by the interpolated volume of each radial segment.

These differences are primarily attributed to the distinct magnetic equilibria employed by each code, which becomes more evident when examining the exact pixel binning used by each method, as illustrated in Figure 18. The CLISTE and IDE equilibria produce different magnetic flux surface values, resulting in pixels being assigned to different radial segments during the integration process.

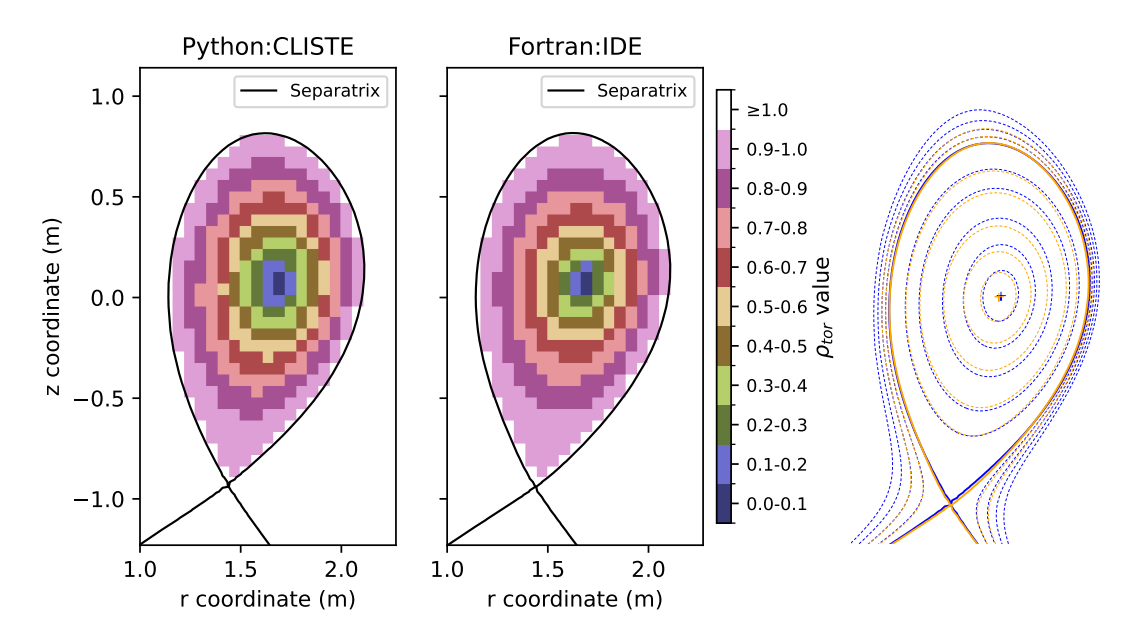
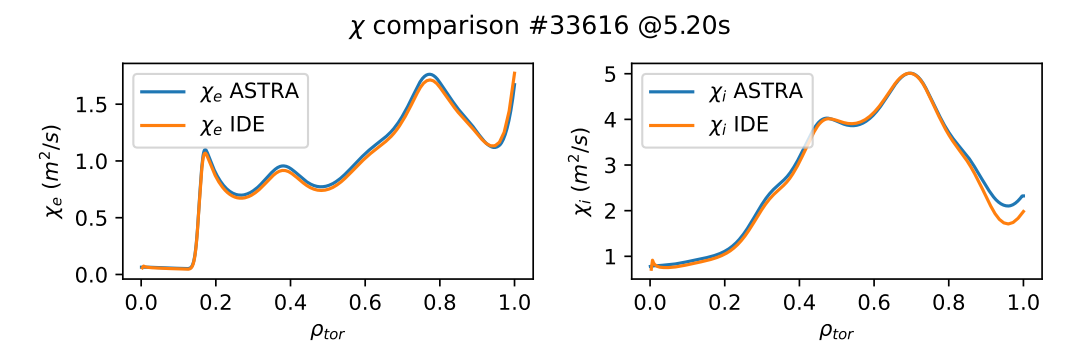


Figure 18: Impact of different magnetic equilibria on pixel binning for discharge #33173 at 1.0s. Left and middle panels: Pixel binning for radial integration with  $\Delta \rho_{tor} = 0.1$  intervals using CLISTE and IDE equilibria, respectively. Right panel: Comparison of flux surfaces from CLISTE (blue) and IDE (orange) equilibria.

The emission reconstruction itself, which represents the primary output of the GPT method, remains unaffected by the choice of equilibrium reconstruction since it relies exclusively on bolometer measurements. Consequently, the Fortran implementation can be readily validated by direct comparison with the original Python implementation. A detailed comparison of the reconstructed 2D emission pixel maps is presented in the Appendix in Figure A1.

## 5 Analysis of the transport coefficients calculation

After the inital implementation of the transport coefficients calculation, a validation was performed to ensure the correctness of the implementation and to identify potential issues. The validation was done by comparing the results with the ASTRA code, which is a well-established code for plasma transport calculations. Running IDE in steady state (no time dependencies of the ne, Te, etc,-profiles) as it is done in ASTRA aswell as taking the same input profiles as ASTRA we expect the results to be the same and they were checked for consistency. This proved to be essential as it led to the discovery of several issues like incorrect data fetching and indexing errors in the initial implementation, which were subsequently fixed. The results of the validation with the same input data can be seen in Figure 19.



**Figure 19:** Comparison of the electron and ion heat diffusivity  $\chi_e$  and  $\chi_i$  calculated by the IDE and ASTRA codes for the same input data. The small discrepancies which can still be seen are due to some parameters being not taken over.

In Figure 20 we can see the results of the validation when running IDE with the input profiles from IDA, which are not in steady state and therefore include the  $\frac{dw}{dt}$  term. The results differ from those obtained with ASTRA as expected but overall show similar trends.

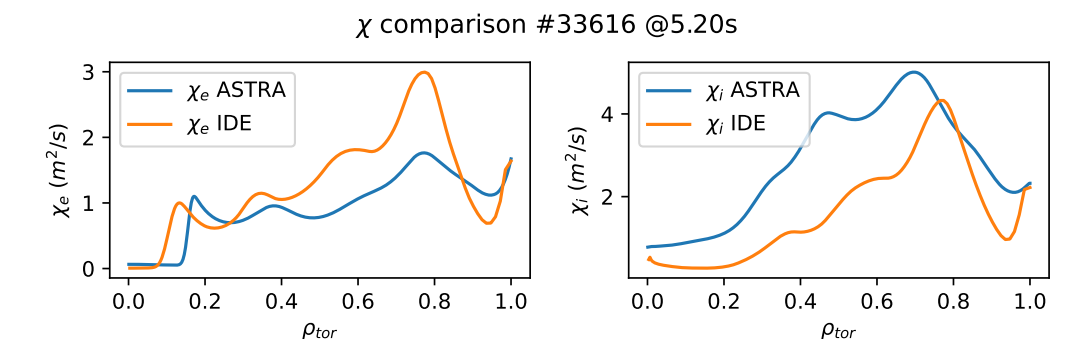


Figure 20: Comparison of the electron and ion heat diffusivity  $\chi_e$  and  $\chi_i$  calculated by the IDE and ASTRA codes for their respective input data. While the overall trends are similar, several notable discrepancies are evident.

Although the absolute values, especially for  $\chi_i$ , differ considerably, the profiles ex-

hibit similar trends and even feature small "bumps" at nearly identical radial positions. These differences prompted a more detailed investigation into the power balance calculations, focusing on the specific terms used in IDE and ASTRA. The findings from this analysis are presented in the following sections.

### 5.1 Power depositions

Comparing the power deposition profiles of IDE and ASTRA revealed significant inconsistencies between the two codes. The electron power deposition profile  $S_e$  shown in Figure 21 clearly demonstrates these differences.

Figure 21 presents the electron power deposition profile  $S_e$  calculated by both IDE and ASTRA codes for discharge #33173 at 3.7s. The solid lines represent IDE calculations, while the dashed lines correspond to ASTRA results. Although the profiles show reasonable agreement in most plasma regions, a notable discrepancy emerges in the core region around  $\rho_{tor} = 0.2$ . Here, the purple lines representing the ECRH power deposition calculated through a code called TORBEAM [74] exhibit a significant radial shift between the two codes.

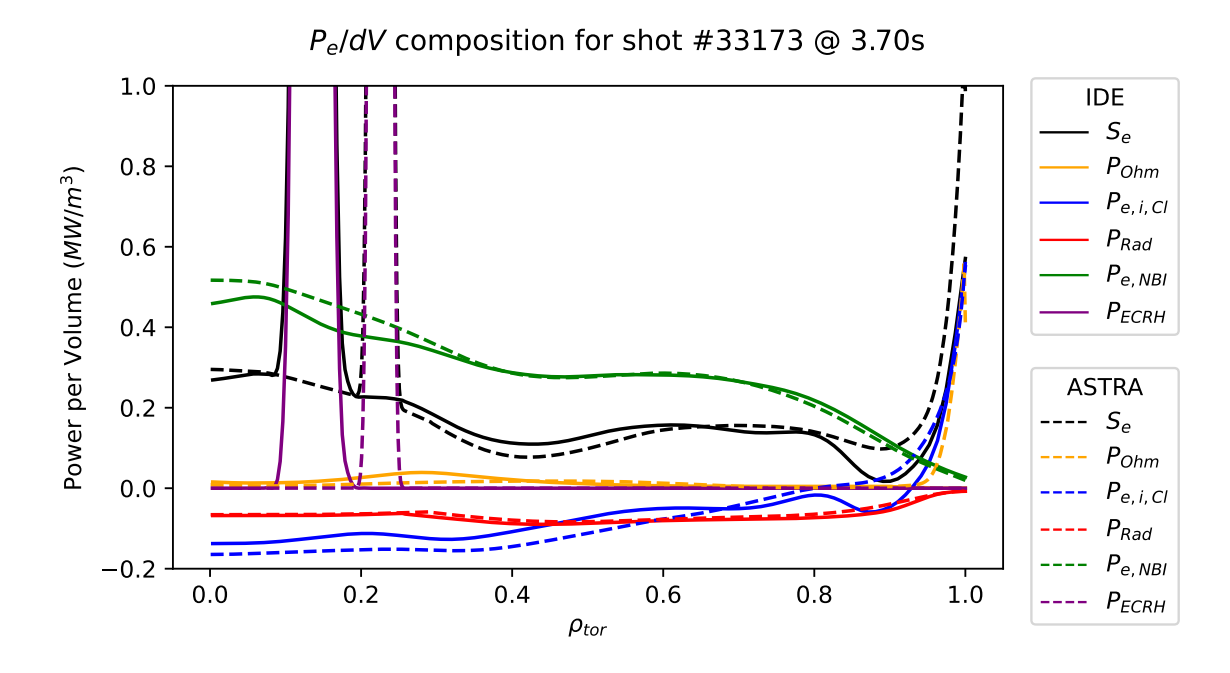


Figure 21: Comparison of the electron power deposition profile  $S_e$  calculated by the IDE and ASTRA codes for discharge #33173 at 3.7s. The profiles show significant differences, especially in the core and edge regions.

This shift can be attributed to differences in the underlying magnetic equilibrium reconstructions. ECRH heating depends critically on electron cyclotron resonance conditions, which are determined by the local magnetic field strength. Since ASTRA employs the SPIDER equilibrium code [75] while IDE uses its own internal equilibrium reconstruction, variations in the calculated magnetic field profiles lead to different resonance locations and consequently different power deposition patterns. This equilibrium-dependent sensitivity highlights the importance of accurate magnetic field

reconstruction for precise heating calculations as well as the difficulty of comparing transport coeffcient results from different codes that use different equilibrium models.

#### 5.2 Radiative Power Loss

Another significant uncertainty in the power deposition profile is the radiated power  $P_{RAD}$ , which has previously relied on the radiation model from ASTRA. This model calculates radiation based on impurity concentrations and their respective radiation properties, combined with bremsstrahlung contributions. The primary impurities considered are carbon and tungsten, which enter the plasma through erosion of plasma-facing components and divertor materials. The radiation model employs empirical formulas derived from experimental data to determine impurity radiation rates as functions of temperature and density (see Figure 13).

Accurate implementation of this approach requires precise knowledge of impurity concentrations throughout the plasma. These concentrations are typically determined through spectroscopic measurements of emission lines characteristic of specific elements. However, this poses significant challenges for heavy elements like tungsten, which exhibit numerous ionization states and correspondingly complex emission line spectra. In the present analysis, only two radially distributed tungsten concentration values were available from the GIW shotfile [72]. According to equation (44), the tungsten radiative power  $P_{RTun}$  is directly proportional to the tungsten concentration  $c_{Tun}$ , meaning that uncertainties in concentration measurements directly translate to errors in the calculated radiation profile.

Furthermore, the model's dependencies on temperature profiles and quadratic dependence on electron density  $n_e$  cause the calculated radiative power to approach zero toward the plasma edge, where these profiles naturally decrease. This behavior contrasts with experimental observations, as illustrated in Figure 22, which compares the calculated radiation profile based on impurity concentrations (blue) with the GPT profile (orange) and a manually reconstructed tomography profile (red).

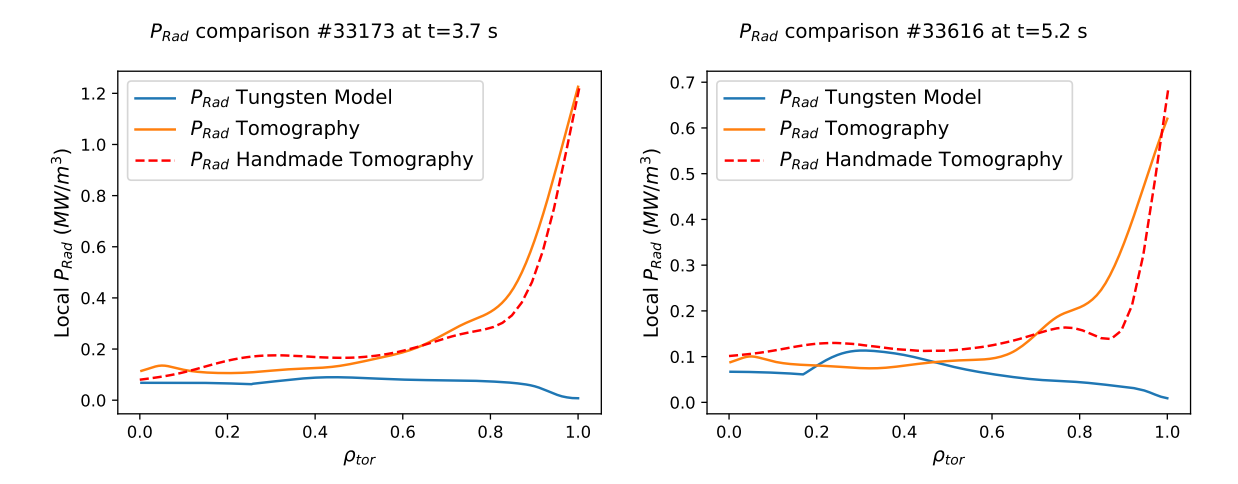


Figure 22: Comparison of the calculate radiation profile (blue), the Gaussian Process Tomography (orange) and the handmade tomography profile (red) for shot #33173 at 3.7s and #33616 at 5.2s.

The manual tomography profile, based on expert analysis of bolometer data, rep-

resents the most reliable reconstruction available. The impurity concentrations based profile exhibits an unphysical drop toward the plasma edge, which is absent in both tomographic reconstructions. The GPT profile demonstrates more realistic behavior, maintaining finite radiation levels at the plasma edge and showing good agreement with the manual reconstruction, albeit with some deviations in the core region.

To address these limitations, an alternative approach was implemented that bypasses impurity concentration calculations entirely. Instead of relying on theoretical models, this method directly infers the radiation emission profile from bolometer measurements using tomographic reconstruction techniques. While traditional tomography usually requires extensive manual intervention, an automated approach called GPT was developed in [44, 45] (see sections 2.8 and 4.3). This method employs Gaussian process regression to automatically reconstruct radiation profiles from bolometer measurements at each time step, providing more reliable and physically consistent results.

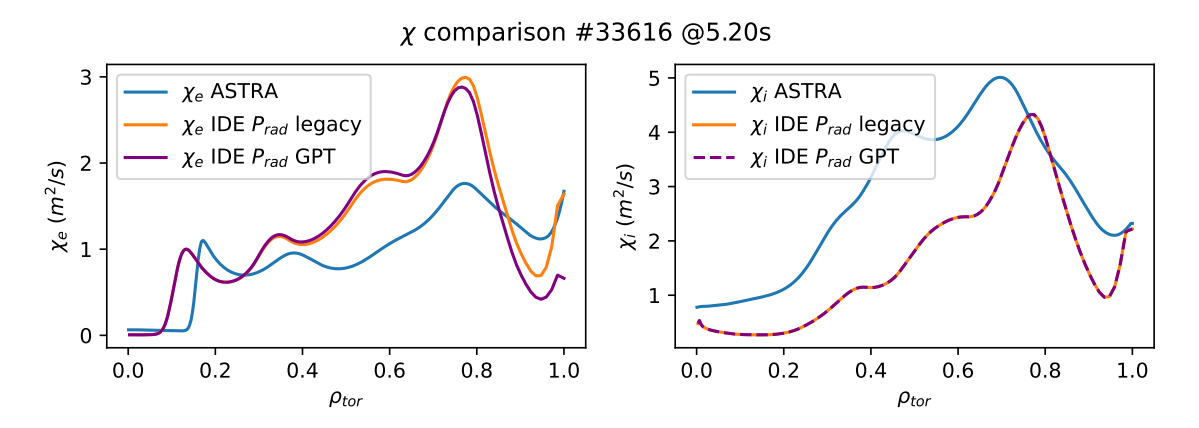


Figure 23: Comparison of the impact of the GPT radiation profile on the transport coefficients  $chi_e$  and  $chi_i$  for discharge #33616 at 5.2s.

The effect of using the substituted radiation profile is illustrated in Figure 23, which compares the transport coefficients calculated with the GPT radiation profile (purple) to those obtained using the original impurity-based profiles from IDE (orange) and ASTRA (blue). Notably, there is a pronounced difference in the transport coefficients near the plasma edge, which is expected since the GPT profile rises rapidly at the edge rather than dropping to zero. For the ion heat diffusivity  $\chi_i$ , no difference is observed, as the radiative term does not contribute to its calculation according to the power balance equations defined in Section 4.1.

### 5.3 Sensitivity Study

To assess the sensitivity of the transport coefficient calculations to errors and uncertainties in the input profiles and measurements, we first identified the most influential parameters in the underlying equations. For each of these parameters, we defined realistic uncertainty ranges based on expected measurement [66, 76, 77]. Using a Monte Carlo simulation approach [78], we then generated a spectrum of possible solutions by randomly sampling within these uncertainty intervals, allowing us to quantify the impact of input uncertainties on the final results.

It is important to emphasize that, although the absolute values of temperature and density for both electrons and ions are generally determined with reasonable accuracy, their radial gradients—essential for transport coefficient calculations—are much more susceptible to measurement noise and uncertainties arising from profile stitching. In this analysis, uncertainties in these gradients are not explicitly quantified; instead, their effects are assumed to be partially captured by the overall uncertainty ranges assigned to the profiles from which the gradients are derived. Previous experience indicates that uncertainties in the gradients can contribute substantially to the total error, particularly in regions with steep profile changes or where different diagnostics overlap and smoothing constraints are being applied leading to gradients close to zero.

**Table 1:** Sensitivity study parameters: Expected uncertainties in plasma parameters.

Parameter	Uncertainty Range
$n_e$	±20%
$T_e$	±20%
$\overline{T_i}$	±20%
$P_{\rm rad}$	±40%
$Z_{ m eff}$	±20%
$P_{ m NBI}$	±10%
$P_{\text{ECRH}}$	±10%
$\rho_{tor}$	$\pm 2\% \stackrel{.}{=} \pm 1 \text{cm}$

The parameters summarized in Table 1 indicate the typical measurement uncertainties for the main plasma quantities involved in the transport coefficient calculations. Electron density  $n_e$ , electron temperature  $T_e$ , and ion temperature  $T_i$  each have estimated uncertainties of  $\pm 20\%$ , reflecting the limitations of current diagnostic techniques. The radiative power loss  $P_{\rm rad}$  and effective ion charge  $Z_{\rm eff}$  are also subject to uncertainties of  $\pm 40\%$  and  $\pm 20\%$  respectively, primarily due to the challenges in impurity characterization. Heating powers  $P_{\rm NBI}$  and  $P_{\rm ECRH}$  are more precisely controlled, with uncertainties of about  $\pm 10\%$ . The radial coordinate  $\rho_{tor}$  is assigned an uncertainty of  $\pm 2\%$ , corresponding to approximately  $\pm 1\,{\rm cm}$  of radial displacement.

### Input Error Propagation

Figure 24 illustrates how these uncertainties (excluding  $\rho_{tor}$ ) affect the input profiles. The profiles are shown for discharge #33173 at 3.7s, with the control profile (black) compared to variations induced by each parameter. Four equally spaced values within the uncertainty range were used as multiplication factors for the entire profile.

It is important to note that  $\chi_e$  and  $\chi_i$  are not influenced by the same set of variables; for instance, ECRH heating affects only  $\chi_e$ ,  $P_{i,NBI}$  only  $\chi_i$ . Therefore, in the following analysis, only the relevant variables for each transport coefficient are considered.

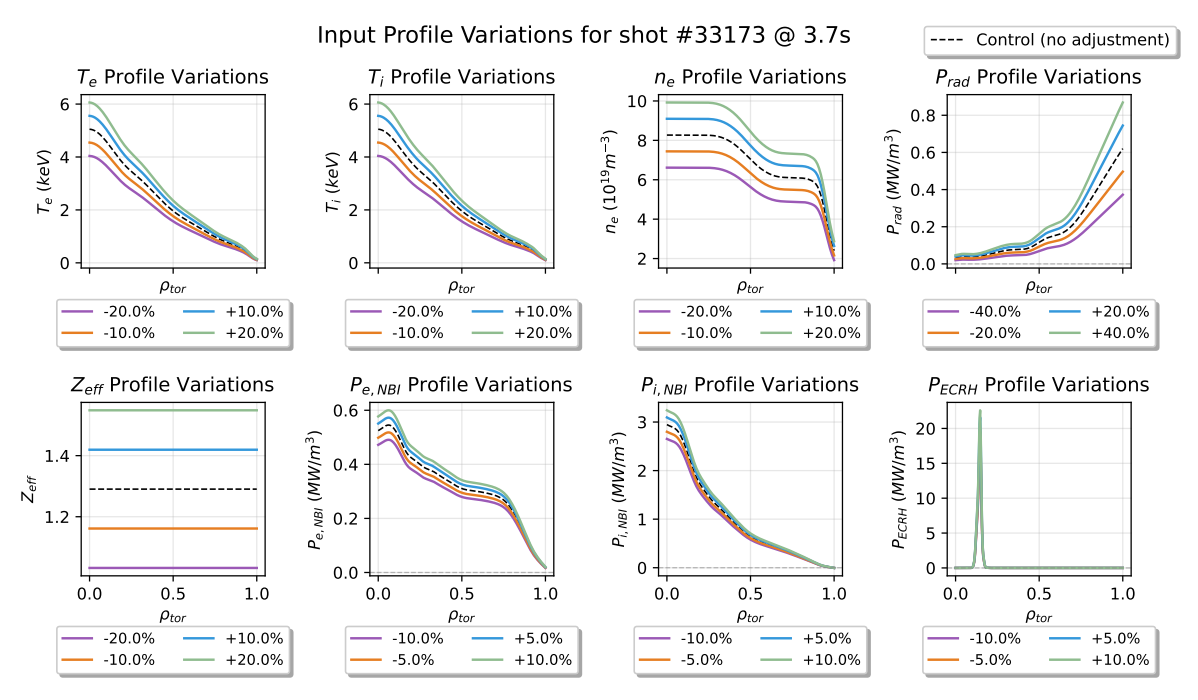


**Figure 24:** Impact of parameter uncertainties on input profiles for discharge #33173 at 3.7s.

The influence of these parameter uncertainties on the diffusive transport coefficients  $\chi_e$  and  $\chi_i$  is illustrated in Figure 25. The figure highlights how each variable affects the profile at different radial positions. A decrease in electron density  $n_e$  or electron temperature  $T_e$  typically causes an overall increase in the magnitude of the  $\chi_e$  profile. Conversely, increasing the ion temperature  $T_i$  leads to a reduction in  $\chi_e$ , which is primarily due to the behavior of the  $P_{e,i,Cl}$  term. The effect of the improved radiative power term  $P_{\rm rad}$  is particularly evident near the plasma edge ( $\rho_{tor} \approx 0.9$  to 1.0), where variations in radiation magnitude result in significant changes to the  $\chi_e$  profile.

The lower 5 Panels of Figure 25 show the corresponding impact on  $\chi_i$ . Here, the influence of  $n_e$ ,  $T_e$ , and  $T_i$  is similar, but the roles of the temperature profiles are reversed, reflecting the different dependencies in the ion heat exchange equation.

In both cases, the temperature profile of the respective particle species is the dominant factor, as it determines the gradient in the power balance equations.

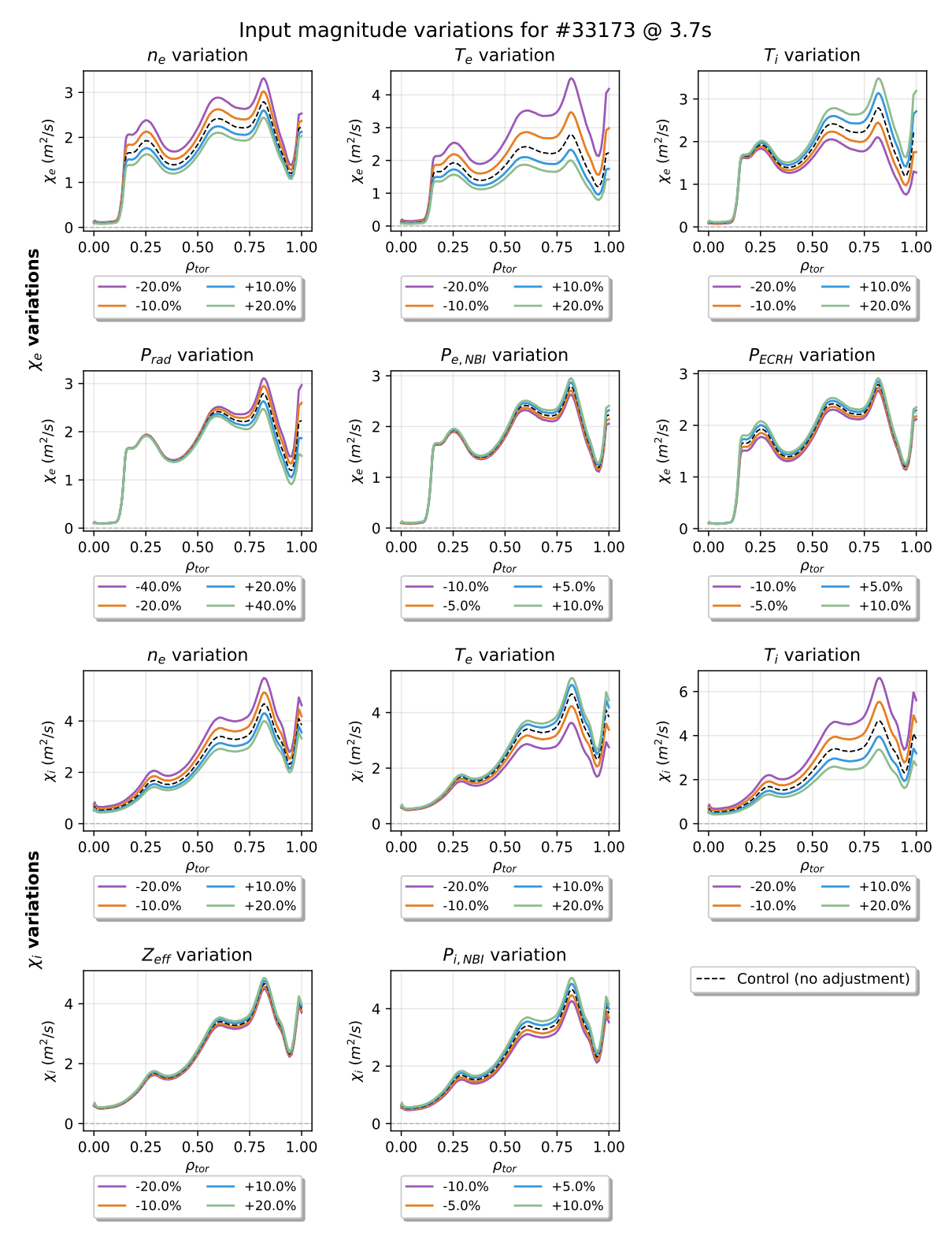


**Figure 25:** Impact of the different parameter variations on the heat diffusivities profiles of  $\chi_e$  and  $\chi_i$  for discharge # 33173 at 3.7s.

To better visualize the relative effect of each variable, we calculate normalized difference

$$\Delta \chi_{norm} = \frac{\chi_{var} - \chi_{control}}{|\chi_{control}|}.$$
 (49)

This approach enables a direct comparison of the relative influence of each parameter and its uncertainty range on the transport coefficient profiles, as illustrated in Figure 26.

Figure 26 clearly shows that electron temperature  $T_e$  has the largest impact on the  $\chi_e$  profile, with variations reaching up to 75% depending on the radial position. The effect of  $P_{\rm rad}$  becomes increasingly significant towards the plasma edge, consistent with previous observations. The influence of  $P_{e,\rm NBI}$  is notable in the core region but diminishes rapidly beyond the main heating region, where  $P_{\rm ECRH}$  has the smallest effect.

The normalized difference profiles for  $\chi_i$ , which are displayed in the lower five panels of Figure 26, exhibit a similar pattern, with ion temperature  $T_i$  being the most influential parameter, as expected. Interestingly, the impact of most of  $\chi_i$  dependant parameters decreases towards the plasma edge, except for the temperature profiles  $T_e$  and  $T_i$ , whose impact increases throughout the radial position.

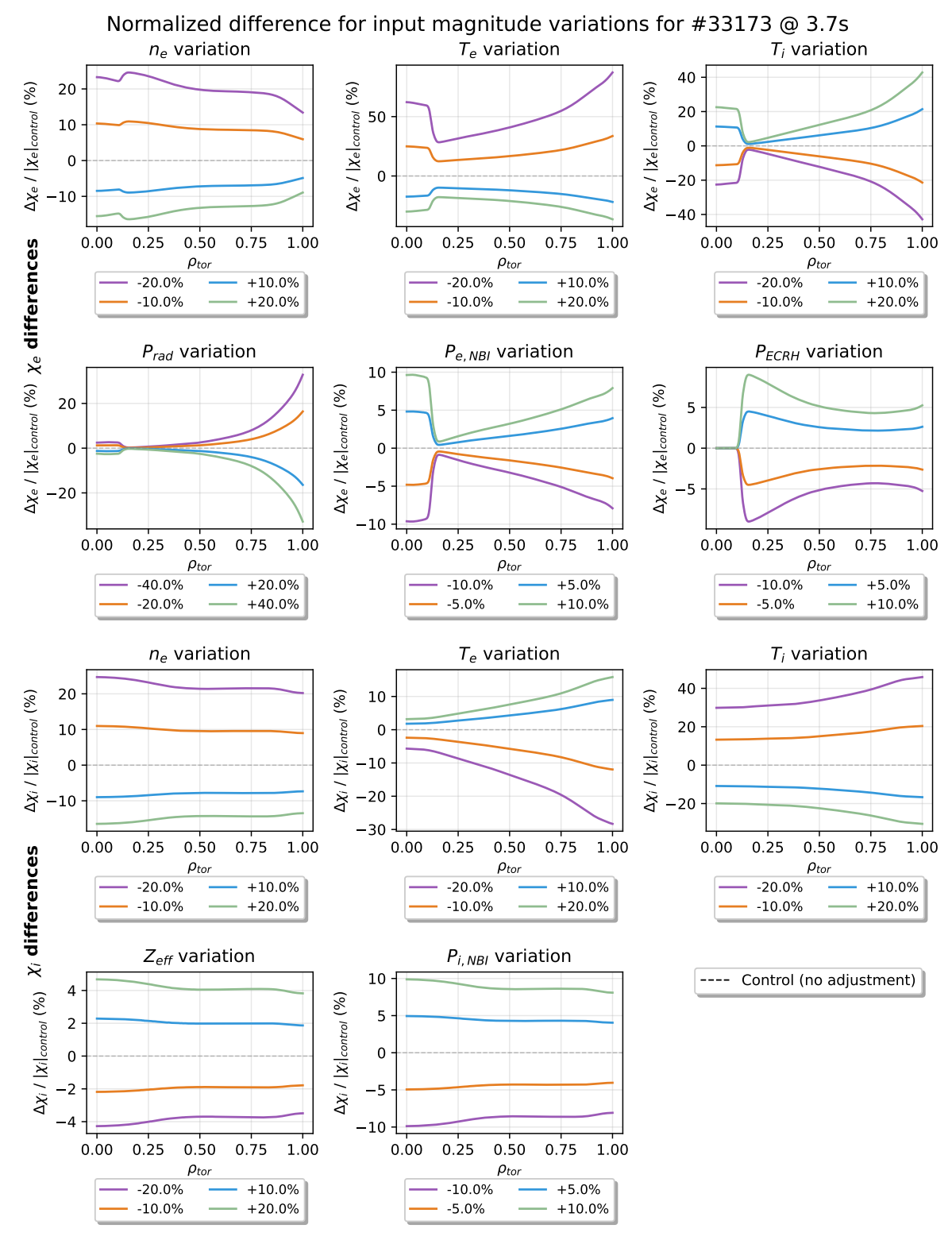


**Figure 26:** Normalized difference profiles showing the impact of parameter uncertainties on the heat diffusivity  $\chi_e$  and  $\chi_i$  for discharge #33173 at 3.7s.

### Varying Radial Alignment

We applied a similar method to assess uncertainties in the radial alignment of our profiles, defined as  $\Delta \rho_{tor} = \pm 2\%$ . This is particularly important for temperature profiles, since their gradients strongly influence the transport coefficient calculation. Figure 27 illustrates the effect of shifting each profile radially by the uncertainty in  $\rho_{tor}$  for each variable. Although the overall shift is small and differences are subtle, they become noticeable in regions where the profile is steep.

To implement the shift, the number of radial points in each profile is multiplied by the specified percentage. With a current radial resolution of 200 elements, a 2% shift corresponds to 4 elements. Profiles are shifted accordingly, and any points falling outside the original range are generated using a natural cubic spline interpolation, ensuring smooth extension beyond the known values.

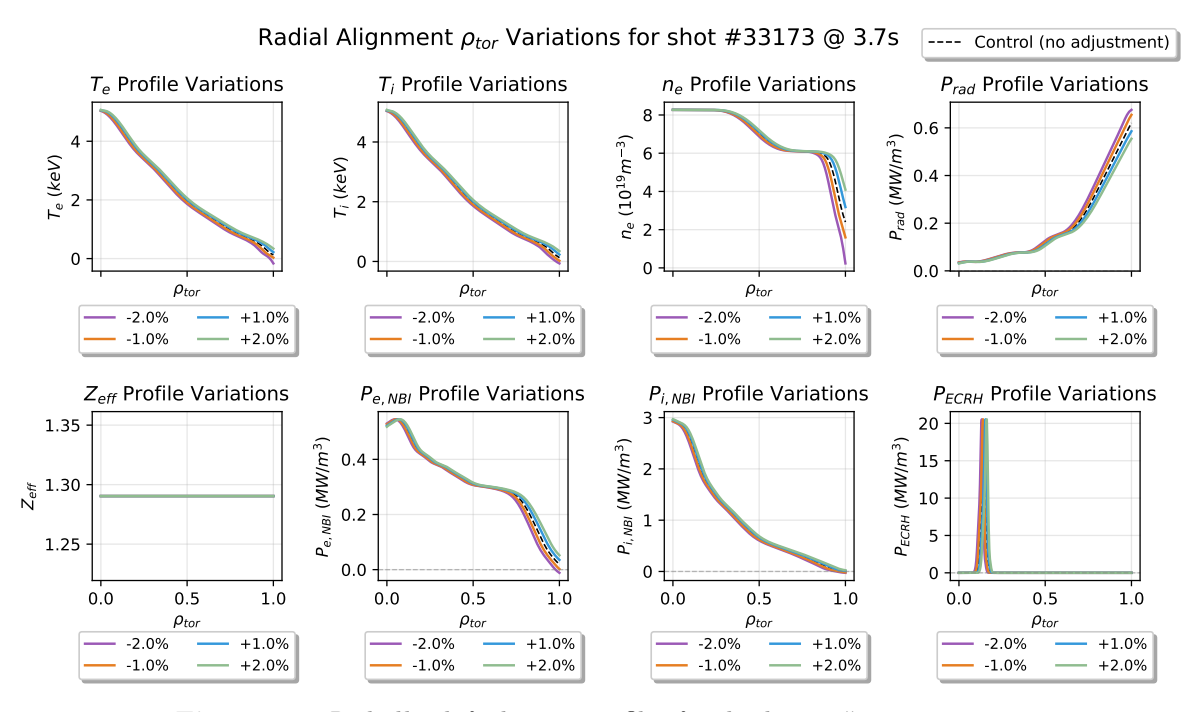
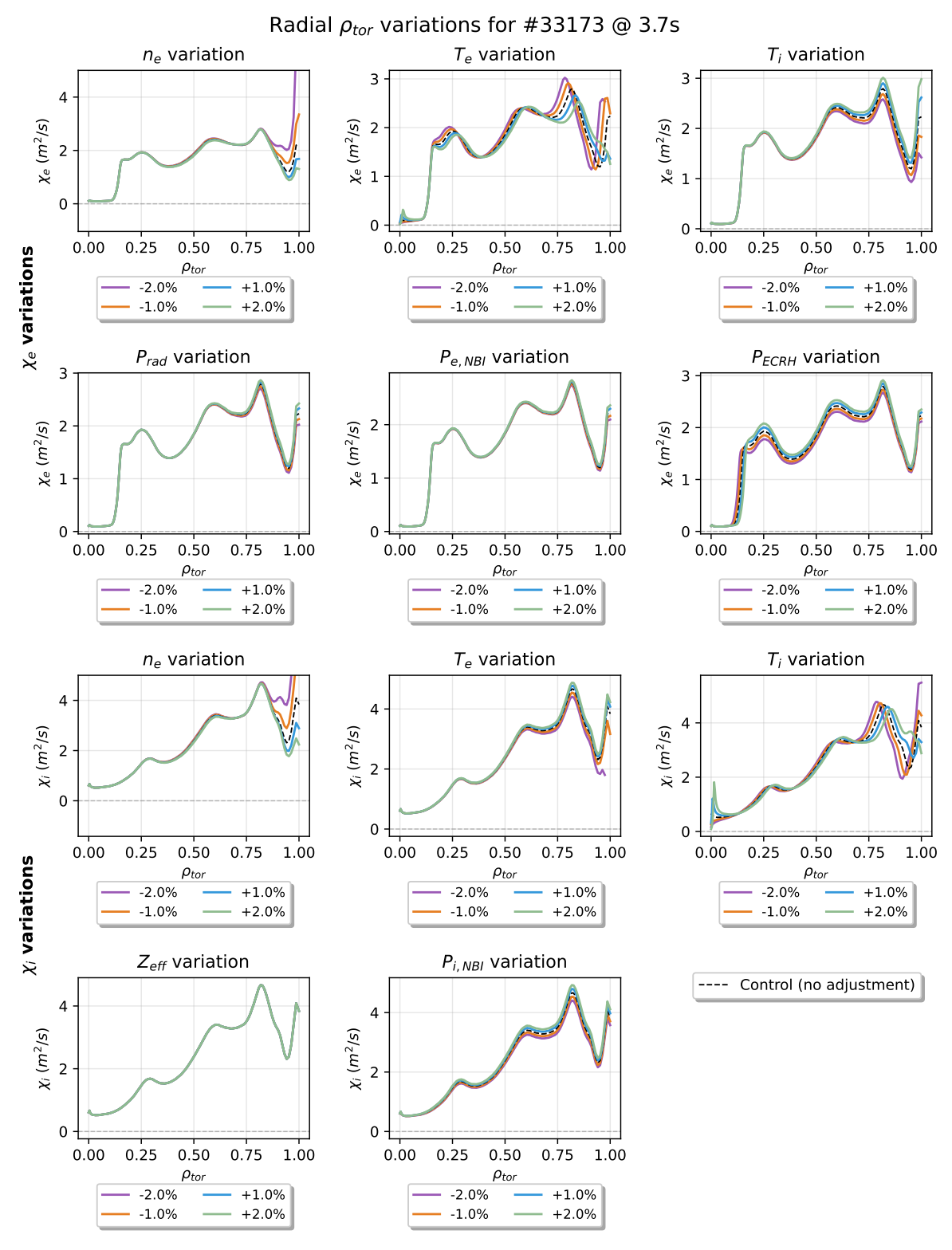


Figure 27: Radially shifted input profiles for discharge #33173 at 3.7s.

The first panel in Figure 28 highlights an issue arising from the generation of values outside the original profile interval. In our case, the density drops sharply within the confined plasma region, causing  $\chi_e$  to spike to very high values. Similar but lees pronounced effects can be seen  $T_e$ ,  $T_i$  in the second and third Panel. It is particularly important to pay close attention to the alignment of these profiles in the pedestal region, as that can lead to large effects on the calculated transport coefficients. Small misalignments or shifts between these profiles may result in significant deviations, especially in regions where the gradients are strongest. For location-dependent profiles such as  $P_{ECRH}$ , a clear shift in the resulting  $\chi_e$  profile is observed. The temperature profiles show an even stronger sensitivity, likely due to changes in the temperature gradient, which significantly affects the denominator in equation (22).



**Figure 28:** Effect of shifts of different parameters along the radial axis ( $\rho_{tor}$ ) on the  $\chi_e$  and  $\chi_i$  profiles for discharge #33173 at 3.7 s.

### Generalised Uncertainty Estimation

To estimate the overall uncertainty in cases where the exact parameter values are unknown, we generated a pseudo-random set of 1000 samples, each representing a possible variation of all relevant parameters for a single discharge. For each parameter in every sample, a random value was drawn within the uncertainty ranges specified in Table 1. The distribution of these sampled values is shown in the appendix (Figure A2). Figure 29 illustrates the resulting parameter profiles, highlighting the 50th and 90th percentile envelopes for both magnitude and radial shifts—effectively varying 16 parameters simultaneously.

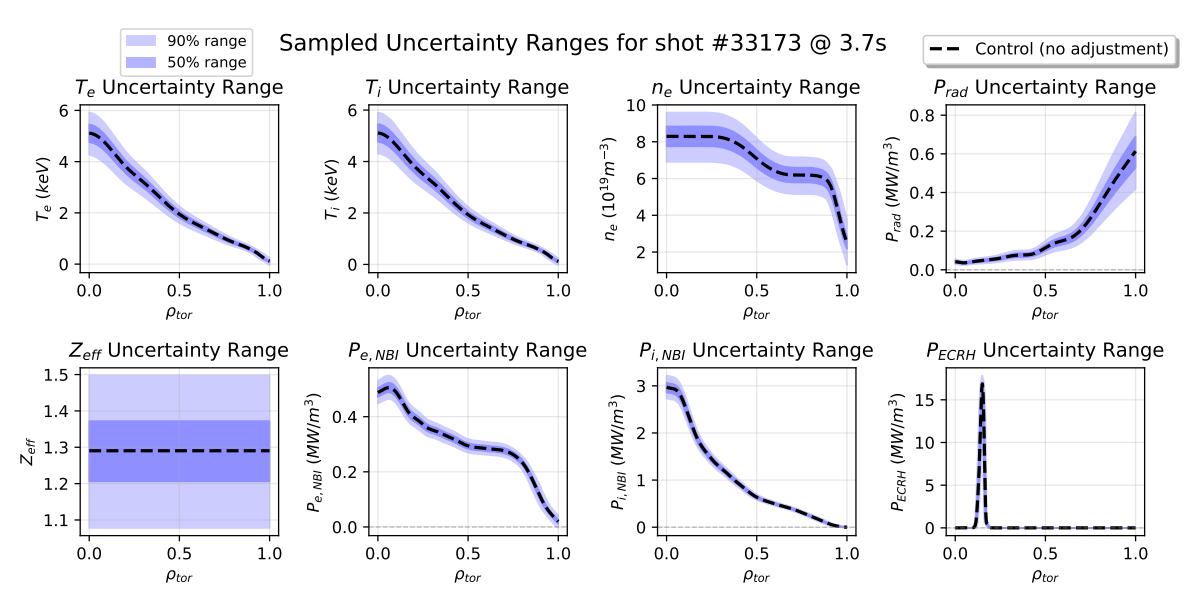


**Figure 29:** Parameter profile envelopes (50th and 90th percentiles) resulting from the sampled uncertainty ranges.

For each sample, the transport coefficient calculation was performed and the results stored. The right panels of Figure 30 display all resulting  $\chi_e$  and  $\chi_i$  profiles from the uncertainty sampling. To better visualize the spread, percentile envelopes were constructed, as shown in the left panels of Figure 30. Notably, the uncertainty bands (50% and 90%) widen significantly towards the plasma edge ( $\rho_{tor} = 1$ ), indicating increased sensitivity in that region.

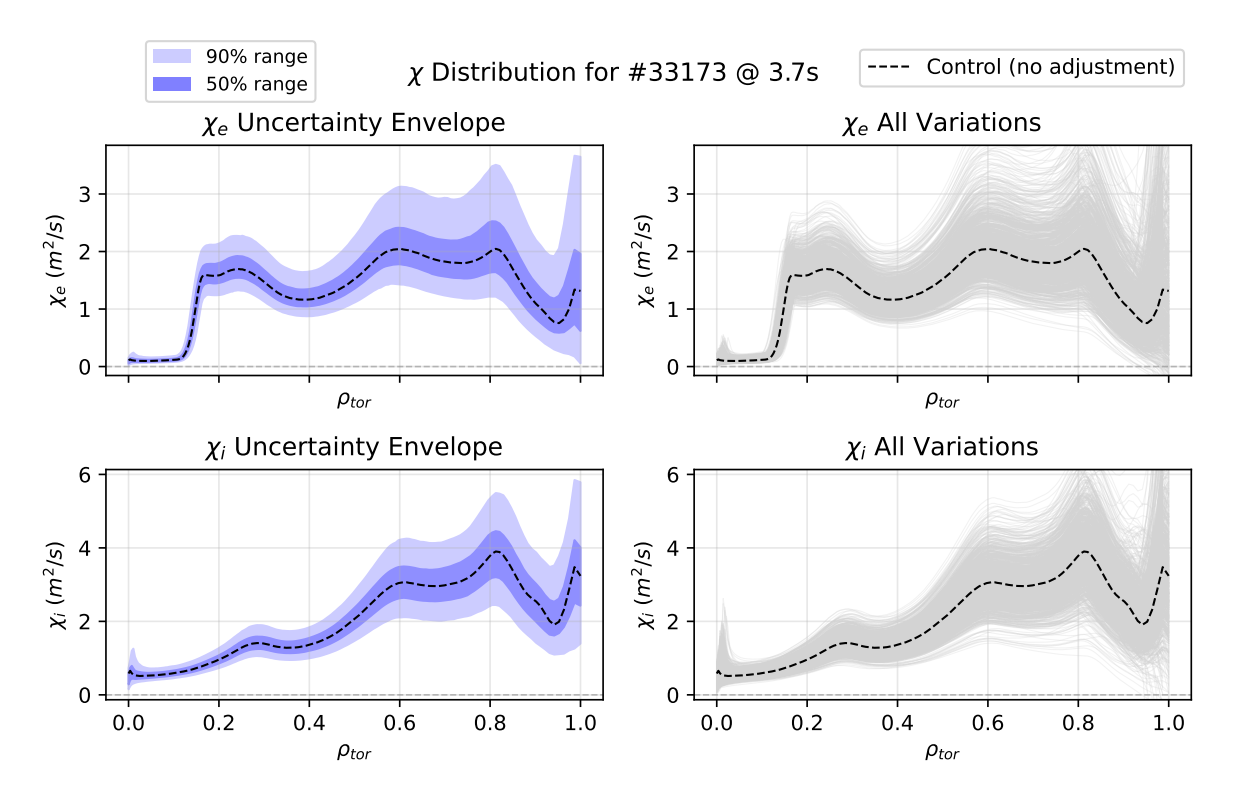
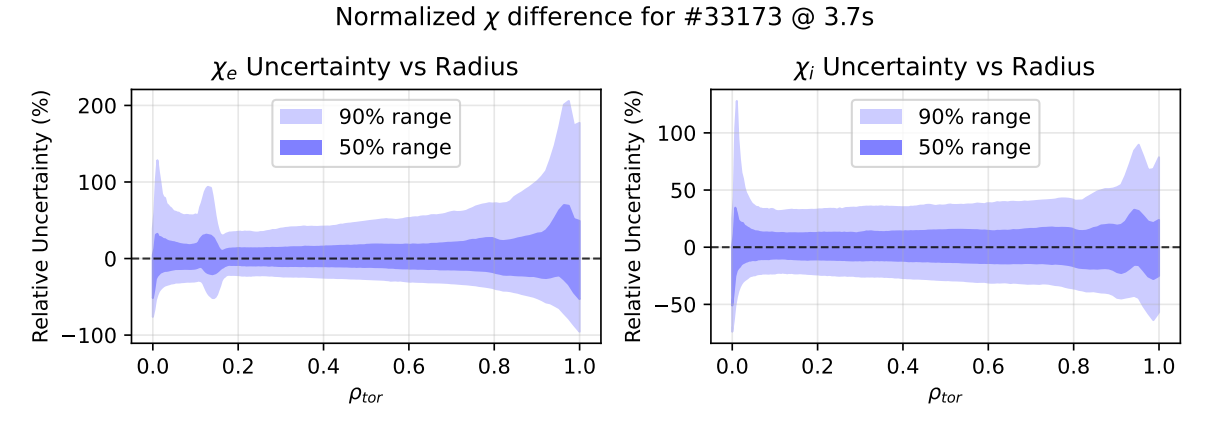


Figure 30: Effect of the profile variations on  $\chi_e$  and  $\chi_i$  for discharge #33173 at 3.7s. Left panel: Percentile envelopes for 50% and 90% bands. Right panel: All the resulting individual profiles resulting from the uncertainty sampling.

To get a more tangible view of the magnitude of the uncertainty for specific radial regions we can use the normalization approach as before. This is illustrated in Figure 31 which shows the normalized difference of the enveloping profiles of the 50 and 90 percentiles. For discharge #33173 at the specific time of 3.7s the uncertainty for 50% of the samples stays mostly within 25% and only differs in the very core ( $\rho_{tor} = 0$ ) or edge ( $\rho_{tor} = 1$ ) regions. Quite similar but a more pronounced behaviour of this can be seen for the 90th percentile of the samples which mostly stays within 50% deviation but with deviations up to 200% towards the plasma edge.



**Figure 31:** Normalized percentile envelopes and distribution of  $\chi_e$  and  $\chi_i$  profiles resulting from the uncertainty sampling for discharge #33173 at 3.7s.

To estimate the overall uncertainty for any discharge at a given time, we calculated the average deviation profile across all time points for a predefined set of discharges, as listed in Table A1. This set includes discharges currently under detailed study for impurity transport behavior [79], supplemented by additional cases with available radiation or ASTRA profiles.

For each discharge, the same input profile variations were applied. At each timestep, percentile envelopes were constructed and the differences in the resulting transport coefficient profiles were normalized to obtain the relative average discrepancy. The resulting uncertainty is presented in Figure 32.

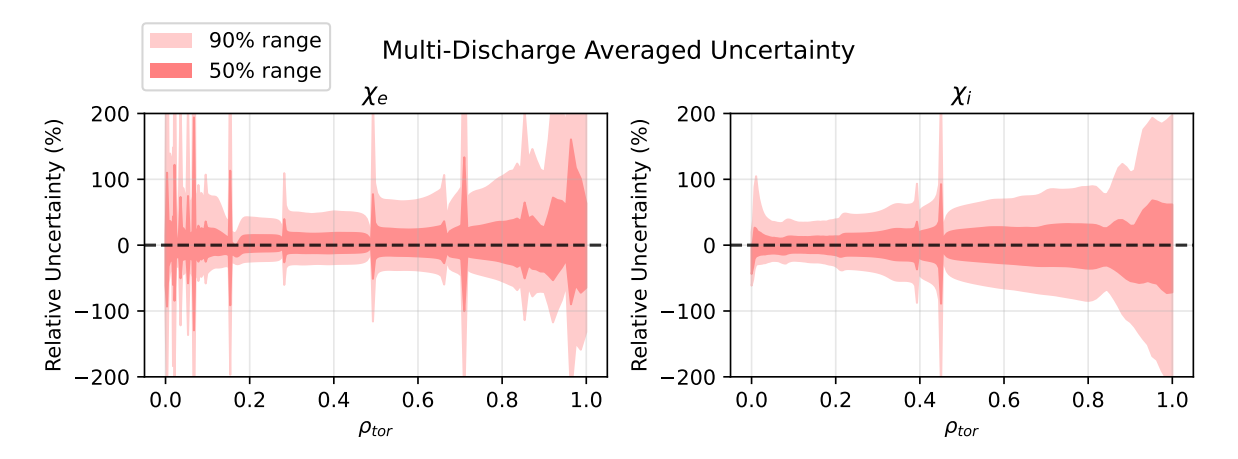


Figure 32: Averaged uncertainty profile for transport coefficient calculations across the discharge set given in A1.

These envelopes were then smoothed to produce a generalized uncertainty range for the transport coefficient calculation, as shown in Figure 33. This analysis reveals that uncertainties are typically higher in the core and edge regions of the plasma.

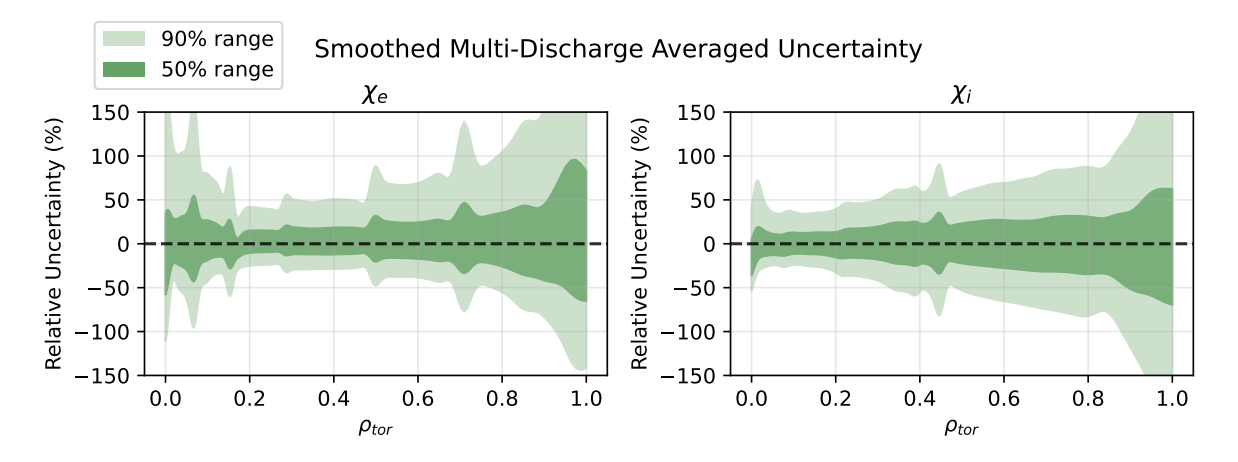


Figure 33: Smoothed generalized uncertainty range for discharge set given in A1.

It should be noted that this is not a statistically rigorous uncertainty estimate, but rather provides a practical overview of the expected precision in transport coefficient calculations. This approach offers insight into how fluctuations in key input parameters affect the results, but does not account for all possible processes or uncertainties present in a broader dataset.

### 5.4 Transport coefficient dynamics during ELM events

Edge Localized Mode (ELM) are magnetohydrodynamic instabilities that occur at the edge of H-mode plasmas in toroidal fusion devices. ELMs cause rapid losses of energy and particles from the plasma edge on millisecond timescales and their repetitive occurrence in ELMy H-mode discharges allows experimental control of the particle inventory. Understanding ELMs is crucial due to their significant impact on plasma confinement and overall reactor performance [80].

Although ELMs are not fundamentally diffusive processes, it is instructive to examine how the transport coefficients respond during these events. To do this, the shunt current (Ipolsoli) measured at the divertor plates was plotted alongside  $\chi_e$  at various radial positions. Each spike in the shunt current corresponds to an ELM event, during which particles and energy are rapidly expelled from the plasma, resulting in a dip in the stored energy  $W_{MHD}$ . This change is captured by the time derivative term  $\frac{dw}{dt}$  in the power balance equation.

Figure 34 shows the time evolution of  $\chi_e$  at selected radial positions for discharge #34257, together with the shunt current measurements. A clear response in  $\chi_e$  is observed at certain radial positions during ELM events. Most notably, at the plasma edge ( $\rho_{tor} \approx 0.8 - 1.0$ ),  $\chi_e$  increases during ELM occurrences, indicating enhanced particle and energy transport in this region. Between ELM events, a gradual rise in  $\chi_e$  is observed in the intermediate radial region ( $\rho_{tor} = 0.5 - 0.8$ ). This behavior reflects the transport of energy that was expelled during the ELM event from the core towards the edge, contributing to the recovery and rebuilding of the characteristic pedestal structure typical of high confinement mode discharges.

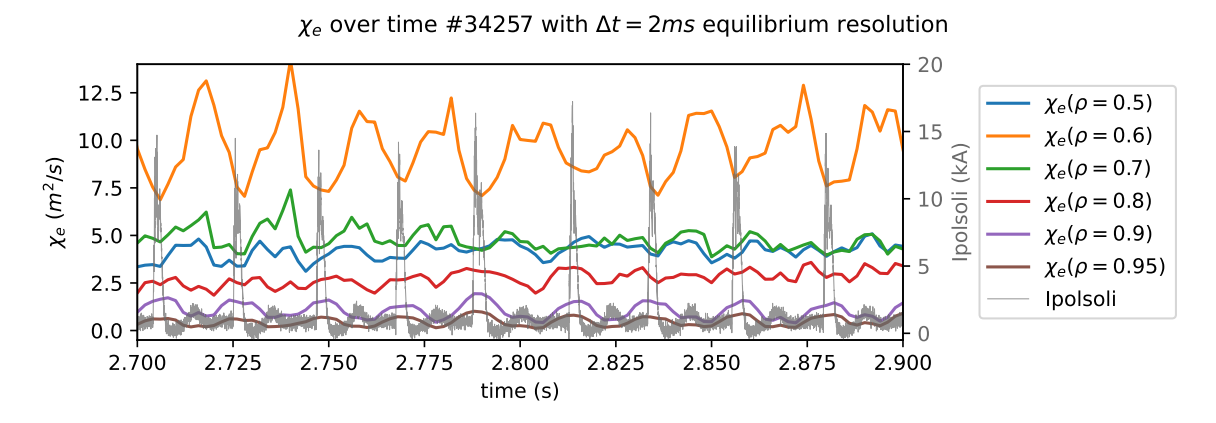


**Figure 34:** Time evolution of  $\chi_e$  at specific radial positions for discharge #34257 with 2 ms temporal resolution. The grey curve shows the shunt current at the divertor, indicating ELM events.

It should be noted that this example represents a special case with a relatively low ELM frequency ( $f_{\rm ELM}=47\pm6\,{\rm Hz}$ ), which allows equilibrium reconstruction with 2 ms time steps to adequately resolve the underlying dynamics. In contrast, most discharges exhibit more frequent and smaller ELMs occurring on timescales that are too fast to be accurately captured in the IDE reconstruction given the limitations of some diagnostics. In particular, ion density and temperature measurements are typically available only every 10 ms, restricting the achievable temporal resolution for the equilibrium reconstruction.

The impact of temporal resolution becomes evident in Figure 35, which shows results for discharge #33616 ( $f_{\rm ELM}=78\pm21\,{\rm Hz}$ ) and #33173 ( $f_{\rm ELM}=169\pm27\,{\rm Hz}$ ) with a higher ELM frequency. For #33616 in the upper panel the 2 ms time step is insufficient to completely resolve the rapid changes in temperature and density profiles and the response in  $\chi_e$  is not so clear but still observable during ELM events. For discharge #33173 in the lower panel, the ELM frequency is even higher and the 2 ms resolution fails to capture any significant response in  $\chi_e$  during ELM events.

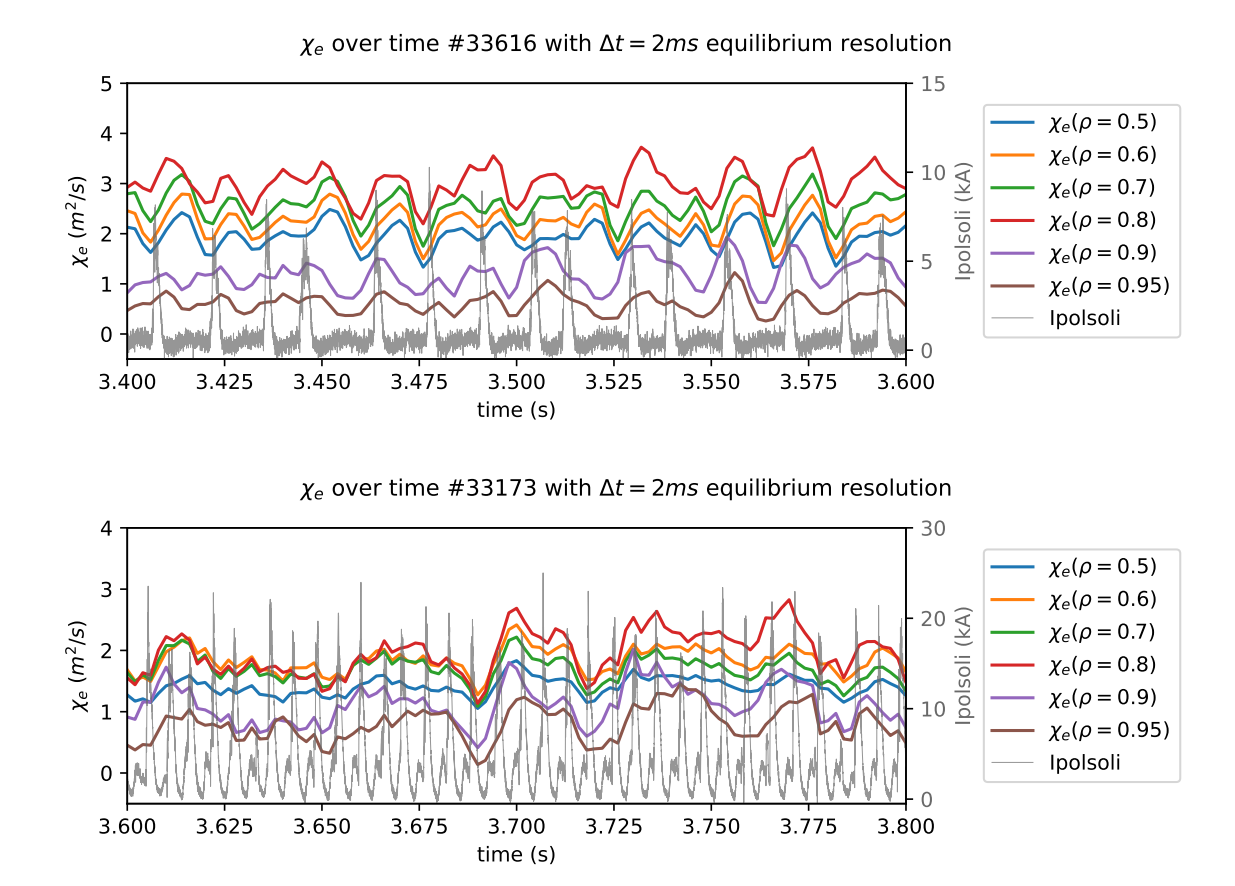


**Figure 35:** Time evolution of  $\chi_e$  at specific radial positions for discharge #33173 and #33616 with 2 ms temporal resolution. The grey curve shows the shunt current at the divertor, indicating ELM events.

### 5.5 Transient condition analysis

The choice of how to treat the transient term  $\frac{dw}{dt}$  in the transport coefficient calculation has been a subject of considerable discussion. Accurately modeling non-steady-state conditions remains a challenging and unresolved issue. One major difficulty is that the only directly comparable data for the time derivative of the stored energy is  $W_{MHD}$ , as defined in equation (23). However,  $W_{MHD}$  does not differentiate between electrons, ions or fast particles and is only available as a single value for the entire confined plasma ( $\rho_{tor} = 1$ ), without any radial resolution.

To facilitate a comparison, we take our time derivatives of the thermal energy components,  $\frac{d}{dt}(n_eT_e)$  and  $\frac{d}{dt}(n_iT_i)$  for each radial point and integrate them for the confined plasma volume (until  $\rho_{tor} = 1$ ) to obtain the total thermal energy change (excluding fast particles).

$$\frac{dW_{nT}}{dt} = \int_{V(\rho)} \left[ \frac{d(n_e T_e)}{dt} + \frac{d(n_i T_i)}{dt} \right] dV$$
 (50)

This approach provides a practical estimate of the total energy change in the plasma, which can be directly compared to  $\frac{d}{dt}W_{\text{MHD}}$  obtained from the equilibrium reconstruction. Although both methods aim to assess the same physical quantity, it is important to recognize that they are based on fundamentally different principles. Specifically,  $\frac{d}{dt}W_{\text{MHD}}$  is derived from magnetic measurements and pressure constraints within the IDE framework, whereas  $n_e$  and  $T_e$  are determined from various diagnostics and combined using the IDA approach.

Despite these differences, this comparison offers a useful benchmark for evaluating the transient condition assumption in the transport coefficient calculation.

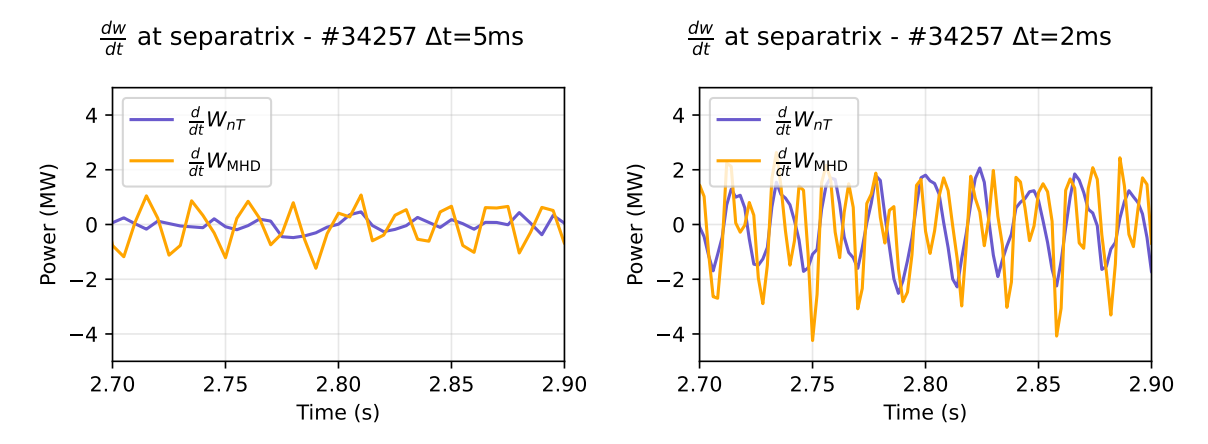


**Figure 36:** Comparison of the time derivative term  $\frac{dW}{dt}$  for discharge #34257 with 5 ms (left) and 2 ms (right) IDE equilibrium reconstruction resolution.

The left panel of Figure 36 shows the plasma energy evolution for discharge #34257 using IDE reconstructions with 5 ms time steps, where the two curves exhibit weak correlation. By increasing the temporal resolution of the equilibrium reconstruction to 2 ms, as depicted in the right panel, the curves demonstrate the expected behavior during ELM events, where the plasma energy changes periodically with each ELM.

In contrast, Figure 37 illustrates the case of discharge #33173, which exhibits a very high ELM frequency (see Figure 35). Here, increasing the temporal resolution actually decreases the accuracy of the results. Instead of averaging over the ELM

events, the higher resolution captures rapid fluctuations in the  $\frac{dW}{dt}$  term, propagating these variations through the calculation. For such high-frequency ELM cases, a 5 ms resolution would yield more consistent  $\chi$  profiles.

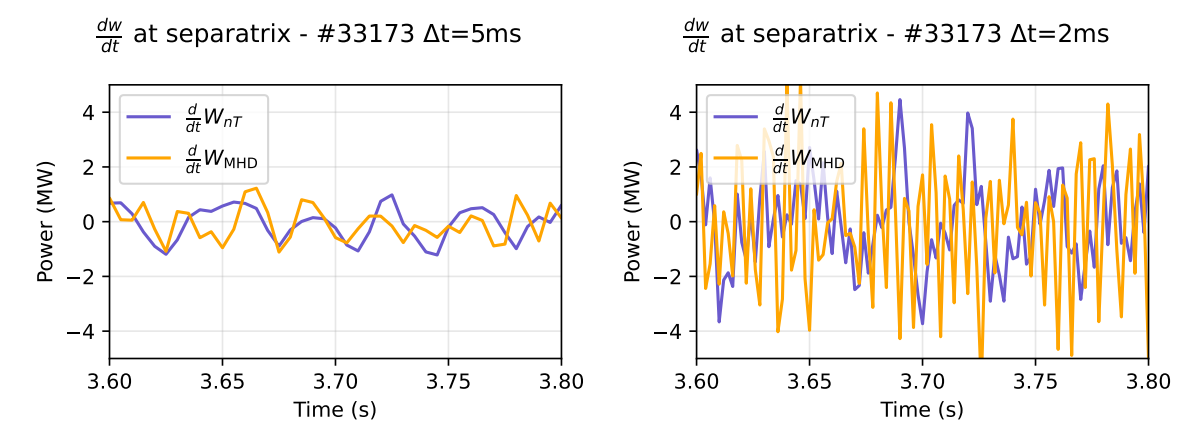


**Figure 37:** Comparison of the time derivative term  $\frac{dW}{dt}$  at  $\rho_{tor} = 1$  calculated by IDE via  $\frac{dW}{dt} = \frac{d(nT)}{dt}$  and  $\frac{d}{dt}W_{MHD}$  from the equilibrium reconstruction for discharge #33173 with 5 ms (left) and 2 ms (right) IDE resolution.

Although  $\frac{d}{dt}W_{\rm MHD}$  provides a physically more accurate/responsive measure of the plasma energy change, these results further demonstrate that the temporal resolution of the IDE equilibrium reconstruction is crucial for analyzing ELM dynamics. Ideally,  $\frac{d}{dt}W_{\rm MHD}$  would be preferred over the  $\frac{d}{dt}(n_eT_e)$  and  $\frac{d}{dt}(n_iT_i)$  data; however,  $\frac{d}{dt}W_{\rm MHD}$  is only available as a global quantity and does not provide radial profiles or as already mentioned above does not distinguish between different particle species. Nevertheless, the magnitude and overall shape of the time derivatives from both approaches show reasonable good agreement, which addresses a major uncertainty encountered during the initial formulation of the calculation.

### 5.6 Impact of Temporal Resolution

The temporal resolution of the equilibrium reconstruction plays a critical role in accurately capturing rapid plasma phenomena, especially during events such as ELMs. A finer time resolution allows the time derivative term  $\frac{dw}{dt}$  to reflect fast changes in plasma energy and profiles. However, simply increasing the resolution is not always beneficial: if the time steps are too short relative to the diagnostic capabilities or the underlying physical processes, the calculation may capture noise and unresolved fluctuations, particularly during ELM events (see Figure 35). This can introduce significant variability and artifacts into the resulting  $\chi$  profiles.

Figures 36 and 37 illustrate how the magnitude of  $\frac{dW}{dt}$  varies with different temporal resolutions. Higher resolution can reveal more rapid changes and measurement noise, which propagate directly into the calculated transport coefficients. As a result,  $\chi$  profiles for the same time point may differ substantially depending on the chosen time step for the equilibrium reconstruction. For example, a higher resolution may sample  $n_e$  and  $T_e$  immediately before and after an ELM, resulting in a pronounced change in  $\frac{dW}{dt}$ , while a lower resolution may skip over several ELMs, resulting in the same energy difference over a longer duration essentially smoothing out the gradient.

This phenomenon is demonstrated in Figure 38, where  $\chi_e$  profiles at specific time points show significant discrepancies across different temporal resolutions.

#### Transport Coefficients vs Time Resolution - Shot #33616 @ 3.5s

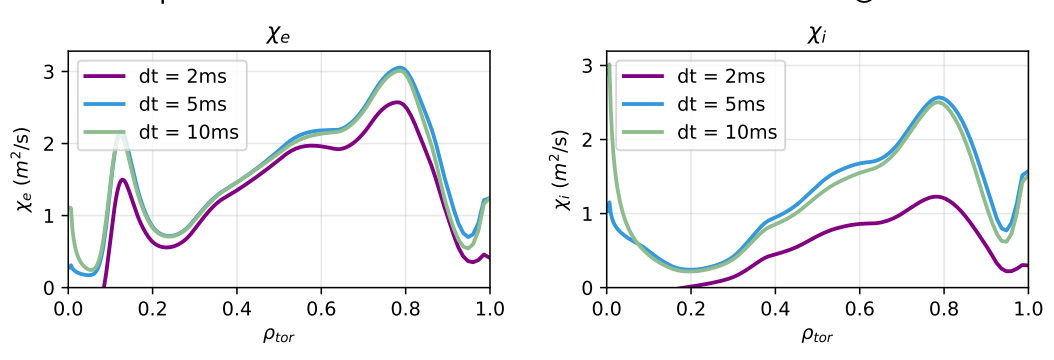


**Figure 38:** Comparison of  $\chi$  profiles for different temporal resolutions in IDE for discharge #33616 at 3.5 s.

A more comprehensive view is provided in Figure 40, which shows all  $\chi_e$  and  $\chi_i$  profiles calculated during a time window around an ELM. The 2 ms resolution captures more of the fast dynamics, resulting in greater fluctuations between profiles. In contrast, the 5 ms resolution yields more consistent profiles, and the 10 ms resolution shows only minor differences over time.

To address the variability introduced by high temporal resolution, it is useful to average the  $\chi$  profiles over the same duration as the lower-resolution analysis. Figure 40 (bottom) shows that the averaged profiles from different resolutions align well, whereas individual time points may show large discrepancies.

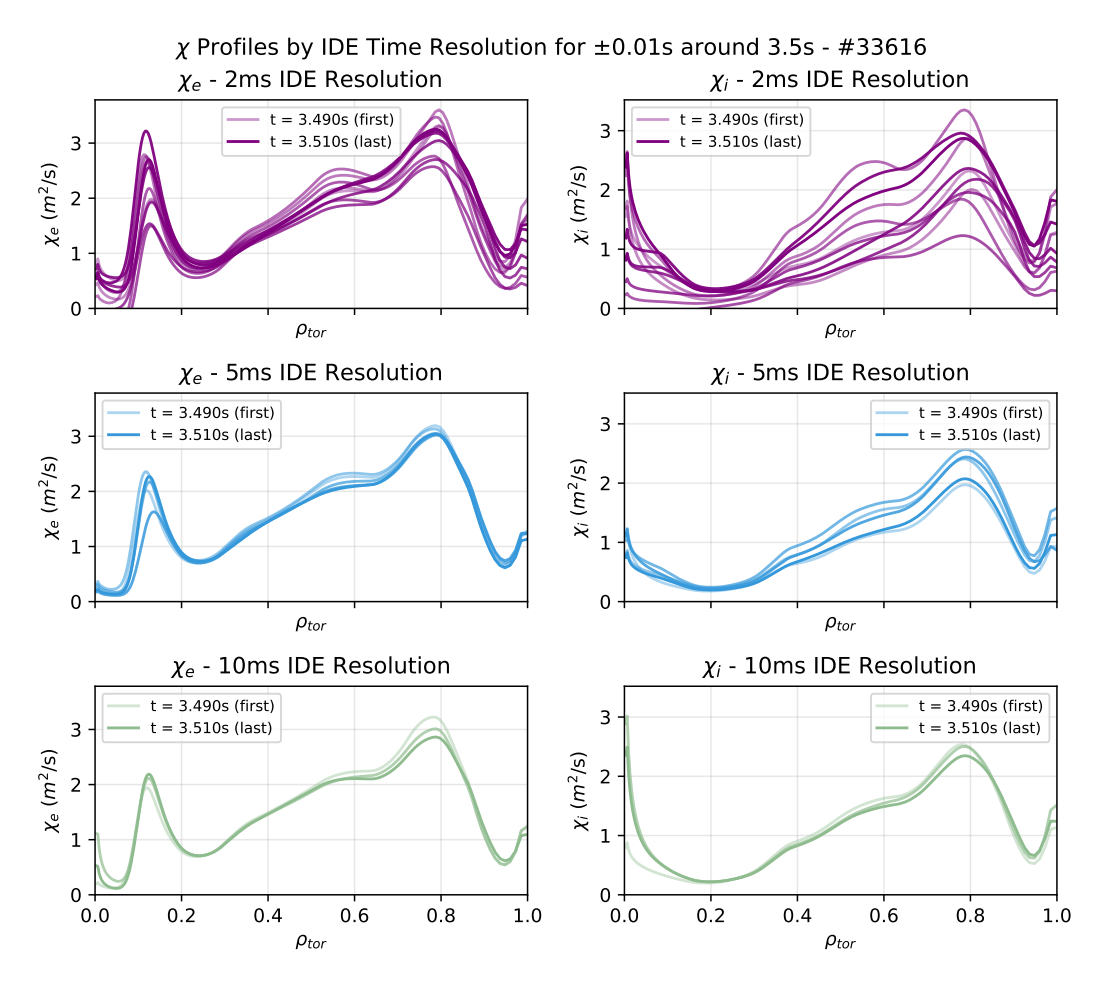


**Figure 39:** Evolution of  $\chi$  profiles for discharge #33616 at 3.5 s using different temporal resolutions in IDE.

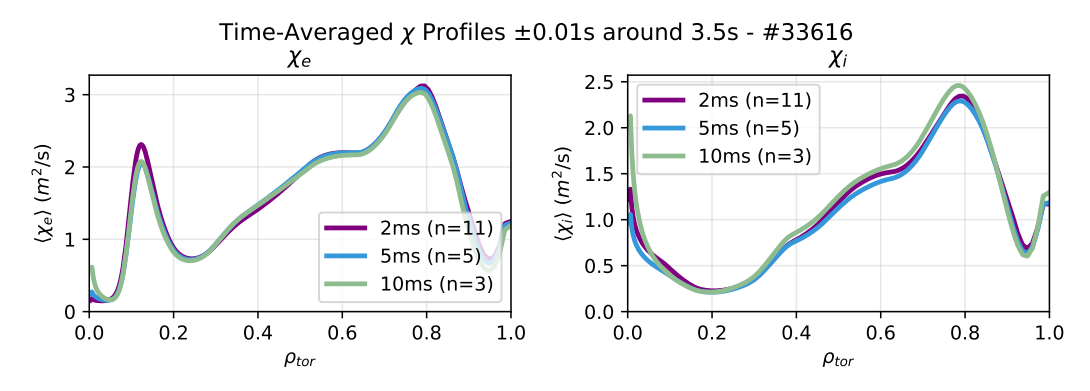


**Figure 40:** Averaged  $\chi$  profiles for different temporal resolutions in IDE for discharge #33616 at 3.5 s.

These findings highlight the importance of considering the effects of temporal resolution and the time derivative term when analyzing transport coefficients. Discharges with different equilibrium reconstruction time steps, or analyses performed without time-dependent components (as in ASTRA), may yield substantially different results. Careful selection and interpretation of the results are therefore essential.

### 6 Conclusion

This thesis has presented the current implementation of transport coefficient calculations within the IDE framework, emphasizing the critical dependence of these calculations on the accurate determination of the temperature gradient profiles. A key advancement in this work was the integration of a Gaussian Process Tomography (GPT) model to reconstruct emission profiles from bolometer measurements via tomography. The GPT code was ported to Fortran90, rigorously validated, and incorporated into the IDE framework. This process uncovered and resolved issues in the initial profile generation, leading to improved reliability across different plasma configurations.

To quantify the reliability of the transport coefficient calculations, uncertainty ranges were established for the most influential input parameters. A Monte Carlo simulation was performed, generating a spectrum of possible solutions by randomly sampling within these uncertainty ranges. The analysis revealed that, as expected, the plasma edge and core regions exhibit the largest uncertainties. In contrast, the region from  $\rho_{tor}=0.2$  to 0.5 is modeled with relatively high confidence, showing maximum deviations of about 75% in coefficient magnitude. Between  $\rho_{tor}=0.5$  and 0.8, the uncertainty gradually increases, reaching up to 100% relative difference. These results provide practical guidelines for assessing the confidence in transport coefficient calculations given typical measurement uncertainties.

The study of transport coefficient profiles during ELM events demonstrated that, with sufficiently high temporal resolution and low ELM frequency, the calculated coefficients exhibit clear periodic behavior across different radial positions, consistent with the expectations of a diffusive transport model. However, the implementation of the diffusive model required addressing the challenge posed by the commonly assumed steady-state condition (dw/dt=0), which is not generally applicable in the IDE context. Instead, the change in plasma energy for each species was approximated by the time derivative  $\frac{d}{dt}(nT)$ , a method whose limitations and comparability to other signals were discussed.

The impact of temporal resolution on the comparability of transport coefficient profiles was also explored. It was shown that profiles calculated at individual time points can differ significantly depending on the chosen time step for equilibrium reconstruction, while averaging over the same duration yields much better agreement between different resolutions.

It is important to note that the transport coefficients are derived from a diffusive model that primarily relies on temperature gradients to drive heat flow. Nevertheless, the model was able to capture non-diffusive phenomena such as ELMs, likely due to the inherent fluctuations in the density and temperature profiles. The analysis also highlighted that discharges with noisy or irregular temperature profiles, especially those with gradients passing through zero, can result in pronounced spikes in the transport coefficient profiles.

Overall, the diffusive transport model implemented and validated in IDE provides a fast and practical method for obtaining transport coefficients directly from ASDEX Upgrade's equilibrium solver, without the need to run ASTRA. This work offers valuable guidance for the application and interpretation of the resulting transport coefficient calculations within the IDE framework, supporting more accurate plasma modeling and contributing to the advancement of reliable fusion energy research.

## 7 Outlook

Several important developments remain to be addressed to further improve the accuracy and applicability of transport coefficient calculations within the IDE framework:

- ICRH Heating Implementation: The development and integration of a robust power deposition model for ICRH remains a key objective. Ongoing work focuses on creating a surrogate model capable of inferring ICRH power deposition from a limited set of input parameters [67]. This approach aims to deliver accurate, spatially resolved power density profiles efficiently, enabling their direct application in transport coefficient analysis.
- Accurate  $Z_{\text{eff}}$  Profiles: The determination of actual  $Z_{\text{eff}}$  profiles remains a challenge, as currently a singular value over the whole profile is used. Improved approaches for reconstructing  $Z_{\text{eff}}$  with higher spatial and temporal resolution would enhance impurity transport modeling and the reliability of radiative loss calculations.
- Time Derivative from GSE: Utilizing the time derivative of the stored energy (dW/dt) directly from the Grad-Shafranov Equation (GSE) offers a promising pathway, as the GSE inherently produces a pressure profile that can be integrated over the plasma volume. However, separating the contributions from electrons and ions remains problematic and further work is needed to enable species-resolved energy evolution analysis.

Addressing these points will enable more comprehensive and precise transport modeling, supporting ongoing efforts to optimize plasma performance and advance fusion research.

## Acknowledgements

I would like to express my sincere gratitude to the Max Planck Institute for Plasma Physics for the opportunity to participate in their research and for welcoming me at their facility in Garching near Munich. My deepest thanks go to Elisabeth Wolfrum for her invaluable guidance and support throughout this project. Her encouragement not only sparked my passion for this fascinating field but also made me feel immediately included in the research group as well as providing essential advice on how to approach every challenge.

I am very grateful to Rainer Fischer for his insights and patience while guiding me through the intricacies of the codebase and Fortran 90. Thank you for always taking the time to answer my questions, discuss ideas, and swiftly resolve any issues I encountered or sometimes created.

My thanks also go to Michael Bergmann for his support during my first months at IPP, for being a great counterpart to exchange ideas with and for fostering a positive working environment that encouraged my scientific growth and independence.

I would like to extend my appreciation to the entire team at IPP for their patience and for generously answering all of my questions. Thank you to the wonderful IPP community for making my time there so enjoyable.

I am deeply thankful to my family, especially my parents, for their unwavering support throughout my academic journey. Special thanks to my brother Ben for always having an open door for me during my visits to IPP in Garching, Munich.

A heartfelt thank you to Pauli, my greatest supporter in all my endeavors. Thank you for always believing in me, encouraging me when I struggled, listening to everything on my mind and checking in on me when I lost sight of myself.

Finally, I want to thank my friends, my Volleyball crew, my Löwen-WG, my Uppsala acquaintances and everyone who may not be mentioned by name but has contributed to making my world a happier place.

# **Appendix**

#### **GPT Validation**

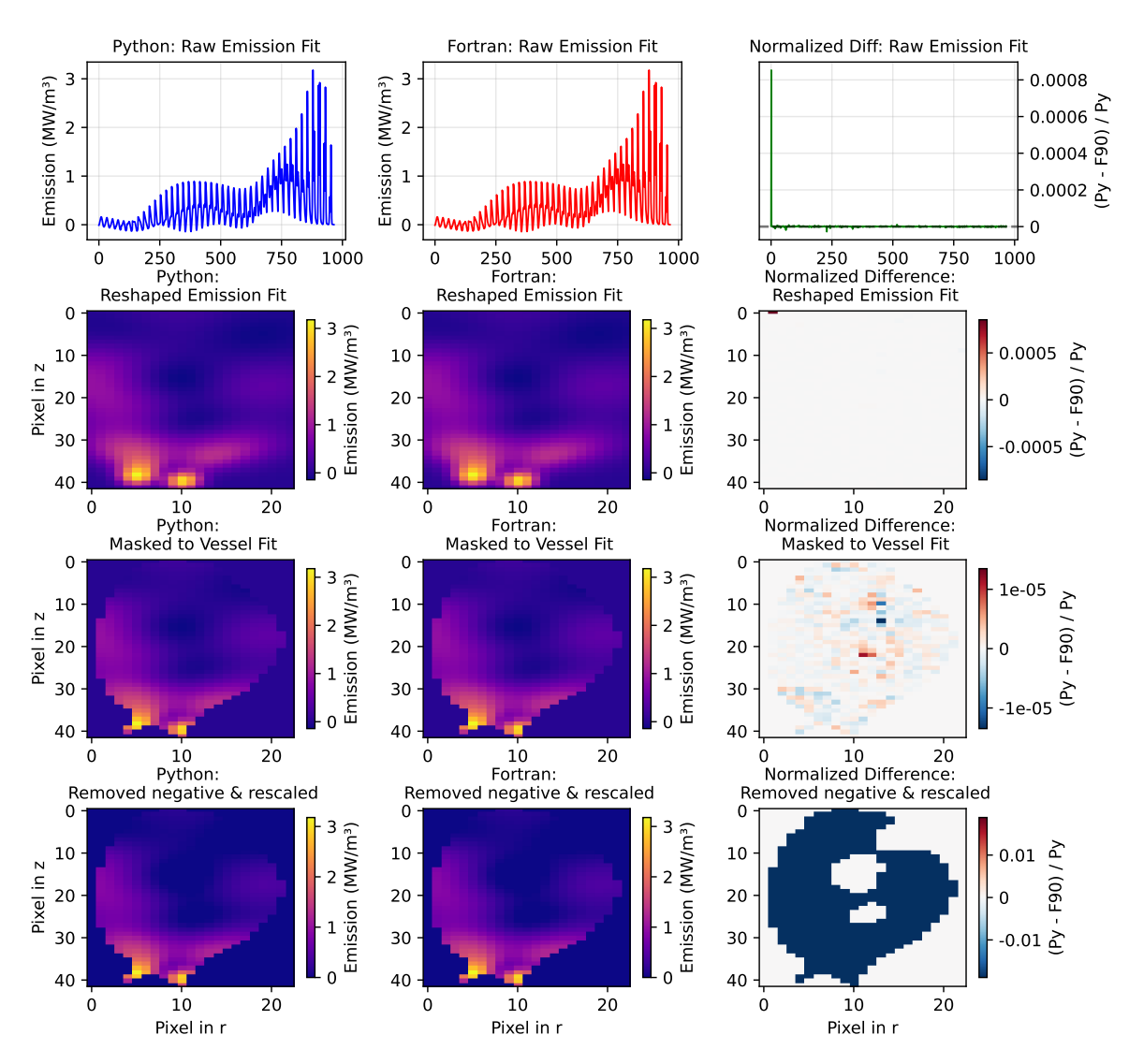
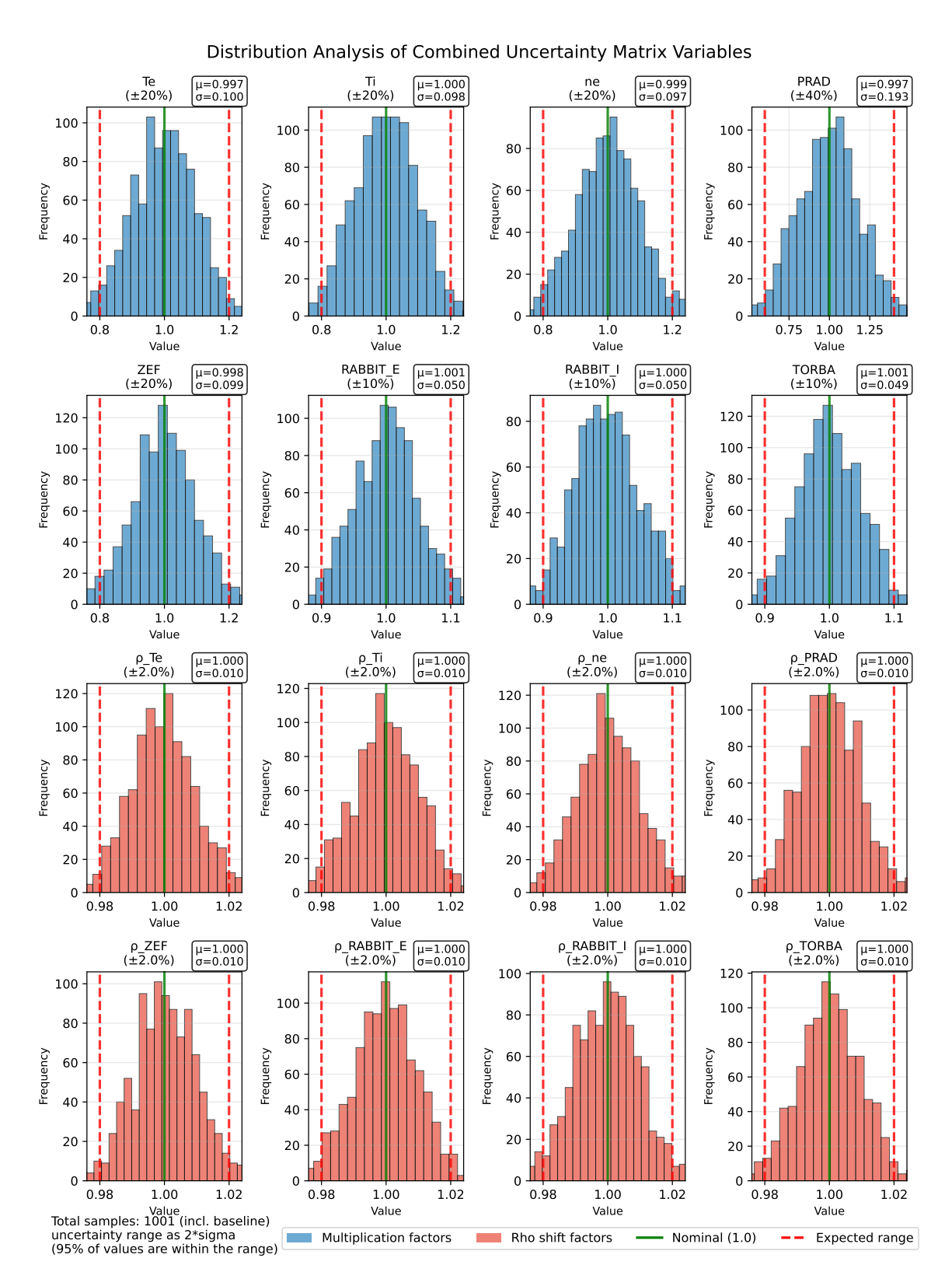


Figure A1: Validation comparison of 2D emission pixelmaps between Python and Fortran implementations for discharge #33173 at 3.7s using the IDE equilibrium for both methods. Left column: Python implementation results. Middle column: Fortran implementation results. Right column: Normalized difference between implementations. Each row shows a different stage of the emission reconstruction pipeline: from the initial raw emission fit reshaped into a pixelmap, through the application of a vessel mask that excludes pixels outside the vacuum vessel, to the removal of negative emission values and subsequent rescaling to preserve the total integrated emission.

## Distribution of uncertainty parameters



**Figure A2:** Histograms for all varied inputs for the uncertainty estimation.

Table A1: Sensitivity study discharges: Shotnumbers and analysed duration.

-	
Shotnumber	Duration
33921	$5.61 - 5.94 \mathrm{s}$
33922	$3.02 - 4.05\mathrm{s}$
34054	$4.25 - 7.26\mathrm{s}$
34257	$2.71 - 3.16\mathrm{s}$
34893	$4.42 - 5.25\mathrm{s}$
34893	$6.17 - 7.49\mathrm{s}$
34899	$2.57 - 4.13\mathrm{s}$
34899	$4.70 - 5.69\mathrm{s}$
37801	$5.56 - 5.98\mathrm{s}$
37933	$2.45 - 2.85\mathrm{s}$
38879	$4.24 - 5.33\mathrm{s}$
38909	$6.80 - 7.54\mathrm{s}$

### Acronyms

ASDEX Axially Symmetric Divertor Experiment. 1, 2, 11, 20, 22–26, 59, 66, II

**ASTRA** Automated System for TRansport Analysis. 12, 13, 28, 30–32, 36, 39–42, 52, 58, 59, 67, I, II

**CDE** Current Diffusion Equation. 10

CXRS Charge Exchange Recombination Spectroscopy. 26

**DCN** Deuterium Cyanide Laser Interferometry. 25

**ECE** Electron Cyclotron Emission. 25

ECRH Electron Cyclotron Resonance Heating. 23, 29, 40, 66

ELM Edge Localized Mode. 53–57, 59, 68, I, II

GPR Gaussian Process Regression. 18, 20, 21

GPT Gaussian Process Tomography. 20, 21, 26, 27, 34–38, 41, 42, 59, 66, 67

**GSE** Grad-Shafranov Equation. 10

ICRH Ion Cyclotron Resonance Heating. 23, 24, 29, 60

IDA Integrated Data Analyses. 2, 11, 13, 39, 55

**IDE** Integrated Data analyses Equilibrium. 2, 11, 13, 14, 21, 28, 29, 34, 35, 37, 39, 40, 42, 53, 55–60, 62, 66–68, I, II

Li-BES Lithium Beam Emission Spectroscopy. 25

LSN Lower Single Null. 34, 35, 67

MCF Magnetic Confinement Fusion. 22

MHD Magnetohydrodynamics. 10

NBI Neutral Beam Injection. 23, 29, 66

SOL Scrape-Off Layer. 8, 25, 66

**TS** Thomson Scattering. 25

USN Upper Single Null. 34, 35, 67

# List of Figures

1	Binding energy calculated from the mass defect for various numbers of	0
0	nucleons in the nucleus. [15]	3
2	Fusion cross sections versus the centre of mass energy for reactions of interest [16]	4
3	Schematic of a Tokamak [21]. The toroidal field coils are arranged around	4
0	the vaccum vessel. The vertical field coils are used to better control the	
	plasma position and shape. The transformer coils induces the plasma	
	current which is indicated by the white arrow. The path of the particles	
	follows a helical path around the nested magnetic flux surfaces (red)	
	indicated by the black magnetic field lines.	7
4	Plasma geometry inside a tokamak [24]. The magnetic field lines are	
	marked in black while detailing the plasma core in red and the SOL	
	in orange. The divertor plates can be seen in blue and intersect the	
_	sepraratrix	8
5	Example toroidal geometry from [12]. Two topologically distinct curves	
	can be used to define flux integrals, which in turn can act as labels for flux surfaces.	9
6	Panel (a): Four random functions sampled from the GP prior distribu-	9
O	tion. Panel (b): After observing two data points, the mean prediction	
	(solid line) and four samples from the posterior (dashed lines) are shown.	
	The shaded area in both plots shows twice the standard deviation at each	
	value $x$ . Taken from [40]	18
7	Posterior Gaussian process after including a measurement error. The	
	sampled functions now accurately reflect the uncertainty introduced by	
0	the measurement noise. (Taken from [44])	20
8	Overview of the Gaussian Process Tomography workflow on an example	
	discharge #33616 at 7s. Initially, bolometer data is loaded and preprocessed. Subsequently, Gaussian Process Tomography is applied to recon-	
	struct a two-dimensional emission tomogram. Finally, the tomogram is	
	radially integrated to obtain the radiated power profile as a function of	
	plasma radius. (Adapted from [43].)	21
9	Sketch of the ASDEX Upgrade tokamak [48]	22
10	Lines of sight for the bolometer channels. The blue lines resprent chan-	
	nels FHC, FVC and FDC. The red lines are FLX, FLH and FHS and	
	were excluded in the GPT analysis	27
11	Flow of data within the mod_coefficients_model.f90 module for cal-	20
12	culating diffusive transport coefficients	28
14	the power balance equation in a tokamak plasma. The figure shows	
	nested magnetic flux surfaces with the separatrix (blue line) defining the	
	plasma boundary, NBI heating trajectories (orange lines), and the ECRH	
	heating region (green shaded area). Power flows are indicated by arrows:	
	heating sources $(P_{\text{ECRH}}, P_{\text{Ohm}}, P_{\text{NBI}})$ on the right, power losses through	
	radiation $(P_{\text{rad}})$ and conducted heat flux $(Q)$ on the left and the temporal	
	change in stored plasma energy $\left(\frac{dw}{dt}\right)$ at the bottom	29

13	Radiation functions for tungsten as a function of electron temperature $T_e$ .	
	The function is used to calculate the radiative power loss in the plasma.	
	The values are based on experimental data and theoretical models [73].	33
14	Magnetic flux surfaces for two example discharges in LSN (left) and	
	USN (right) configurations. The blue line indicates the separatrix, with	
	its self-intersection point being the X-point. Gray dashed lines represent	
	additional magnetic flux surfaces for different values of $\rho_{pol}$	34
15	Erroneous pixel inclusion in radial integration for discharge #33173 at	0.
10	t=1.0s using the Python GPT implementation with CLISTE equilibrium	
	data. Left panel: Gradient colormap showing all pixels with $\rho_{pol} < 1$	
	included in the integration. Right panel: Binned colormap depicting	
	the radial bins of $\Delta \rho_{pol} = 0.1$ used for integration. The separatrix (black line) complexities have pivels in the director ration (below the V point) are	
	line) emphasizes how pixels in the divertor region (below the X-point) are	25
1.0	incorrectly included in the confined plasma radiation profile reconstruction.	30
16	Comparison of the radiative power for discharge #33173 at 1.0s. Left	
	panel: Radiative power profiles calculated by the GPT method, com-	
	paring calculations with (purple) and without (orange) the z-coordinate	
	X-point filtering condition. Right panel: Interpolated power profile nor-	0.0
1 -	malized by the interpolated volume of each radial segment	36
17	Comparison of the radiative profiles from Python via CLISTE and For-	
	tran90 via IDE equilibrium for discharge #33173 at 1.0s. Left panel:	
	Radiative power profiles calculated by the GPT method. Right panel:	
	Interpolated power profile normalized by the interpolated volume of each	
	radial segment.	37
18	Impact of different magnetic equilibria on pixel binning for discharge	
	#33173 at 1.0s. Left and middle panels: Pixel binning for radial inte-	
	gration with $\Delta \rho_{tor} = 0.1$ intervals using CLISTE and IDE equilibria,	
	respectively. Right panel: Comparison of flux surfaces from CLISTE	
	(blue) and IDE (orange) equilibria	37
19	Comparison of the electron and ion heat diffusivity $\chi_e$ and $\chi_i$ calculated	
	by the IDE and ASTRA codes for the same input data. The small	
	discrepancies which can still be seen are due to some parameters being	
	not taken over	39
20	Comparison of the electron and ion heat diffusivity $\chi_e$ and $\chi_i$ calculated	
	by the IDE and ASTRA codes for their respective input data. While the	
	overall trends are similar, several notable discrepancies are evident	39
21	Comparison of the electron power deposition profile $S_e$ calculated by the	
	IDE and ASTRA codes for discharge #33173 at 3.7s. The profiles show	
	significant differences, especially in the core and edge regions	40
22	Comparison of the calculate radiation profile (blue), the Gaussian Pro-	
	cess Tomography (orange) and the handmade tomography profile (red)	
	for shot #33173 at 3.7s and #33616 at 5.2s	41
23	Comparison of the impact of the GPT radiation profile on the transport	
	coefficients $chi_e$ and $chi_i$ for discharge #33616 at 5.2s	42
24	Impact of parameter uncertainties on input profiles for discharge #33173	
	at 3.7s	44
25	Impact of the different parameter variations on the heat diffusivities pro-	
	files of $\chi_e$ and $\chi_i$ for discharge # 33173 at 3.7 s	45

26	Normalized difference profiles showing the impact of parameter uncer-	4-
~-	tainties on the heat diffusivity $\chi_e$ and $\chi_i$ for discharge #33173 at 3.7 s.	47
27	Radially shifted input profiles for discharge #33173 at 3.7s	48
28	Effect of shifts of different parameters along the radial axis $(\rho_{tor})$ on the	
	$\chi_e$ and $\chi_i$ profiles for discharge #33173 at 3.7 s	49
29	Parameter profile envelopes (50th and 90th percentiles) resulting from	
	the sampled uncertainty ranges	50
30	Effect of the profile variations on $\chi_e$ and $\chi_i$ for discharge #33173 at	
	3.7 s. Left panel: Percentile envelopes for 50% and 90% bands. Right	
	panel: All the resulting individual profiles resulting from the uncertainty	
	sampling.	51
31	Normalized percentile envelopes and distribution of $\chi_e$ and $\chi_i$ profiles	
	resulting from the uncertainty sampling for discharge $\#33173$ at $3.7 \mathrm{s.}$ .	51
32	Averaged uncertainty profile for transport coefficient calculations across	
	the discharge set given in A1	52
33	Smoothed generalized uncertainty range for discharge set given in A1	52
34	Time evolution of $\chi_e$ at specific radial positions for discharge #34257	
	with 2 ms temporal resolution. The grey curve shows the shunt current	
	at the divertor, indicating ELM events	53
35	Time evolution of $\chi_e$ at specific radial positions for discharge #33173	
	and #33616 with 2 ms temporal resolution. The grey curve shows the	
2.0	shunt current at the divertor, indicating ELM events	54
36	Comparison of the time derivative term $\frac{dW}{dt}$ for discharge #34257 with	
07	5  ms (left) and $2  ms (right)$ IDE equilibrium reconstruction resolution.	55
37	Comparison of the time derivative term $\frac{dW}{dt}$ at $\rho_{tor} = 1$ calculated by	
	IDE via $\frac{dW}{dt} = \frac{d(nT)}{dt}$ and $\frac{d}{dt}W_{\text{MHD}}$ from the equilibrium reconstruction	
	for discharge $\#33173$ with $5\mathrm{ms}$ (left) and $2\mathrm{ms}$ (right) IDE resolution	56
38	Comparison of $\chi$ profiles for different temporal resolutions in IDE for	
	discharge #33616 at 3.5 s	57
39	Evolution of $\chi$ profiles for discharge #33616 at 3.5 s using different tem-	
4.0	poral resolutions in IDE	58
40	Averaged $\chi$ profiles for different temporal resolutions in IDE for discharge	
A -1	#33616 at 3.5 s	58
A1	Validation comparison of 2D emission pixelmaps between Python and	
	Fortran implementations for discharge #33173 at 3.7s using the IDE	
	equilibrium for both methods. Left column: Python implementation re-	
	sults. Middle column: Fortran implementation results. Right column:	
	Normalized difference between implementations. Each row shows a dif-	
	ferent stage of the emission reconstruction pipeline: from the initial raw	
	emission fit reshaped into a pixelmap, through the application of a vessel	
	mask that excludes pixels outside the vacuum vessel, to the removal of	
	negative emission values and subsequent rescaling to preserve the total	ee
4.0	integrated emission	62
A2	Histograms for all varied inputs for the uncertainty estimation	63

## List of Tables

1	Sensitivity study parameters: Expected uncertainties in plasma param-	
	eters	43
A1	Sensitivity study discharges: Shotnumbers and analysed duration	64

### Use of Generative AI Tools in Thesis Preparation

In accordance with the "Living Guidelines on the Responsible Use of Generative AI in Research", as endorsed by the Technical University of Vienna<sup>2</sup>, and in alignment with ethical research practices, I transparently declare the usage and scope of various AI-based tools in the preparation of this thesis. These tools were used to enhance the quality of my work, particularly in areas such as writing, coding, and language translation, while adhering to the principles of responsible AI usage as outlined by the European research community.

The AI tools utilized in this thesis include:

- ChatGPT: Employed for rephrasing sentences, refining language and generating ideas to improve the clarity and readability of text passages. All suggestions made by ChatGPT were critically evaluated and adapted to ensure they accurately reflected my original research and understanding.
- **GitHub Copilot:** Used as an assistant for coding-related tasks, bug fixing and providing suggestions and solutions to programming challenges encountered during the development of specific projects. The code generated by GitHub Copilot was reviewed and modified to meet the specific needs of the research.
- **DeepL:** Applied for translating non-English research materials and refining translated content to ensure accurate and nuanced language representation.
- **Grammarly:** Utilized to correct grammatical errors and spelling mistakes as well as improve overall sentence structure, contributing to the linguistic quality of the thesis.

The integration of these AI tools was conducted in a manner consistent with the recommendations provided in the "Living Guidelines", ensuring that they served as supplementary aids rather than replacements for critical analysis and original thought. The transparent use of these tools reflects my commitment to leveraging advanced technologies while maintaining academic integrity in scientific research.

Raffael Wendlinger

Date: 19.09.2025

 $<sup>^1</sup>$  European Commission, 20.03.2024, Living guidelines on the responsible use of generative AI in research available at: https://research-and-innovation.ec.europa.eu/document/2b6cf7e5-36ac-41cb-aab5-0d32050143dc\_en (accessed: 26.07.2025).

<sup>&</sup>lt;sup>2</sup> Technical University of Vienna, 20.03.2024, TU Wien News Article available at: https://www.tuwien.at/en/tu-wien/news/news-articles/news/leitlinien-fuer-den-verantwortungsvollen-einsatz-generativer-ki-in-der-forschung (accessed: 26.07.2025).

### **Bibliography**

- Isaac Newton. The Correspondence of Isaac Newton. Ed. by A. Rupert Hall and Laura Tilling.
   Vol. 5. Cambridge University Press, 1975, pp. 1709–1713.
- [2] International Energy Agency. *Energy and AI*. IEA, Paris. Licence: CC BY 4.0. IEA. 2025. URL: https://www.iea.org/reports/energy-and-ai.
- [3] ENTSO-E. *Iberian Peninsula Blackout 28 April 2025*. Working documentation and preliminary information on the blackout affecting Spain and Portugal. European Network of Transmission System Operators for Electricity (ENTSO-E). Apr. 2025. URL: https://www.entsoe.eu/news/2025/04/28/iberian-peninsula-blackout/. (accessed: 12.06.2025).
- [4] Bundesministerium für Bildung und Forschung (BMBF). Positionspapier Fusionsforschung: Auf dem Weg zur Energieversorgung von morgen. Positionspapier über Magnet- und Laserfusionsforschung. May 2023. URL: https://www.bmbf.de/SharedDocs/Downloads/de/2023/230522-memorandum-laser-inertial-fusion-energy.html. (accessed: 12.06.2025).
- [5] CDU/CSU-Fraktion im Deutschen Bundestag. Neue Energie-Agenda für Deutschland: Bezahlbar, sauber, sicher Energiepolitik für den Weg zum klimaneutralen Industrieland. Diskussionsentwurf für den Energie-Kongress am 5. November 2024. Diskussionspapier. Nov. 2024. URL: https://www.cducsu.de/sites/default/files/2024-11/241104\_Diskussionspapier\_Energie\_0.pdf. (accessed: 12.06.2025).
- [6] International Atomic Energy Agency. Can fusion cause a nuclear accident? Vienna. URL: https://www.iaea.org/topics/energy/fusion/faqs. (accessed: 27.06.2025).
- [7] B. Nie et al. "Insights into potential consequences of fusion hypothetical accident, lessons learnt from the former fission accidents". In: *Environmental Pollution* 245 (2019), pp. 921–931. DOI: 10.1016/j.envpol.2018.11.075.
- [8] S. M. Gonzalez de Vicente et al. Overview on the management of radioactive waste from fusion facilities: ITER, demonstration machines and power plants. 2022. DOI: 10.1088/1741-4326/ ac62f7.
- [9] D Maisonnier, D Campbell, I Cook, L Di Pace, L Giancarli, J Hayward, A Li Puma, M Medrano, P Norajitra, M Roccella, et al. "Power plant conceptual studies in Europe". In: Nuclear Fusion 47.11 (2007), p. 1524.
- [10] J. Wesson and D.J. Campbell. *Tokamaks*. International Series of Monographs on Physics. Oxford University Press, 2011. ISBN: 9780199592234.
- [11] E.J. Doyle, W.A. Houlberg, Y. Kamada, V. Mukhovatov, T.H. Osborne, A. Polevoi, G. Bateman, J.W. Connor, J.G. Cordey, T. Fujita, X. Garbet, T.S. Hahm, L.D. Horton, A.E. Hubbard, F. Imbeaux, F. Jenko, J.E. Kinsey, Y. Kishimoto, J. Li, T.C. Luce, Y. Martin, M. Ossipenko, V. Parail, A. Peeters, T.L. Rhodes, J.E. Rice, C.M. Roach, V. Rozhansky, F. Ryter,

- G. Saibene, R. Sartori, A.C.C. Sips, J.A. Snipes, M. Sugihara, E.J. Synakowski, H. Takenaga, T. Takizuka, K. Thomsen, M.R. Wade, H.R. Wilson, ITPA Transport Physics Topical Group, ITPA Confinement Database, Modelling Topical Group, ITPA Pedestal, and Edge Topical Group. "Chapter 2: Plasma confinement and transport". In: *Nuclear Fusion* 47.6 (June 2007), S18. DOI: 10.1088/0029-5515/47/6/S02.
- [12] H. Zohm, ed. Magnetohydrodynamic Stability of Tokamaks. Wiley-VCH Verlag GmbH Co. KGaA, 2014. ISBN: 978-3527677375.
- [13] Alexander E. Lifschitz. Magnetohydrodynamics and Spectral Theory. 1st ed. Developments in Electromagnetic Theory and Applications. Kluwer Academic Publishers 1989. Topics: Nuclear Physics, Heavy Ions, Hadrons. Springer Dordrecht, 1989, pp. XII, 446. ISBN: 978-94-009-2561-8.
  DOI: 10.1007/978-94-009-2561-8.
- [14] W. Demtröder. "Experimentalphysik 4: Kern-, Teilchen- und Astrophysik". ger. In: 5. Aufl. 2017. Springer-Lehrbuch. Springer Berlin Heidelberg Imprint: Springer Spektrum, 2017. Chap. 8.4, pp. 220–225. DOI: 10.1007/978-3-662-52884-6.
- [15] Wikimedia Commons. File:Binding energy curve common isotopes.svg Wikimedia Commons, the free media repository. (accessed 27.06.2025). 2023. URL: https://commons.wikimedia.org/w/index.php?title=File:Binding\_energy\_curve\_-\_common\_isotopes.svg&oldid=741566373.
- [16] S. Atzeni and J. Meyer-ter-Vehn. The Physics of Inertial Fusion: BeamPlasma Interaction, Hydrodynamics, Hot Dense Matter. Oxford University Press, June 2004. DOI: 10.1093/acprof: oso/9780198562641.001.0001.
- [17] J D Lawson. "Some Criteria for a Power Producing Thermonuclear Reactor". In: *Proceedings of the Physical Society. Section B* (Jan. 1957). DOI: 10.1088/0370-1301/70/1/303.
- [18] Steven C. Cowley. "The quest for fusion power". In: Nature Physics 12.5 (2016), pp. 384–386.
  ISSN: 1745-2481. DOI: 10.1038/nphys3719.
- [19] International Energy Agency (IEA). Global Energy Review 2025. Tech. rep. Licence: CC BY 4.0. Paris: IEA, 2025. URL: https://www.iea.org/reports/global-energy-review-2025.
- [20] U. Stroth. *Plasmaphysik : Phänomene, Grundlagen und Anwendungen.* ger. 2. Auflage. Berlin: Springer Spektrum, 2018, p. 349. DOI: 10.1007/978-3-662-55236-0.
- [21] Max Planck Institute for Plasma Physics. Magnet System of a Tokamak Fusion Device. URL: https://www.ipp.mpg.de/14869/tokamak. (accessed: 30.06.2025).
- [22] J. P. Freidberg. *Plasma Physics and Fusion Energy*. Cambridge University Press, 2008. ISBN: 978-0-521-73317-5.
- [23] F. F. Chen. Introduction to plasma physics and controlled fusion. eng. 2. ed., 4. print. Plenum Press, 1990. DOI: 10.1007/978-3-319-22309-4.

- [24] Matthew Moynihan and Alfred B. Bortz. "Tokamaks and Spherical Tokamaks". In: Fusion's Promise: How Technological Breakthroughs in Nuclear Fusion Can Conquer Climate Change on Earth (And Carry Humans To Mars, Too). Cham: Springer International Publishing, 2023, pp. 123–151. ISBN: 978-3-031-22906-0. DOI: 10.1007/978-3-031-22906-0\_6.
- [25] A. J. Creely, M. J. Greenwald, S. B. Ballinger, D. Brunner, J. Canik, J. Doody, T. Fülöp, D. T. Garnier, R. Granetz, T. K. Gray, and et al. "Overview of the SPARC tokamak". In: *Journal of Plasma Physics* 86.5 (2020), p. 865860502. DOI: 10.1017/S0022377820001257.
- [26] Jr. Spitzer Lyman. "The Stellarator Concept". In: The Physics of Fluids 1.4 (July 1958), pp. 253–264. ISSN: 0031-9171. DOI: 10.1063/1.1705883.
- [27] C. R. Burnett, D. J. Grove, R. W. Palladino, T. H. Stix, and K. E. Wakefield. "The Divertor, a Device for Reducing the Impurity Level in a Stellarator". In: *The Physics of Fluids* 1.5 (Sept. 1958), pp. 438–445. ISSN: 0031-9171. DOI: 10.1063/1.1724361.
- [28] P. Martin P.J. McCarthy and W. Schneider. "The CLISTE interpretive equilibrium code". In: IPP-5/85 (1999). PLASMA PHYSICS AND FUSION TECHNOLOGY. URL: http://inis. iaea.org/search/search.aspx?orig\_q=RN:31057068. (accessed: 16.08.2024).
- [29] H. Grad and H. Rubin. "Hydromagnetic equilibria and force-free fields". In: Journal of Nuclear Energy (1954) 7.3-4 (1958), pp. 284–285. DOI: 10.1016/0891-3919(58)90139-6.
- [30] V. D. Shafranov. Plasma equilibrium in a magnetic field. Vol. 2. Reviews of plasma physics. Consultants Bureau, 1966.
- [31] R. Fischer, C. Wendland, A. Dinklage, S. Gori, V. Dose, and the W7-AS team. "Thomson scattering analysis with the Bayesian probability theory". In: *Plasma Physics and Controlled Fusion* 44.8 (July 2002), p. 1501. DOI: 10.1088/0741-3335/44/8/306.
- [32] A. Dinklage R. Fischer and E. Pasch. "Bayesian modelling of fusion diagnostics". In: *Plasma Physics and Controlled Fusion* 45.7 (May 2003), p. 1095. DOI: 10.1088/0741-3335/45/7/304.
- [33] R. Fischer, A. Bock, M. Dunne, J.C. Fuchs, L. Giannone, K. Lackner, P.J. McCarthy, E. Poli, R. Preuss, M. Rampp, M. Schubert, J. Stober, W. Suttrop, G. Tardini, and M. Weiland. "Coupling of the Flux Diffusion Equation with the Equilibrium Reconstruction at ASDEX Upgrade". In: Fusion Science and Technology 69 (Apr. 2016), pp. 526–536. DOI: 10.13182/FST15-185.
- [34] F. Felici, O. Sauter, S. Coda, B.P. Duval, T.P. Goodman, J-M. Moret, J.I. Paley, and the TCV Team. "Real-time physics-model-based simulation of the current density profile in tokamak plasmas". In: Nuclear Fusion 51.8 (Aug. 2011), p. 083052. DOI: 10.1088/0029-5515/51/8/ 083052.
- [35] G.V. Pereverzev and P.N. Yushmanov. "ASTRA Automated System for TRansport Analysis". In: IPP 5/98 (Feb. 2002). URL: https://hdl.handle.net/11858/00-001M-0000-0027-61A2-7. (accessed: 30.06.2025).

- [36] R. Fischer, C. J. Fuchs, B. Kurzan, W. Suttrop, E. Wolfrum, and and. "Integrated Data Analysis of Profile Diagnostics at ASDEX Upgrade". In: Fusion Science and Technology 58.2 (2010), pp. 675–684. DOI: 10.13182/FST10-110.
- [37] Ulrich Stroth. "Transportprozesse im Plasma". In: Plasmaphysik: Phänomene, Grundlagen, Anwendungen. Wiesbaden: Vieweg+Teubner, 2011, pp. 239–273. ISBN: 978-3-8348-8326-1. DOI: 10.1007/978-3-8348-8326-1\_8.
- [38] Ira B Bernstein, EA Frieman, Martin David Kruskal, and RM91737 Kulsrud. "An energy principle for hydromagnetic stability problems". In: Proceedings of the Royal Society of London. Series A. Mathematical and Physical Sciences 244.1236 (1958), pp. 17–40.
- [39] L Giannone, M Weiland, R Fischer, Ondrej Kudlacek, T Lunt, M Maraschek, B Sieglin, W Suttrop, G Conway, Mark Dunne, E Fable, J Fuchs, A Gude, Valentin Igochine, P McCarthy, and R McDermott. "Magnetics only real-time equilibrium reconstruction on ASDEX Upgrade". In: Plasma Physics and Controlled Fusion 66 (Mar. 2024). DOI: 10.1088/1361-6587/ad2c2b.
- [40] Carl Edward Rasmussen and Christopher K. I. Williams. Gaussian Processes for Machine Learning (Adaptive Computation and Machine Learning). The MIT Press, 2005. ISBN: 026218253X.
- [41] Eric Schulz, Maarten Speekenbrink, and Andreas Krause. "A tutorial on Gaussian process regression: Modelling, exploring, and exploiting functions". In: *Journal of mathematical psychology* 85 (2018), pp. 1–16.
- [42] G. E. Uhlenbeck and L. S. Ornstein. "On the Theory of the Brownian Motion". In: *Phys. Rev.* 36 (5 Sept. 1930), pp. 823–841. DOI: 10.1103/PhysRev.36.823.
- [43] K. Moser. "Transport Modeling with Experimental Data and Machine Learning at ASDEX Upgrade". PhD thesis. Aug. 2023. DOI: 10.13140/RG.2.2.26238.77128.
- [44] K. Moser. "Gaussian Processes for Emission Tomography at ASDEX Upgrade". PhD thesis. June 2020. DOI: 10.13140/RG.2.2.18673.30567.
- [45] K. Moser, A. Bock, P. David, M. Bernert, R. Fischer, and ASDEX Upgrade Team. "Gaussian Process Tomography at ASDEX Upgrade with Magnetic Equilibrium Information and Nonstationary Kernels". In: Fusion Science and Technology 78.8 (2022), pp. 607–616. DOI: 10.1080/15361055.2022.2072659.
- [46] A. Kallenbach, for the ASDEX Upgrade Team, and the EUROfusion MST1 Team. "Overview of ASDEX Upgrade results". In: Nuclear Fusion 57.10 (June 2017), p. 102015. DOI: 10.1088/1741-4326/aa64f6.
- [47] G. Federici, C. Bachmann, L. Barucca, W. Biel, L. Boccaccini, R. Brown, C. Bustreo, S. Ciattaglia, F. Cismondi, M. Coleman, V. Corato, C. Day, E. Diegele, U. Fischer, T. Franke, C. Gliss, A. Ibarra, R. Kembleton, A. Loving, F. Maviglia, B. Meszaros, G. Pintsuk, N. Taylor, M.Q. Tran, C. Vorpahl, R. Wenninger, and J.H. You. "DEMO design activity in Europe: Progress and updates". In: Fusion Engineering and Design 136 (2018). Special Issue: Proceedings

- of the 13th International Symposium on Fusion Nuclear Technology (ISFNT-13), pp. 729-741.

  DOI: 10.1016/j.fusengdes.2018.04.001.
- [48] ASDEX Upgrade Drawing Gallery. ASDEX Upgrade Drawing Gallery. 2023. URL: https://www.aug.ipp.mpg.de/aug/local/aug\_only/AUG\_Aufbau/Drawing\_Gallery/index.htm. (accessed: 27.05.2024).
- [49] W. Demtröder. Experimentalphysik 4: Kern-, Teilchen- und Astrophysik. ger. 5. Aufl. 2017. Springer-Lehrbuch. Springer Berlin Heidelberg Imprint: Springer Spektrum, 2017. DOI: 10.1007/978-3-662-52884-6.
- [50] M. Weiland, R. Bilato, B. Sieglin, F. Felici, L. Giannone, O. Kudlacek, M. Rampp, M. Scheffer, W. Treutterer, T. Zehetbauer, the ASDEX Upgrade Team, and the EUROfusion MST1 Team. "Real-time implementation of the high-fidelity NBI code RABBIT into the discharge control system of ASDEX Upgrade". In: Nuclear Fusion 63.6 (Apr. 2023), p. 066013. DOI: 10.1088/1741-4326/acc31c. URL: https://dx.doi.org/10.1088/1741-4326/acc31c.
- [51] D Wagner, J Stober, F Leuterer, F Monaco, S Müller, M Münich, CJ Rapson, M Reich, M Schubert, H Schütz, et al. "Status, operation, and extension of the ECRH system at ASDEX upgrade". In: *Journal of Infrared, Millimeter, and Terahertz Waves* 37.1 (2016), pp. 45–54.
- [52] E. Poli, A. Bock, M. Lochbrunner, O. Maj, M. Reich, A. Snicker, A. Stegmeir, F. Volpe, N. Bertelli, R. Bilato, G.D. Conway, D. Farina, F. Felici, L. Figini, R. Fischer, C. Galperti, T. Happel, Y.R. Lin-Liu, N.B. Marushchenko, U. Mszanowski, F.M. Poli, J. Stober, E. Westerhof, R. Zille, A.G. Peeters, and G.V. Pereverzev. "TORBEAM 2.0, a paraxial beam tracing code for electron-cyclotron beams in fusion plasmas for extended physics applications". In: Computer Physics Communications 225 (2018), pp. 36-46. ISSN: 0010-4655. DOI: https://doi.org/10.1016/j.cpc.2017.12.018. URL: https://www.sciencedirect.com/science/article/pii/S001046551730423X.
- [53] Fusion Physics. Non-serial Publications. Vienna: INTERNATIONAL ATOMIC ENERGY AGENCY, 2012. ISBN: 978-92-0-130410-0. URL: https://www.iaea.org/publications/8879/ fusion-physics.
- [54] F Braun, F Hofmeister, F Wesner, W Becker, H Faugel, D Hartmann, and J-M Noterdaeme. "ICRF system enhancements at ASDEX upgrade". In: Fusion engineering and design 56 (2001), pp. 551–555.
- [55] N.C. Luhmann, H. Bindslev, H. Park, J. Sanchez, G. Taylor, and C.X. Yu. "Microwave diagnostics". English. In: Fusion Science and Technology 53.2 (2008), pp. 335–396. ISSN: 1536-1055. DOI: 10.13182/FST08-A1675.
- [56] S. K. Rathgeber, L. Barrera, T. Eich, R. Fischer, B. Nold, W. Suttrop, M. Willensdorfer, E. Wolfrum, and the ASDEX Upgrade Team. "Estimation of edge electron temperature profiles via forward modelling of the electron cyclotron radiation transport at ASDEX Upgrade". In: Plasma

- Physics and Controlled Fusion 55.2 (Dec. 2012), p. 025004. DOI: 10.1088/0741-3335/55/2/025004.
- [57] A. Murari, L. Zabeo, A. Boboc, D. Mazon, and M. Riva. "Real-time recovery of the electron density from interferometric measurements affected by fringe jumps". In: Review of Scientific Instruments 77.7 (July 2006), p. 073505. ISSN: 0034-6748. DOI: 10.1063/1.2219731.
- [58] R. Fischer, E. Wolfrum, J. Schweinzer, and the ASDEX Upgrade Team. "Probabilistic lithium beam data analysis". In: *Plasma Physics and Controlled Fusion* 50.8 (June 2008), p. 085009. DOI: 10.1088/0741-3335/50/8/085009.
- [59] J. Schweinzer, E. Wolfrum, F. Aumayr, M. Pockl, H. Winter, R. P. Schorn, E. Hintz, and A. Unterreiter. "Reconstruction of plasma edge density profiles from Li I (2s-2p) emission profiles". In: Plasma Physics and Controlled Fusion 34.7 (July 1992), p. 1173. DOI: 10.1088/0741-3335/34/7/001.
- [60] B. Kurzan and H. D. Murmann. "Edge and core Thomson scattering systems and their calibration on the ASDEX Upgrade tokamak". In: Review of Scientific Instruments 82.10 (Oct. 2011), p. 103501. ISSN: 0034-6748. DOI: 10.1063/1.3643771.
- [61] M. Cavedon, T. Pütterich, E. Viezzer, R. Dux, B. Geiger, R. M. McDermott, H. Meyer, U. Stroth, and ASDEX Upgrade Team. "A fast edge charge exchange recombination spectroscopy system at the ASDEX Upgrade tokamak". In: Review of Scientific Instruments 88.4 (Apr. 2017), p. 043103. ISSN: 0034-6748. DOI: 10.1063/1.4979801.
- [62] D.J. Cruz-Zabala, E. Viezzer, M. Griener, U. Plank, M. Cavedon, P. Cano-Megias, R. Dux, G. Fuchert, J. Garcia-Lopez, M. Garcia-Munoz, A. Jansen van Vuuren, T. Pütterich, and V. Rohde. "Upgrade of the edge Charge Exchange Recombination Spectroscopy system at the High Field Side of ASDEX Upgrade". In: *Journal of Instrumentation* 14.11 (Nov. 2019), p. C11006. DOI: 10.1088/1748-0221/14/11/C11006.
- [63] E. Viezzer, T. Pütterich, G.D. Conway, R. Dux, T. Happel, J.C. Fuchs, R.M. McDermott, F. Ryter, B. Sieglin, W. Suttrop, M. Willensdorfer, E. Wolfrum, and the ASDEX Upgrade Team. "High-accuracy characterization of the edge radial electric field at ASDEX Upgrade". In: Nuclear Fusion 53.5 (Apr. 2013), p. 053005. DOI: 10.1088/0029-5515/53/5/053005.
- [64] K. F. Mast, J. C. Vallet, C. Andelfinger, P. Betzler, H. Kraus, and G. Schramm. "A low noise highly integrated bolometer array for absolute measurement of VUV and soft x radiation". In: Review of Scientific Instruments 62.3 (Mar. 1991), pp. 744–750. ISSN: 0034-6748. DOI: 10.1063/ 1.1142078.
- [65] M. Bernert. "Bolometry with Diodes at the Tokamak ASDEX Upgrade". eng. diploma. München: Technische Universität München, 2010. URL: https://hdl.handle.net/11858/00-001M-0000-0026-F2B0-7.
- [66] M. Bergmann. internal communication. 2025.

- [67] M. Sieben. internal communication. 2025.
- [68] C. Angioni. internal communication. 2025.
- [69] F. L. Hinton and R. D. Hazeltine. "Theory of plasma transport in toroidal confinement systems". In: Rev. Mod. Phys. 48 (2 Apr. 1976), pp. 239–308. DOI: 10.1103/RevModPhys.48.239.
- [70] C. A. Ordonez and M. I. Molina. "Evaluation of the Coulomb logarithm using cutoff and screened Coulomb interaction potentials". In: *Physics of Plasmas* 1.8 (Aug. 1994), pp. 2515–2518. ISSN: 1070-664X. DOI: 10.1063/1.870578.
- [71] N.A. Uckan, Vienna (Austria) International Atomic Energy Agency, and ITER Physics Group. ITER physics design guidelines: 1989. Jan. 2025.
- [72] T. Pütterich, R. Neu, R. Dux, A. D. Whiteford, M. G. O'Mullane, and the ASDEX Upgrade Team. "Modelling of measured tungsten spectra from ASDEXUpgrade and predictions for ITER". In: *Plasma Physics and Controlled Fusion* 50.8 (June 2008), p. 085016. DOI: 10.1088/0741-3335/50/8/085016.
- [73] T. Pütterich, R. Neu, R. Dux, A.D. Whiteford, M.G. O'Mullane, H.P. Summers, and the ASDEX Upgrade Team. "Calculation and experimental test of the cooling factor of tungsten". In: Nuclear Fusion 50.2 (Jan. 2010), p. 025012. DOI: 10.1088/0029-5515/50/2/025012.
- [74] E. Poli, A. Bock, M. Lochbrunner, O. Maj, M. Reich, A. Snicker, A. Stegmeir, F. Volpe, N. Bertelli, R. Bilato, G.D. Conway, D. Farina, F. Felici, L. Figini, R. Fischer, C. Galperti, T. Happel, Y.R. Lin-Liu, N.B. Marushchenko, U. Mszanowski, F.M. Poli, J. Stober, E. Westerhof, R. Zille, A.G. Peeters, and G.V. Pereverzev. "TORBEAM 2.0, a paraxial beam tracing code for electron-cyclotron beams in fusion plasmas for extended physics applications". In: Computer Physics Communications 225 (2018), pp. 36–46. ISSN: 0010-4655. DOI: 10.1016/j.cpc.2017. 12.018.
- [75] AA Ivanov, RR Khayrutdinov, S Yu Medvedev, Yu Yu Poshekhonov, et al. "New adaptive grid plasma evolution code SPIDER". In: Proceedings of 32nd EPS Conference on Plasma Phys., Tarragona, 27 June-1 July 2005 ECA. Vol. 29. 2005, pp. 5-063.
- [76] M. Bergmann, R. Fischer, C. Angioni, K. Höfler, P. Molina Cabrera, T. Görler, T. Luda, R. Bilato, G. Tardini, F. Jenko, and the ASDEX Upgrade team. "Plasma profile reconstruction supported by kinetic modeling". In: *Nuclear Fusion* 64.5 (Apr. 2024), p. 056024. DOI: 10.1088/1741-4326/ad3138.
- [77] D.P. Coster, R. Fischer, O. Hoenen, J. Lakhlili, O.O. Luk, R. Preuss, B.D. Scott, U. von Toussaint, and the ASDEX Upgrade Team. "Building a turbulence-transport workflow incorporating uncertainty quantification for predicting core profiles in a tokamak plasma". In: Nuclear Fusion 61.12 (Nov. 2021), p. 126068. DOI: 10.1088/1741-4326/ac359f.
- [78] Christopher Z Mooney. Monte carlo simulation. 116. Sage, 1997. ISBN: 978-0803959439.
- [79] R. McDermott. internal communication. 2025.

[80] H. Zohm. "Edge localized modes (ELMs)". In: Plasma Physics and Controlled Fusion 38.2 (Feb. 1996), p. 105. DOI: 10.1088/0741-3335/38/2/001.